

COSMOGLOBE I. Improved Wilkinson Microwave Anisotropy Probe frequency maps through Bayesian end-to-end analysis

D. J. Watts^{1*}, A. Basyyrov¹, K. S. F. Fornazier², M. Galloway¹, E. Gjerløw¹, L. T. Hergt³, G. A. Hoerning², H. T. Ihle¹, A. Marins^{2,4}, S. Paradiso⁶, F. Rahman⁷, H. Thommesen¹, M. Bersanelli⁵, L. A. Bianchi⁵, M. Brilenkov¹, L. P. L. Colombo⁵, H. K. Eriksen¹, J. R. Eskilt^{1,8}, U. Fuskeland¹, B. Hensley⁹, D. Herman¹, K. Lee¹, J. G. S. Lunde¹, S. K. Nerval^{10,11}, S. K. Patel¹², M. Regnier¹³, M. San¹, S. Sanyal¹², N.-O. Stutzer¹, A. Verma¹², I. K. Wehus¹, and Y. Zhou¹⁴

¹ Institute of Theoretical Astrophysics, University of Oslo, Blindern, Oslo, Norway

² Instituto de Física, Universidade de São Paulo - C.P. 66318, CEP: 05315-970, São Paulo, Brazil

³ Department of Physics and Astronomy, University of British Columbia, 6224 Agricultural Road, Vancouver BC, V6T1Z1, Canada

⁴ Department of Astronomy, University of Science and Technology of China, Hefei, China

⁵ Dipartimento di Fisica, Università degli Studi di Milano, Via Celoria, 16, Milano, Italy

⁶ Waterloo Centre for Astrophysics, University of Waterloo, Waterloo, ON N2L 3G1, Canada

⁷ Indian Institute of Astrophysics, Koramangala II Block, Bangalore, 560034, India

⁸ Imperial Centre for Inference and Cosmology, Department of Physics, Imperial College London, Blackett Laboratory, Prince Consort Road, London SW7 2AZ, United Kingdom

⁹ Department of Astrophysical Sciences, Princeton University, 4 Ivy Lane, Princeton, NJ 08540

¹⁰ David A. Dunlap Department of Astronomy & Astrophysics, University of Toronto, 50 St. George Street, Toronto, ON M5S 3H4, Canada

¹¹ Dunlap Institute for Astronomy & Astrophysics, University of Toronto, 50 St. George Street, Toronto, ON M5S 3H4, Canada

¹² Department of Physics, Indian Institute of Technology (BHU), Varanasi - 221005, India

¹³ Laboratoire Astroparticule et Cosmologie (APC), Université Paris-Cité, Paris, France

¹⁴ Department of Physics, UC Berkeley

February 28, 2023

ABSTRACT

We present the first joint analysis of *WMAP* and *Planck* LFI time-ordered data, processed within the Bayesian end-to-end COSMOGLOBE framework. This framework builds directly on a similar analysis of the LFI measurements by the BEYONDPLANCK collaboration, and approaches the CMB analysis challenge through Gibbs sampling of a global posterior distribution. The computational cost of producing one complete *WMAP*+LFI Gibbs sample is 581 CPU-hr, including calibration, map-making, and component separation, of which 389 CPU-hr is spent on *WMAP* low-level processing; this demonstrates that end-to-end Bayesian analysis of the *WMAP* We find that our *WMAP* posterior mean temperature sky maps are largely consistent with the official maps. The most notable differences are associated with the gain model; for example, our *K*-band calibration is on average 0.6% lower and it exhibits weaker bi-annual variations. Our polarization maps exhibits significantly weaker transmission imbalance residuals than the official maps, and it is particularly noteworthy that our *W*-band sky maps appear for the first time statistically consistent with the *V*-band maps. At a higher level, *WMAP*-minus-LFI frequency map differences appear for the first time visually consistent with white noise over most of the sky. However, although these new products clearly represent an important step forward in understanding both the *WMAP* and LFI measurements, we do identify three specific issues that require further work, namely 1) noise mismodelling at high temporal frequencies, 2) a quadrupolar *V*-band temperature residual at the 2 μK level; and 3) a strong degeneracy between the absolute *K*-band calibration and the dipole of the anomalous microwave emission component. Nevertheless, the reprocessed *WMAP* maps presented here are significantly cleaner in terms of systematic uncertainties than the official *WMAP* maps, and we believe that they should be preferable for most scientific analyses that require *WMAP* data. Both sky maps and the associated code are made publicly available through the COSMOGLOBE web page.

Key words. ISM: general – Cosmology: observations, polarization, cosmic microwave background, diffuse radiation – Galaxy: general

Contents

1	Introduction	2	2.4 Sky model	4	
2	End-to-end Bayesian CMB analysis	3	2.5 Posterior distribution and Gibbs sampling	5	
2.1	LFI and BEYONDPLANCK	3	2.6 Sampling algorithms	5	
2.2	Official <i>WMAP</i> pipeline	3	2.6.1 Review of sampling algorithms	5	
2.3	Instrument model	4	2.6.2 Differential mapmaking	6	
			2.6.3 Transmission imbalance estimation	7	
			2.6.4 Baseline sampling	7	
			3	Data and data processing	7
			3.1	Publicly available <i>WMAP</i> products	7

* Corresponding author: D. J. Watts; duncanwa@astro.uio.no

3.2	TOD pre-processing and data selection	7
3.3	Computational resources	9
4	Posterior distributions	9
4.1	Gain and baselines	9
4.2	Transmission imbalance	11
4.3	Instrumental noise and goodness-of-fit	11
4.4	Astrophysical sky model	12
5	Markov chains and parameter correlations	12
5.1	Trace plots	12
5.2	Parameter correlations	13
5.2.1	<i>K</i> -band calibration and AME	13
6	Frequency maps and astrophysical components	15
6.1	Map summary statistics	15
6.2	Comparison with 9-year <i>WMAP</i> maps	22
6.3	Consistency within <i>WMAP</i> channels	22
6.4	Consistency between <i>WMAP</i> and LFI	22
6.5	Preliminary CMB results	22
6.5.1	CMB Solar dipole	22
6.5.2	Temperature power spectrum	22
6.5.3	Preliminary large-scale CMB polarization results	22
6.6	Signal-to-noise ratio comparison between <i>WMAP</i> and LFI	22
7	Systematic error corrections and uncertainties	22
7.1	Sky map corrections	22
7.2	Power spectrum residuals	22
8	Outstanding issues	22
8.1	Noise modelling	22
8.2	<i>V</i> -band quadrupole residual	22
8.3	Degeneracy between <i>K</i> -band calibration and AME dipole	22
8.4	Other minor effects	22
8.4.1	Time-variable bandpass modelling	22
8.4.2	Polarized sidelobe modelling	22
9	Conclusions	22
A	Survey of instrumental parameters	36
A.1	Gain, baselines, noise and χ^2	36
A.2	Transmission imbalance	36
B	<i>WMAP</i> frequency map survey	36
C	Comparison with BEYONDPLANCK LFI results	36

1. Introduction

The discovery of the Cosmic Microwave Background (CMB) by Penzias & Wilson (1965) marked a genuine paradigm shift in the field of cosmology, giving direct evidence that the Universe was once much hotter than it is today, effectively ruling out the steady-state theory of the universe (Dicke et al. 1965). Aside from a fundamental shift in the astrophysical history of the universe, this discovery spurred a series of cosmological experiments, which culminated in the Nobel Prize-winning measurements by COBE’s FIRAS and DMR experiments that confirmed the blackbody nature of the CMB and measured temperature variations from the primordial gravitational field (Smoot et al. 1992; Mather et al. 1994).

The *Wilkinson Microwave Anisotropy Probe* (*WMAP*) mission directly superseded the DMR, with the goal of making maps of the CMB that were 45 times more sensitive and 33 times higher angular resolution, all with the goal of measuring the physics of the universe at recombination (Bennett et al. 2003a). It can be argued that *WMAP*’s measurements of the CMB heralded a paradigm shift of similar magnitude to the 1965 discovery of the CMB. As quantified in Bennett et al. (2013), the volume of parameter space in standard Λ CDM allowed before *WMAP* was 68,000 times larger than after, with 99.9985 % of six-parameter Λ CDM ruled out. As a concrete example, the best determination of the age of the CMB before *WMAP* came from Boomerang (Lange et al. 2001) and constrained $t_0 < 14$ Gyr, with peak values of 9–11 Gyr, in contradiction with direct measurements of the oldest globular clusters (Hu et al. 2001).

The *Planck* satellite was developed concurrently with *WMAP*, and their operation lifetimes briefly overlapped, with *Planck* observing from 2009–2013 and *WMAP* from 2001–2011 (cite). *Planck*’s stated goal was to (check overview papers) fully characterize the temperature fluctuations from recombination, as well as to characterize the polarized microwave sky on large angular scales. Overall, the *Planck* experiment’s sensitivity to the CMB was an improvement in white noise sensitivity of a factor x, and a factor of y improvement in angular resolution. Overall, the raw sensitivity of *Planck* was an order of magnitude lower than *WMAP*. As opposed to *WMAP*, which used minimal COBE data in its fiducial analysis, *Planck*’s initial release calibrated off of *WMAP*’s Solar dipole solution, and the Galactic component separation solution found in Planck Collaboration X (2016) by Commander (Jewell et al. 2004; Eriksen et al. 2004, 2006, 2008) made use of *WMAP* frequency maps. Most crucially, the *Planck* and *WMAP* maps are of similar quality that meaningful comparisons can be made between them. This last aspect has been critical, especially for the *Planck* Low Frequency Instrument (LFI), whose channels lie between those of *WMAP*.

As became clear in the LFI analysis (2018 LFI analysis), there was a circular dependency between the instrument calibration and the sky – a robust sky model made from *Planck* LFI maps was required to calibrate the timestreams sufficiently accurately. It was from this need that the BEYONDPLANCK project grew (BeyondPlanck 2022), powered by Commander3 (Galloway et al. 2022), a Gibbs sampling software that performs high-level and low-level parameter estimation in a single integrated framework. This analysis demonstrated the feasibility of a full end-to-end Gibbs sampling analysis in the CMB framework, while providing the highest-quality LFI maps to date.

The success of this paradigm, using properly characterized external datasets to improve TOD processing, led to the COSMOGLOBE initiative. As part of the BEYONDPLANCK suite of papers, Watts et al. (2022) integrated *WMAP* Q-band TODs into the Commander3 framework, calibrated off of the BEYONDPLANCK sky model. Beyond demonstrating that Commander3 can be applied to non-*Planck* data, this analysis uncovered an instrumental effect not previously described in the literature, namely a spurious polarization signal induced by the coupling of the Solar dipole, sidelobes, and horn transmission imbalance.

This paper is the next logical step in the set of previous developments, and presents the first end-to-end TOD analysis of multiple datasets. In this work, we analyze the full *WMAP* dataset at the raw TOD level alongside the *Planck* LFI TODs. As described in Sect. 2, this takes into account the fact that *Planck* and *WMAP* observed the same sky, and hence uses the sky as determined from a component separation using these data as a given in each stage of the Gibbs chain. We describe the underlying data

and computational resources in Sect. 3. We describe the posterior distribution of instrumental parameters in Sect. 4, and describe the properties of the output astrophysical and frequency maps in Sect. 6. Section 7 includes a thorough discussion of systematic error treatment in both frameworks, and Sect. 8 covers the outstanding issues that will be addressed in future analyses. We conclude in Sect. 9, and lay a path forward for the COSMOGLOBE project.

2. End-to-end Bayesian CMB analysis

We begin by discussing the *WMAP* analysis from uncalibrated TOD to maps. Section 2.1 gives an overview of the BEYONDPLANCK project's reanalysis of *Planck* LFI data, Sect. 2.2 provides a brief overview of the official *WMAP* pipeline, and Sect. 2.3 constructs the data model that is used in the end-to-end Gibbs sampling analysis.

2.1. LFI and BEYONDPLANCK

The BEYONDPLANCK project (BeyondPlanck 2022) was the first true application of end-to-end Gibbs sampling in the framework of CMB data analysis. The *Planck* Low Frequency Instrument data had been gradually improved through each *Planck* data release, specifically PR1 (Planck Collaboration II 2016), PR2 (Planck Collaboration II 2016), PR3 (Planck Collaboration II 2020), and PR4 (Planck Collaboration II 2016). Even after PR4, the LFI data still failed polarization null tests and contained visually striking poorly measured modes corresponding to relative gain uncertainty between different detectors. During the PR3 analysis, it became clear that there was a degeneracy between the assumption of the sky's polarization and the gain differences.

The BEYONDPLANCK analysis generated the first clean LFI maps by Gibbs sampling the sky components and underlying instrumental parameters jointly (BeyondPlanck 2022; Galloway et al. 2022; Basyrov et al. 2022). The Commander3 pipeline was used to perform the low-level data analysis conditioned on a sky model that was created through component separation, and the reprocessed maps were used to perform component separation once again. This Gibbs chain not only allowed for the true instrumental properties to be determined thus creating the best LFI maps to date – it fully explored the degeneracies between the low-level instrumental parameters themselves and our knowledge of the sky (Andersen et al. 2022; Svalheim et al. 2022).

2.2. Official WMAP pipeline

The *WMAP* satellite carried forty differential polarization-sensitive radiometers grouped as differencing assemblies (DAs), where one pair was sensitive to the difference in signal at one polarization orientation and the other pair sensitive to the orthogonal polarization. In total, the DAs were allocated as: 1 *K* (23 GHz), 1 *Ka* (30 GHz), 2 *Q* (40 GHz), 2 *V* (60 GHz), and 4 *W* (90 GHz).

The *WMAP* pointing solution was determined using the boresight vectors of individual feedhorns in spacecraft coordinates, in combination with on-board star trackers. Thermal flexure of the tracking structure introduced small pointing errors, as discussed by Jarosik et al. (2007). Using the temperature variation measured by housekeeping data, the quaternion pointing solution was corrected using a linear model that depends on arcsecond per temperature change. The residual pointing errors were computed using observations of Jupiter Saturn, and the reported

upper limit was given by 10" (Bennett et al. 2013; Greason et al. 2012).

The *WMAP* bandpasses were measured directly pre-launch, sweeping a signal source through 201 frequencies and recording the output (Jarosik et al. 2003b). The bandpass responses have not been updated since the initial data release. However, as noted in Bennett et al. (2013), there has been an observed drift in the center frequency of *K*, *Ka*, *Q*, and *V*-band corresponding to a $\sim 0.1\%$ decrease over time. In practice, this did not affect the *WMAP* data processing because each year was mapped separately and co-added afterwards. An effective frequency calculator was delivered in the DR5 release as part of the IDL library to mitigate this effect during astrophysical analyses.¹

The beams were characterized in the form of maps, with separate products for the near-field and far-field. The main beam and near sidelobes were characterized using a combination of physical optics codes and observations of Jupiter for each horn separately. The maps of Jupiter were then combined with the best-fit physical optics codes to create a map of the beam response (Hill et al. 2009; Weiland et al. 2011; Bennett et al. 2013). Far sidelobes were estimated using a combination of laboratory measurements and Moon data taken during the mission (Barnes et al. 2003), as well as a physical optics model describe in Hinshaw et al. (2009). To remove the far sidelobe in the TOD, an estimate was calculated by convolving the intensity map and the orbital dipole signal with the measured sidelobe signal (Jarosik et al. 2007). Although the sidelobe pickup was modeled in Barnes et al. (2003), it was determined that the results were small enough to be neglected, and have not been reported in any of the *WMAP* data releases.

The *WMAP* data were calibrated by jointly estimating the time-dependent gains and baselines, as describe in Hinshaw et al. (2007), Hinshaw et al. (2009), and Jarosik et al. (2011). The TOD are intially modelled as having constant gain and baseline for a 1–24 hour period, and are fit to the orbital dipole assuming T_0 from Mather et al. (1999) and a map made from a previous iteration of the mapmaking procedure. Once the gain and baseline solution has converged, the data are fit to a parametric form of the radiometer performance as a function of housekeeping data, given in Appendix A of Greason et al. (2012).

Transmission imbalance, i.e., the effect of different sky signal transmission from the A-side and B-side optics, is parameterized using x_{im} , which is zero in the case of an ideal differential radiometer. In practice, an unpolarized sky map generates a timestamp

$$d_t^{imbal} \propto (1 + x_{im})T_{p_A} - (1 - x_{im})T_{p_B} \quad (1)$$

$$= (T_{p_A} - T_{p_B}) + x_{im}(T_{p_A} + T_{p_B}). \quad (2)$$

If the x_{im} value is inaccurate, this yields a spurious polarization component, and creates imbalance modes due to coupling with the Solar dipole (Jarosik et al. 2007). The transmission imbalance factors are fit by using the Solar dipole in TOD space and fitting the common-mode and differential signals in TOD space directly (Jarosik et al. 2003a, 2007).

Data are flagged and masked before the final mapmaking step. In particular, station-keeping manuevers, solar flares, and unscheduled events caused certain data to be unusable – the full catalog of these events is listed in Table 1.8 of Greason et al. (2012). In addition, data are masked depending on the channel frequency and the planet itself, with the full list of exclusion radii enumerated in Table 4 of Bennett et al. (2013).

¹ https://lambda.gsfc.nasa.gov/product/wmap/dr5/m_sw.html

To create the sky maps, the calibrated data are put into the asymmetric mapmaking equation,

$$\mathbf{P}_{\text{am}}^T \mathbf{N}^{-1} \mathbf{P} \mathbf{m} = \mathbf{P}_{\text{am}}^T \mathbf{N}^{-1} \mathbf{d}, \quad (3)$$

where \mathbf{P} is implicitly defined for detectors \mathbf{d}_1 and \mathbf{d}_2 sensitive to different polarization orientations,

$$\begin{aligned} \mathbf{d}_1 &= \mathbf{P}_1 \mathbf{m} \\ &= (1 + x_{\text{im}})[T_A + Q_A \cos 2\gamma_A + U_A \sin 2\gamma_A + S_A] \\ &\quad + (1 - x_{\text{im}})[-T_B - Q_B \cos 2\gamma_B - U_B \sin 2\gamma_B - S_B] \end{aligned} \quad (4)$$

$$\begin{aligned} \mathbf{d}_2 &= \mathbf{P}_2 \mathbf{m} \\ &= (1 + x_{\text{im}})[T_A - Q_A \cos 2\gamma_A - U_A \sin 2\gamma_A - S_A] \\ &\quad + (1 - x_{\text{im}})[-T_B + Q_B \cos 2\gamma_B + U_B \sin 2\gamma_B + S_B] \end{aligned} \quad (5)$$

In this formalism, S acts as an extra Stokes parameter that absorbs the effects of different bandpass response between radiometers \mathbf{d}_1 and \mathbf{d}_2 (Jarosik et al. 2007). The asymmetric mapmaking matrix, \mathbf{P}_{am} , is used because, as noted in Jarosik et al. (2011), large signals observed in one beam can leak into the solution for the pixel observed by the other beam, leading to incorrect signals in the final map. The asymmetric mapmaking solution essentially works by only updating the matrix multiplication for beam A when beam A is in a high emission region and beam B is not, and vice versa. Bennett et al. (2013) also identified that these effects are pronounced when there is a steep gradient in the emission across the $N_{\text{side}} = 512$ pixels within an $N_{\text{side}} = 16$ superpixel, leading to excesses 140° away from the Galactic center.

An accurate noise model is necessary to perform the maximum likelihood mapmaking, as it requires the evaluation of \mathbf{N}^{-1} . The time-space autocorrelation function was estimated for each year of data, which is then Fourier transformed, inverted, and Fourier transformed again to create an effective inverse noise operator $\mathbf{N}_{tt'}^{-1}$. Finally, to create the sky maps themselves, the data are treated one year at a time, and the iterative Bi-conjugate Gradient Stabilized Method (BiCG-STAB van der Vorst 1992; Barrett et al. 1994) is applied to the maps.

2.3. Instrument model

As opposed to the *WMAP* pipeline, the COSMOGLOBE model involves creating a generative model for every aspect of the data, including the sky and instrumental effects at once. In the COSMOGLOBE paradigm, it is simplest to characterize the data's goodness-of-fit to a model,

$$\mathbf{d} = \mathbf{GP}[\mathbf{B}^{\text{symm}} \mathbf{Ma} + \mathbf{B}^{4\pi}(\mathbf{s}^{\text{orb}} + \mathbf{s}^{\text{fsl}})] + \mathbf{s}^{\text{inst}} + \mathbf{n}^{\text{corr}} + \mathbf{n}^{\text{w}}, \quad (6)$$

where \mathbf{G} is the time-dependent gain in the form of the matrix $\text{diag}(g_t)$, \mathbf{P} is the $n_p \times n_t$ pointing matrix, \mathbf{B}^{symm} and $\mathbf{B}^{4\pi}$ are the symmetrized and full symmetric beam, respectively, \mathbf{M} is the mixing matrix between a given component c with spectral energy distribution $f_c(\nu/\nu_{0,c})$ and a detector j with bandpass $\tau_j(\nu)$, given by

$$\mathbf{M}_{cj} = \int d\nu \tau_j(\nu) f_c(\nu/\nu_{c,0}). \quad (7)$$

The maps \mathbf{a} are the component amplitudes, \mathbf{s}^{orb} is the orbital dipole induced by the motion of the telescope with respect to the Sun, and \mathbf{s}^{fsl} is the time-dependent far sidelobe signal. In the Commander3 (Galloway et al. 2022) implementation, \mathbf{n}^{corr} is a realization of the correlated noise component whose SED is parametrized by $P(f | \xi_n)$, where ξ_n generally includes f_{knee} ,

a slope α , and whose amplitude is fixed by the white noise σ_0 . Similarly, each experiment has particular signals that are specific to the instrument in question, e.g., the 1 Hz spike in *Planck* LFI or the large baseline in *WMAP*, which can be modeled by \mathbf{s}^{inst} .

The most unique feature of the *WMAP* data is that it includes differential pointing. *WMAP* has two primary mirrors approximately reflected along the vertical satellite axis, and are tilted approximately 19.5° downwards – in total, when horn A is pointed at pixel p_A , horn B is pointed at a pixel p_B that is approximately 141° away (Page et al. 2003). The incoming radiation is differenced in the electronics before being deposited on the detectors, essentially recording radiation proportional to $\mathbf{m}_A - \mathbf{m}_B$ and $\mathbf{m}_B - \mathbf{m}_A$ on the detectors (Jarosik et al. 2003b). Each pair of radiometers has a partner pair of radiometers that observes the same pixels with sensitivity to the orthogonal polarization direction. Taking these effects all into account, the total data model for a single radiometer is given by

$$d_t = g_t \mathbf{P}_{t,p} s_p + s_t^{\text{inst}} + n_t \quad (8)$$

$$\begin{aligned} &= g_t [\alpha_A(T_{p_A(t)} + Q_{p_A(t)} \cos 2\gamma_A(t) + U_{p_A(t)} \sin 2\gamma_A(t)) \\ &\quad - \alpha_B(T_{p_B(t)} + Q_{p_B(t)} \cos 2\gamma_B(t) + U_{p_B(t)} \sin 2\gamma_B(t))] \\ &\quad + s_t^{\text{inst}} + n_t \end{aligned} \quad (9)$$

where s_p is the total sky signal \mathbf{BMa} , $\gamma_{A/B}$ are the time-dependent polarization angles, and $p_{A/B}$ are the A and B pixel locations. In this notation, $\alpha_{A/B}$ is the total optical power transmission for horn A and B. Defining the transmission imbalance for a given radiometer pair $x_{\text{im}} \equiv (\alpha_A - \alpha_B)/(\alpha_A + \alpha_B)$ and absorbing $\alpha_A + \alpha_B$ into the definition of g_t allows the pointing operation to be written in terms of the deviation from ideality,

$$\mathbf{P}_{t,p} s_p = (1 + x_{\text{im}})(T_{p_A} + Q_{p_A} \cos 2\gamma_A + U_{p_A} \sin 2\gamma_A) - (1 - x_{\text{im}})(T_{p_B} + Q_{p_B} \cos 2\gamma_B + U_{p_B} \sin 2\gamma_B). \quad (10)$$

2.4. Sky model

Following BeyondPlanck (2022), we assume that the sky can be modeled as a linear combination of CMB fluctuations, synchrotron, free-free emission, anomalous microwave emission, thermal dust, and radio point sources. The parametric sky model we adopt is given in brightness temperature units as

$$s_{\text{RJ}} = (\mathbf{a}_{\text{CMB}} + \mathbf{a}_{\text{quad}}(\nu)) \frac{x^2 e^x}{(e^x - 1)^2} + \quad (11)$$

$$+ \mathbf{a}_s \left(\frac{\nu}{\nu_{0,s}} \right)^{\beta_s} + \quad (12)$$

$$+ \mathbf{a}_{\text{ff}} \left(\frac{\nu_{0,\text{ff}}}{\nu} \right)^2 \frac{g_{\text{ff}}(\nu; T_e)}{g_{\text{ff}}(\nu_{0,\text{ff}}; T_e)} + \quad (13)$$

$$+ \mathbf{a}_{\text{ame}} e^{\beta(\nu - \nu_{0,\text{ame}})} + \quad (14)$$

$$+ \mathbf{a}_{\text{d}} \left(\frac{\nu}{\nu_{0,\text{d}}} \right)^{\beta_{\text{d}}+1} \frac{e^{h\nu_{0,\text{d}}/k_B T_{\text{d}}} - 1}{e^{h\nu/k_B T_{\text{d}}} - 1} + \quad (15)$$

$$+ U_{\text{mJy}} \sum_{j=1}^{N_{\text{src}}} \mathbf{a}_{j,\text{src}} \left(\frac{\nu}{\nu_{0,\text{src}}} \right)^{\alpha_{j,\text{src}}-2}. \quad (16)$$

Note that the AME model we adopt is a pure exponential, rather than the SED template $s_0^{\text{sd}}(\nu)$ computed using SpDust2 (Ali-Haïmoud et al. 2009; Ali-Haïmoud 2010; Silsbee et al. 2011).

The SpDust2 model was parameterized in [BeyondPlanck \(2022\)](#) by a peak frequency ν_p such that

$$s_{\text{RJ}}^{\text{sd}}(\nu) \propto \nu^{-2} s_0^{\text{sd}} \left(\nu \cdot \frac{30 \text{ GHz}}{\nu_p} \right). \quad (17)$$

In the *WMAP* and LFI frequency range, the exponential model and the SpDust2 are phenomenologically quite similar, despite their very different origins. The exponential model is a simple fit with β drawn from a prior value of -3.57 , and is a clear parametric form that is easy to interpret. An alternative model is the two-parameter log-normal AME SED,

$$s_{\text{RJ}}^{\text{ame,log-N}} = a_{\text{ame}} \left(\frac{\nu}{\nu_{\text{ame}}} \right)^{-2} \exp \left(-\frac{1}{2} \left[\frac{\ln(\nu/\nu_{\text{ame}})}{W_{\text{ame}}} \right]^2 \right), \quad (18)$$

derived by [Stevenson \(2014\)](#) as an analytical approximation to the spinning dust emission. This has also been employed in the latest QUIJOTE analysis, e.g., [Tramonte et al. \(2023\)](#), as it allows for variation of the peak frequency ν_{ame} and width W_{ame} . Although this work is not dependent on the specific parametric form of the AME, we opt for the exponential form described above, as it provides an excellent fit to the diffuse AME with a single parameter.

2.5. Posterior distribution and Gibbs sampling

As shown in [BeyondPlanck \(2022\)](#), this parametric description of the instrumental effects and sky this parametric description of the instrumental effects and sky allows us to write down a total model for the data, $\mathbf{d} = \mathbf{s}^{\text{tot}}(\omega) + \mathbf{n}^{\text{w}}$, where \mathbf{s}^{tot} encompasses all of the terms in Eq. (6) except for the white noise term. Assuming that all instrumental effects have been modelled, the data should be Gaussian distributed with a mean of $\mathbf{s}^{\text{tot}}(\omega)$ and variance σ_0^2 . Given this model, we can evaluate the likelihood for arbitrary chunks of time-ordered data in the context of the entire model, so that individual chunks of data with poor fits can be more easily identified. In general, the likelihood is written

$$P(\mathbf{d} | \omega) \propto \exp \left(-\frac{1}{2} \sum_t \frac{(d_t - s_t^{\text{tot}}(\omega))^2}{\sigma_0^2} \right). \quad (19)$$

If $\mathbf{d} \sim \mathcal{N}(\mathbf{s}^{\text{tot}}, \sigma_0^2)$ is the correct model for the data, the argument of the exponent is proportional to a χ^2 -distribution with n_{TOD} degrees of freedom. In the limit of large n , a χ^2 distribution is well-approximated by a Gaussian with mean n and variance $2n$. Therefore we define and use the reduced- χ^2 statistic,

$$\chi^2 \equiv \frac{\sum_t ((d_t - s_t^{\text{tot}})^2 / \sigma_0^2) - n_{\text{TOD}}}{\sqrt{2n_{\text{TOD}}}}, \quad (20)$$

which is approximately drawn from the standard normal distribution $\mathcal{N}(0, 1)$.

The COSMOGLOBE Gibbs chain is given by

$$\mathbf{g} \leftarrow P(\mathbf{g} | \mathbf{d}, \xi_n, s^{\text{inst}}, \beta, \mathbf{a}, C_\ell, \theta) \quad (21)$$

$$\mathbf{n}_{\text{corr}} \leftarrow P(\mathbf{n}_{\text{corr}} | \mathbf{d}, \mathbf{g}, \xi_n, s^{\text{inst}}, \beta, \mathbf{a}, C_\ell, \theta) \quad (22)$$

$$\xi_n \leftarrow P(\xi_n | \mathbf{d}, \mathbf{g}, \mathbf{n}_{\text{corr}}, s^{\text{inst}}, \beta, \mathbf{a}, C_\ell, \theta) \quad (23)$$

$$s^{\text{inst}} \leftarrow P(s^{\text{inst}} | \mathbf{d}, \mathbf{g}, \mathbf{n}_{\text{corr}}, \xi_n, \beta, \mathbf{a}, C_\ell, \theta) \quad (24)$$

$$\beta \leftarrow P(\beta | \mathbf{d}, \mathbf{g}, \mathbf{n}_{\text{corr}}, \xi_n, s^{\text{inst}}, C_\ell, \theta) \quad (25)$$

$$\mathbf{a} \leftarrow P(\mathbf{a} | \mathbf{d}, \mathbf{g}, \mathbf{n}_{\text{corr}}, \xi_n, s^{\text{inst}}, \beta, C_\ell, \theta) \quad (26)$$

$$C_\ell \leftarrow P(C_\ell | \mathbf{d}, \mathbf{g}, \mathbf{n}_{\text{corr}}, \xi_n, s^{\text{inst}}, \beta, \mathbf{a}, \theta) \quad (27)$$

$$\theta \leftarrow P(\theta | \mathbf{d}, \mathbf{g}, \mathbf{n}_{\text{corr}}, \xi_n, s^{\text{inst}}, \beta, \mathbf{a}, C_\ell), \quad (28)$$

with each step requiring its own dedicated sampling algorithm, and in the case of BEYONDPLANCK, its own publication. The Commander3 pipeline is designed so that results of each Gibbs sample can be easily passed to each other, and that the internal calculations of each step do not directly depend on the inner workings of each other. Therefore, in order to add another data set to the Gibbs chain, one must implement Eqs. (21)–(24) for each instrument, as was done in [BeyondPlanck \(2022\)](#) and [Basyrov et al. \(2022\)](#) for *Planck* LFI and in [Watts et al. \(2022\)](#) for *WMAP*, or simply pass processed maps with beam, mask, and noise information to Eqs. (25)–(28), as was done for the Haslam 408 MHz map ([Haslam et al. 1982](#); [Remazeilles et al. 2015](#)) and the *Planck* 353 and 857 GHz maps.

Before we discuss the results of this Gibbs chain as applied to the *Planck* LFI and *WMAP* data, we summarize the TOD processing steps in Sect. 2.6.

2.6. Sampling algorithms

Each step of the Gibbs chain requires its own distribution to be sampled from. In Sect. 2.6.1 we review the sampling algorithms implemented in the BEYONDPLANCK suite of papers, while Sects. 2.6.2–2.6.4 provide an overview of the *WMAP*-specific processing steps.

2.6.1. Review of sampling algorithms

Several of the techniques required for *WMAP* data analysis have already been implemented and described in the BEYONDPLANCK framework and implemented in Commander3. This section includes a summary of the algorithms that were used described previously for the analysis of LFI data. In each of these cases, every part of the model not explicitly mentioned is held fixed unless specified otherwise.

Noise estimation and calibration, described in [Ihle et al. \(2022\)](#) and [Gjerløw et al. \(2022\)](#) respectively, are highly degenerate, given that the timestream

$$d_{t,i} = g_{q,i} s_{t,i}^{\text{tot}} + n_{t,i}^{\text{corr}} + n_{t,i}^{\text{wn}} \quad (29)$$

is equally well fit by two solutions if $g' = gs^{\text{tot}}/(s^{\text{tot}})$ or $(n^{\text{corr}})' = n^{\text{corr}} + gs^{\text{tot}} + g'(s^{\text{tot}})'$. In practice, this is dealt with by marginalizing over the correlated noise realization \mathbf{n}^{corr} assuming a fixed PSD ξ_n , so that Eqs. (21) and (22) are evaluated as

$$\mathbf{g} \leftarrow P(\mathbf{g} | \mathbf{d}, \xi_n, \dots) \quad (30)$$

$$\mathbf{n}_{\text{corr}} \leftarrow P(\mathbf{n}_{\text{corr}} | \mathbf{d}, \mathbf{g}, \xi_n, \dots). \quad (31)$$

This is allowed by probability theory given that the joint distribution $P(\mathbf{g}, \mathbf{n}_{\text{corr}} | \omega) = P(\mathbf{n}_{\text{corr}} | \mathbf{g}, \omega)P(\mathbf{g} | \omega)$, so that Eqs. (30) and (31) evaluated in sequence is equivalent to drawing a joint sample from $P(\mathbf{g}, \mathbf{n}_{\text{corr}} | \omega)$. In practice, this means that when sampling for \mathbf{g} , the covariance matrix $\mathbf{N} = \mathbf{N}_{\text{wn}} + \mathbf{N}_{\text{corr}}$ must be used, rather than just \mathbf{N}_{wn} .

Commander3 models the gain at each timestream t for a detector i as

$$g_{t,i} = g_0 + \Delta g_i + \delta g_{q,i} \quad (32)$$

where q labels the time interval for which we assume the gain is constant over, e.g., a single scan. In order to sample the gain, we write down a generative model for the TOD,

$$d_i = g_i s_i^{\text{tot}} + n_i^{\text{tot}} \sim \mathcal{N}(g_i s_i^{\text{tot}}, \mathbf{N}_i). \quad (33)$$

Since the \mathbf{d}_i is given as a linear combination of the fixed signal and the gains, a random sample of the gain can be drawn by solving²

$$[(\mathbf{s}_i^{\text{tot}})^T \mathbf{N}_i^{-1} \mathbf{s}_i^{\text{tot}}] \mathbf{g}_i = (\mathbf{s}_i^{\text{tot}})^T \mathbf{N}_i^{-1} \mathbf{d}_i + (\mathbf{s}_i^{\text{tot}})^T \mathbf{N}_i^{-1/2} \boldsymbol{\eta}. \quad (34)$$

Note that the \mathbf{N}_i depends implicitly on the noise PSD ξ_n , while the specific realization of \mathbf{n}_{corr} is accounted for in the covariance matrix. In practice, as shown in Gjerløw et al. (2022), Commander3 samples g_0 , Δg_i , and $\delta g_{q,i}$ in separate sampling steps. Formally, the Gibbs chain is broken by fitting the absolute gain g_0 to the orbital dipole rather than the full sky signal. However, this makes the sampling much more robust to unmodelled systematic effects, so the trade-off in rigor is justified.

The correlated noise sampling, described in Ihle et al. (2022), follows a similar procedure to gain sampling, except now conditioned upon the gain estimate, sampled just before correlated noise in the code. Similar to the gain case, we can write a generative model for the data

$$\mathbf{d}_i = \mathbf{g}_i \mathbf{s}_i^{\text{tot}} + \mathbf{n}_i^{\text{corr}} + \mathbf{n}_i^{\text{wn}} \sim \mathcal{N}(\mathbf{g}_i \mathbf{s}_i^{\text{tot}}, \mathbf{N}_{\text{corr},i} + \mathbf{N}_{\text{wn},i}). \quad (35)$$

Given fixed $\mathbf{r}_i = \mathbf{d}_i - \mathbf{g}_i \mathbf{s}_i^{\text{tot}}$, we can again write a sampling equation,

$$(\mathbf{N}_{\text{corr},i}^{-1} + \mathbf{N}_{\text{wn},i}^{-1}) \mathbf{n}_i^{\text{corr}} = \mathbf{N}_{\text{wn},i}^{-1} \mathbf{r}_i + \mathbf{N}_{\text{wn},i}^{-1/2} \boldsymbol{\eta}_1 + \mathbf{N}_{\text{corr},i}^{-1/2} \boldsymbol{\eta}_2. \quad (36)$$

This gives a sample of the true underlying correlated noise that occurred when the instrument was taking data. In practice, this is equivalent to the destriping mapmaking algorithm Madam, and returns equivalent results to the classical method (Keihänen et al. 2022).

To solve for the correlated noise parameters, we assume that the correlated noise is drawn from a correlated Gaussian and form the posterior distribution

$$P(\xi_n | \mathbf{n}^{\text{corr}}) \propto \frac{\exp[-\frac{1}{2}(\mathbf{n}^{\text{corr}})^T \mathbf{N}_{\text{corr}}^{-1} \mathbf{n}^{\text{corr}}]}{\sqrt{|\mathbf{N}_{\text{corr}}|}} P(\xi_n). \quad (37)$$

The simplest parameterization for correlated noise is given by

$$\mathbf{N}_{\text{corr}}(f) = \sigma_0^2 \left(\frac{f}{f_{\text{knee}}} \right)^\alpha. \quad (38)$$

This can in principle be modified, and for *Planck* LFI a Gaussian log-normal bump was added at a late stage in the BEYOND-PLANCK analysis. Rather than sampling for σ_0 , we effectively fix the white noise level to the noise level at the highest frequency, e.g.,

$$\sigma_0^2 \equiv \frac{\text{Var}(r_{t+1} - r_t)}{2}, \quad (39)$$

where t and $t + 1$ are consecutive time samples, and $\mathbf{r} \equiv \mathbf{d} - \mathbf{g} \mathbf{s}^{\text{tot}} - \mathbf{n}^{\text{corr}}$. In practice, this makes σ_0 a deterministic function of the sampled sky and gain parameters. The parameters α and f_{knee} are not linear in the data, so must be sampled using the general inversion sampler.³ In practice, this requires gridding out the posterior one parameter at a time.

The bandpass mismatch is explicitly modeled in Commander3. Using the calibrated sky model, the expected calibrated sky signal is given by

$$m_{p,j} = \mathbf{B}_{p,p'} \sum_c \mathbf{M}_{c,j} a_p^c + n_{j,p}^w. \quad (40)$$

² See, e.g., Appendix A.2 of BeyondPlanck (2022) for a derivation of this result.

³ See, e.g., Appendix A.3 of BeyondPlanck (2022) and Chapter 7.3.2 of Press et al. (2007) for further details.

Since $\mathbf{M}_{c,j}$ encodes the bandpass response of every detector j to every component c , the maps \mathbf{m}_j will each be slightly different depending on their bandpass τ_j . More importantly, differences in signal between different detectors can be attributed to a spurious polarization signal, giving spurious polarized maps. Therefore, before averaging different detectors together, Commander3 estimates the average over all detectors in a given frequency channel $\mathbf{m} \equiv \langle \mathbf{m}_j \rangle$, and subtracts it directly in the timestream;

$$\delta s_{t,j}^{\text{leak}} = \mathbf{P}_{t,p}^j \mathbf{B}_{p,p'}^j (\mathbf{m}_{j,p'} - \mathbf{m}_{p'}). \quad (41)$$

This leakage term uses the expected bandpass

Once the instrumental parameters have been sampled, Commander3 computes the calibrated TOD for each band,

$$r_{t,j} = \frac{d_{t,j} - n_{t,j}^{\text{corr}}}{g_{t,j}} - (s_{t,j}^{\text{orb}} + s_{t,j}^{\text{fsl}} + \delta s_{t,j}^{\text{leak}} + s_{t,j}^{\text{inst}}) \quad (42)$$

where s^{orb} is the orbital dipole, s^{fsl} is the far sidelobe timestream, δs^{leak} is the bandpass leakage, and s^{inst} is the set of instrumental parameters, e.g., the 1 Hz spike in LFI. With the a correlated noise realization removed, one can perform simple binned mapmaking, weighting each pixel by the white noise amplitude.

2.6.2. Differential mapmaking

The first additional algorithm that needed to be added to Commander3 was differential mapmaking, since the *Planck* LFI data came from a standard single-horn instrument.

After calibration and correction for instrumental effects, the TOD can be modeled as

$$\mathbf{d} = \mathbf{P}\mathbf{m} + \mathbf{n}^w, \quad (43)$$

where

$$\mathbf{m} = \mathbf{B}^{\text{symm}} \mathbf{M} \mathbf{a} \quad (44)$$

is the expected map for each detector after removing the orbital dipole, far sidelobe, baseline, and a realization of correlated noise. The differential pointing strategy can be represented in matrix form as

$$\mathbf{P}_{tp} = (1 + x_{\text{im}})(\delta p'_A p'_A + \delta p'^{\text{o}} p'^{\text{o}} \cos 2\psi_A + \delta p'^{\text{u}} p'^{\text{u}} \sin 2\psi_A) \quad (45)$$

$$- (1 - x_{\text{im}})(\delta p'_B p'_B - \delta p'^{\text{o}} p'^{\text{o}} \cos 2\psi_B - \delta p'^{\text{u}} p'^{\text{u}} \sin 2\psi_B) \quad (46)$$

where p_A and p_B are the time-dependent pointings for each DA. The maximum likelihood map can in principle be solved using the usual mapmaking equation,

$$\mathbf{P}^T \mathbf{N}^{-1} \mathbf{P} \mathbf{m} = \mathbf{P}^T \mathbf{N}^{-1} \mathbf{d}. \quad (47)$$

For a single-horn experiment, i.e., *Planck* LFI, this reduces to a 3×3 matrix that can be inverted for each pixel independently. For the pointing matrix in Eq. (45), this is no longer possible, as there is inherently coupling between horns A and B in the timestreams. The $3N_{\text{pix}} \times 3N_{\text{pix}}$ matrix can be solved using an iterative algorithm, e.g., preconditioned conjugate gradients.

Jarosik et al. (2011) identified an issue where a large difference in the sky temperature at pixel value at pixel A versus pixel B induced artifacts in the mapmaking procedure. We adopt the procedure first described in Hinshaw et al. (2003) where only the pixel in a bright region, defined by a small processing mask (Bennett et al. 2013) is accumulated, thus modifying the mapmaking equation to

$$\mathbf{P}_{\text{am}}^T \mathbf{N}^{-1} \mathbf{P} \mathbf{m} = \mathbf{P}_{\text{am}}^T \mathbf{N}^{-1} \mathbf{d}. \quad (48)$$

This equation can be solved using the BiCG-STAB algorithm for a non-symmetric matrix \mathbf{A} where $\mathbf{Ax} = \mathbf{b}$. We apply a preconditioner \mathbf{M} by numerically inverting the same problem with $N_{\text{side}} = 16$ maps and applying a diagonal noise matrix. Numerically, we define convergence as when the residual $\mathbf{r} \equiv \mathbf{b} - \mathbf{Ax}$ satisfies $\mathbf{r}^T \mathbf{M}^{-1} \mathbf{r} / \mathbf{b}^T \mathbf{M}^{-1} \mathbf{b} < 10^{-10}$, which typically takes about 20 iterations for producing frequency maps.

2.6.3. Transmission imbalance estimation

Transmission imbalance, i.e., the differential power transmission of the optics and waveguide components, can be parameterized as

$$d_{t,j} = g_{t,j}[(1 + x_{\text{im},j})s_{t,j}^{\text{tot,A}} - (1 - x_{\text{im},j})s_{t,j}^{\text{tot,B}}] + n_t. \quad (49)$$

This can be decomposed into a differential (d) and common-mode (c) signal such that

$$d_{t,j} = g_{t,j}[s_{t,j}^{\text{d}} + x_{\text{im},j}s_{t,j}^{\text{c}}] + n_t. \quad (50)$$

In this form, the imbalance parameters can be estimated by drawing Gaussian samples from the standard mean and standard deviation over the entire mission. To draw samples for $x_{\text{im},j}$, we construct the sampling routine analogous to Eqs. (34) and (36) with $\mathbf{r} = \mathbf{d} - \mathbf{gs}^{\text{d}}$,

$$[(\mathbf{gs}^{\text{c}})^T \mathbf{N}^{-1} \mathbf{gs}^{\text{c}}]x_{\text{im}} = (\mathbf{gs}^{\text{c}})^T \mathbf{N}^{-1} \mathbf{r} + (\mathbf{gs}^{\text{c}})^T \mathbf{N}^{-1/2} \boldsymbol{\eta}, \quad (51)$$

essentially cross-correlating the common-mode signal with \mathbf{r} with appropriate weights and adding a Gaussian random variable with the correct weighting. Note that we are marginalizing over the correlated noise here by using $\mathbf{N} = \mathbf{N}_{\text{wn}} + \mathbf{N}_{\text{corr}}$. This mitigates any baseline drifts being erroneously attributed to the common-mode signal and biasing the estimate of x_{im} .

The *WMAP* procedure, described in Jarosik et al. (2003a), fit for common-mode and differential coefficients along with a cubic baseline over 10 precession periods at a time, corresponding to 10 hours of observation. The mean and uncertainty were then calculated by averaging and taking the standard deviation of these values. This approach has the benefit of allowing for the tracking of possible transmission imbalance variation throughout the mission. However, none of the *WMAP* suite of papers have indicated this, and it has not arisen in our analysis, so we model this as an effect whose value is constant throughout the mission.

2.6.4. Baseline sampling

The data model adopted in Hinshaw et al. (2003) can be written in raw digital units (du) as

$$\mathbf{d} = \mathbf{GPBM}\mathbf{a} + \mathbf{n} + \mathbf{b}, \quad (52)$$

where \mathbf{b} is the instrumental baseline and \mathbf{n} is the total instrumental noise. As detailed in Ihle et al. (2022), Commander3 divides the noise into $\mathbf{n} = \mathbf{n}^{\text{w}} + \mathbf{n}^{\text{corr}}$, a white noise term and a correlated noise term. By definition, the white noise does not have any correlations between adjacent pixels, so that any pixel-pixel covariance should be fully described by realizations of the \mathbf{n}^{corr} timestream.

Commander estimates the baseline using the full estimate of the current sky model, $\mathbf{r} = \mathbf{d} - \mathbf{gs}^{\text{tot}} = \mathbf{b} + \mathbf{n}$. Modeling $\mathbf{b} = b_0 + b_1 \Delta t$, we solve for b_0 and b_1 using linear regression in each timestream while masking out samples that lie within the processing mask. Strictly speaking, this is breaking the Gibbs

chain, as we are not formally sampling b_0 and b_1 for each TOD chunk. In practice, baseline estimation uncertainty propagates to correlated noise realizations and PSD parameters, as discussed below.

The approach detailed in Hinshaw et al. (2003) and the Commander implementation differ mainly in the assumed stable timescale – the initial *WMAP* baseline is estimated over one hour timescales, whereas Commander assumes constant values throughout the entire timestream, 3–7 days depending on the band in question. As noted in Hinshaw et al. (2003), residual baseline variations manifest as correlated noise stripes in the final maps. *WMAP9* solves this using a time-domain filter, downweighting the data based off of the noise characterization. This approach is equivalent to the Commander3 procedure of removing a constrained realization of correlated noise from the timestream directly, based on the best-fit to the noise PSD.

3. Data and data processing

We describe the delivered *WMAP* data in Sect. 3.1, then describe the treatment we apply it to make them compatible with Commander3 in Sect. 3.2, then describe the computational requirements in Sect. 3.3.

3.1. Publicly available WMAP products

The full *WMAP* dataset is hosted at the Legacy Archive for Microwave Background Data Analysis (LAMBDA).⁴ In addition to the primary scientific products, e.g., cosmological parameters, CMB power spectra and anisotropy maps, and frequency maps, the time-ordered data (TOD) can be downloaded, both in uncalibrated and calibrated form.⁵ In principle, thanks to these data and the explanatory supplements (Greason et al. 2012), the entire data analysis pipeline can be reproduced from TOD in digital units (du) to frequency maps.

For this analysis, we keep certain instrumental parameters fixed to the reported values. For example, we have made no attempts to rederive the pointing solutions, re-estimate the main beam response and far sidelobe pickup, or recover data that was flagged in the *WMAP* event log. These and other analyses, such as estimating the bandpass shift over the course of the mission, are certainly possible within the larger Gibbs sampling framework. However, in this work we limit ourselves to recalibrating the TOD, estimating the noise properties, and applying bandpass corrections to the data before mapmaking.

3.2. TOD pre-processing and data selection

The full nine-year *WMAP* archive spans from August 10, 2001 to August 10, 2010, with the raw uncalibrated data spanning 626 GB. A little over 1 % of the data were lost or rejected due to incomplete satellite telemetry, thermal disturbances, spacecraft anomalies, and station-keeping maneuvers, with an extra 0.1 % rejected due to planet flagging (Bennett et al. 2003b; Hinshaw et al. 2007, 2009; Bennett et al. 2013). The final results reported in Bennett et al. (2013) included roughly 98.4 % of the total data volume. A full accounting of all data cuts can be found in Table 1.8 of Greason et al. (2012). In total, we flag the same data

⁴ https://lambda.gsfc.nasa.gov/product/wmap/dr5/m_products.html

⁵ https://lambda.gsfc.nasa.gov/product/wmap/dr5/tod_info.html

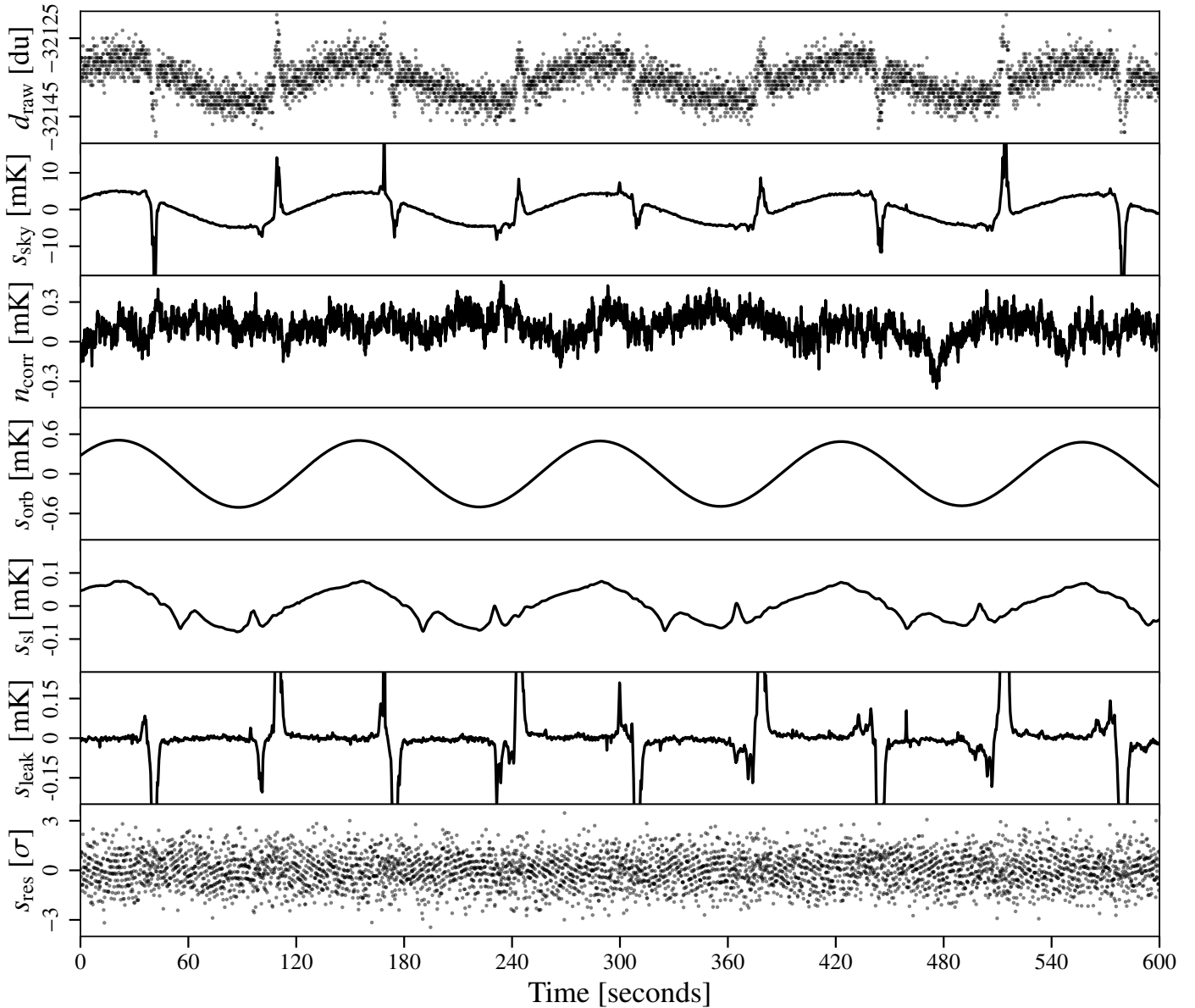


Fig. 1. Each of the timestreams that go into the model. Note the varying dynamic ranges of each plot.

Table 1. Flagging statistics

Band	Flagged (%)	Discarded (%)	Used (%)
<i>K</i>	1.72	0.87	97.4
<i>Ka</i>	1.64	0.88	97.5
<i>Q1</i>	1.84	0.84	96.5
<i>Q2</i>	1.62	0.81	97.6
<i>V1</i>	1.62	1.10	97.3
<i>V2</i>	1.61	1.01	97.4
<i>W1</i>	1.76	1.03	97.2
<i>W2</i>	1.60	0.81	97.6
<i>W3</i>	1.61	0.87	97.5
<i>W4</i>	1.60	0.81	97.6

indicated in the fiducial *WMAP* analysis, and use the same planet flags.

As shown in Galloway et al. (2022), a large fraction of Commander3’s computational time is spent performing FFTs on individual scans. Rather than truncating datastreams to have

lengths equal to “magic numbers” for which FFTW (Frigo & Johnson 2005) is fastest, as in Galloway et al. (2022), we split the data into scans of length 2^N , where $N = 22$ for *K*–*Q*, $N = 23$ for *V*–*W*. This yields scans with lengths of 6.21 days for *K*- and *Ka*-band, 4.97 days for *Q*-band, 7.46 days for *V*-band, and 4.97 days for *W*-band. These datastream lengths are short enough to be processed quickly and distributed efficiently across multiple processors, while being long enough to properly characterize the noise properties of the timestreams, whose f_{knee} ’s are on the order 1 mHz. Most importantly, FFTW performs fastest when the datastream is of length 2^N .

When rechunking the data, timestreams of length 2^N were interrupted by events logged in Table 1.8 of Greason et al. (2012). When we encountered these events, TOD segments that were interrupted by the event were appended to the previous TOD, in most cases creating TODs with lengths $> 2^N$. We found that events of length $< 2^N$ were too short to accurately estimate the noise PSD parameters. This criterion led us to discard these otherwise useful data. In addition, when $> 10\%$ of the TOD was flagged, the large number of gaps in the data made the con-

strained realizations unreliable, as well as biasing the noise PSD parameters. Together, these two effects led to $\simeq 1\%$ of the data to be discarded despite being of acceptable quality. We present the full flagging statistics for our maps in Table 1. In total, the COSMOGLOBE maps use slightly less data than the *WMAP9* official products, which had a total efficiency of $\simeq 98.4\%$ (Bennett et al. 2013). The total difference in data volume can be entirely accounted for by the cuts described in this paragraph.

3.3. Computational resources

A key motivation of the COSMOGLOBE project is to evaluate whether it is feasible to perform a joint analysis of two datasets simultaneously, each with its own particular processing requirements and algorithmic treatment. One of the results from Watts et al. (2022) was that most of the data processing procedures for *WMAP* and *Planck* LFI overlapped, with the notable exception of mapmaking. While the algorithmic requirements have been discussed in Sect. 2, we have not yet quantified the requirements in terms of RAM and CPU hours. In Table 2, we enumerate the RAM requirements and CPU time for each sampling step using the local cluster at the Institute of Theoretical Astrophysics at the University of Oslo. The node that these numbers come from used 128 cores of an AMD EPYC 7H12, 2.6 GHz machine with 2 TB of memory. As Commander3 is parallelized and used 128 cores, wall hours in Table 2 can be obtained by dividing by 128.

Despite the relatively small data volume spanned by *WMAP*, the CPU time is comparable to each of the LFI channels. By far the largest reason for this is the mapmaking step, which requires looping over the entire dataset for each matrix multiplication, a process which must be repeated ~ 20 times. This is vastly sped up by the use of a low resolution preconditioner, reducing the number of iterations by an order of magnitude.

Additionally, operations that require creating timestreams for each detector, i.e., TOD projection, sidelobe evaluation, and orbital dipole projection, take much longer than expected from a pure data volume scaling. Part of this is due to each *WMAP* radiometer needing to evaluate the sky in two pixels simultaneously, doubling the expected workload. The operations of gain sampling and correlated noise sampling include multiple FFTs. Typical LFI TODs are of length $\sim 200\,000$, an order of magnitude smaller than the *WMAP* TODs of length 2^{22-23} .

4. Posterior distributions

4.1. Gain and baselines

To compare the calibrated TODs from *WMAP* versus COSMOGLOBE, it is important to look at the *WMAP* gain model,

$$g = \alpha \frac{\bar{V} - V_\circ - \beta(T_{\text{RXB}} - 290\text{ K})}{T_{\text{FPA}} - T_\circ} + (m\Delta t + c), \quad (53)$$

where α , V_\circ , β , T_\circ , m , and c are fit to a constant value across the mission for each radiometer. \bar{V} are radio frequency bias powers per detector, and T_{RXB} and T_{FPA} are the receiver box and focal plane assembly temperatures, which are recorded every 23.04 s. Evaluating the model as a function of T_{RXB} and T_{FPA} requires finding the housekeeping data for the thermistor that was physically closest to the relevant radiometer's focal plane on the satellite. As this requires detailed technical information about the specifications of the satellite's schematics layout that can easily be misunderstood, we do not attempt to reproduce the gain model given in Eq. (53) in this work. Although we are unable to

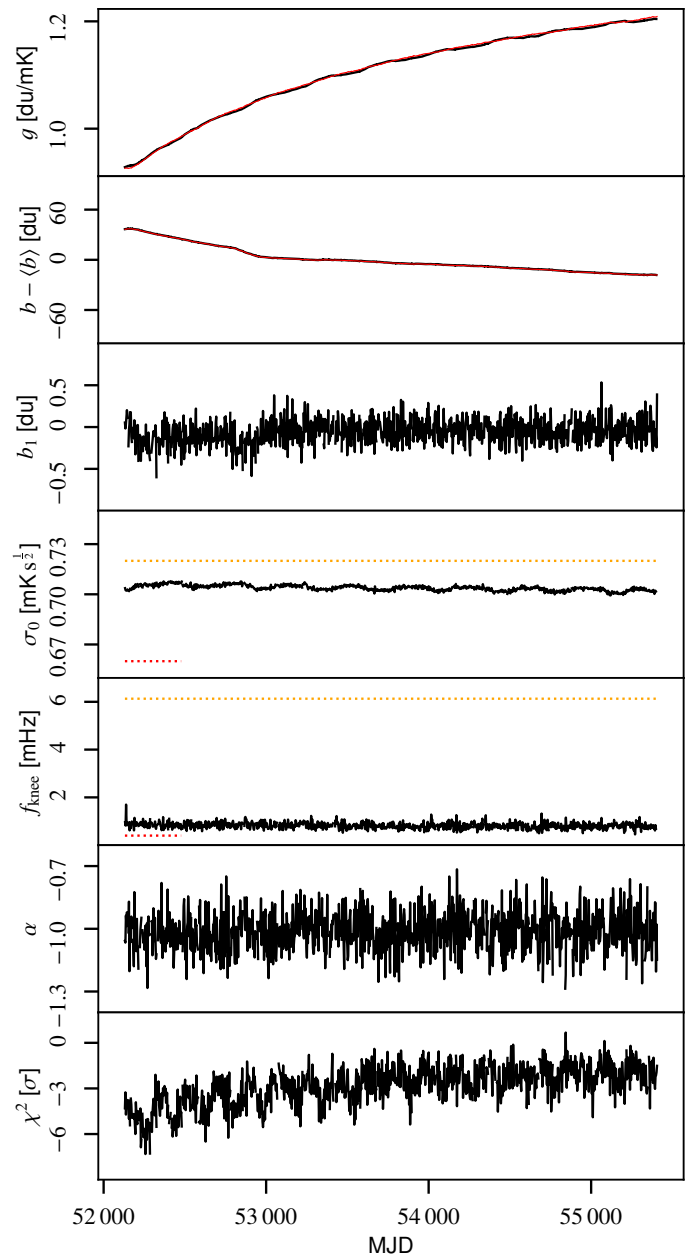


Fig. 2. Overview of K113. The red solid lines in first and second panel are the delivered gain and baselines from *WMAP9*, while the black lines in all panels are samples from the COSMOGLOBE Gibbs chain. The red dashed and yellow dashed lines are reported σ_0 and f_{knee} values from the first-year *WMAP* data analysis and GSFC measurements, respectively.

reproduce the exact gain model parametrized in Greason et al. (2012), the 23.4 s time dependence of the gain model on housekeeping data is a plausible explanation for the time-dependent noise variation in the different calibrated data solutions.

As reported in Hinshaw et al. (2007), the calibrated data archive has been calibrated using the procedure listed above, with a baseline subtracted each hour and the sidelobe subtracted. Figure 3 shows the COSMOGLOBE timestream $d/g - s_{\text{sl}} - b$ with the *WMAP* delivered calibrated signal subtracted. The most prominent feature is a $\sim 25\,\mu\text{K}$ offset, which is unsurprising, given the different treatment of baselines in our two pipelines. The second obvious difference is a series of spikes associated with Galactic plane crossings. The differences of order $50\,\mu\text{K}$ correspond to sky brightness of order 10 mK, equivalent to $\sim 0.5\%$ devi-

Table 2. Computational resources required for end-to-end COSMOGLOBE processing. All times correspond to CPU hours, and all data volumes are reported in GB. Reported times are averaged over more than 100 samples, and vary by $\lesssim 5\%$ from sample to sample.

ITEM	30	44	70	K	Ka	Q1	Q2	V1	V2	W1	W2	W3	W4	SUM
<i>Data volume</i>														
Compressed TOD volume	86	178	597	13	12	15	15	19	18	26	26	26	26	1 053
<i>Processing time (cost per run)</i>														
TOD initialization/IO time	1.8	2.5	9.3	0.3	0.3	0.4	0.4	0.4	0.4	0.5	0.5	0.5	0.5	17.8
Other initialization														13.4
Total initialization														31.2
<i>Gibbs sampling steps (cost per sample)</i>														
Huffman decompression	1.1	2.1	10.5	0.9	0.8	1.0	1.0	1.3	1.3	1.8	1.8	1.8	1.8	27.2
TOD projection (P operation)	0.4	0.9	4.2	2.6	2.6	3.3	3.4	4.3	4.3	6.4	6.3	6.3	6.4	54.0
Sidelobe evaluation	1.0	2.1	7.6	2.9	2.9	3.5	3.5	4.7	4.8	7.0	6.9	6.9	6.9	60.7
Orbital dipole	0.9	1.9	7.1	1.3	1.3	1.7	1.7	2.2	2.3	3.4	3.3	3.3	3.3	33.7
Gain sampling	0.5	0.8	1.9	0.8	0.8	0.5	0.5	0.9	0.9	0.7	0.7	0.7	0.7	10.4
1 Hz spike sampling	0.3	0.4	1.6											2.4
Correlated noise sampling	2.0	4.0	21.7	2.8	2.9	3.3	3.6	5.1	5.4	8.0	7.7	7.2	8.5	81.3
Correlated noise PSD sampling	4.8	5.9	1.5	0.2	0.2	0.3	0.3	0.5	0.4	0.7	0.6	0.6	0.7	16.7
TOD binning (P' operation)	0.1	0.1	4.0	0.5	0.5	0.7	0.8	0.8	0.8	1.2	1.2	1.2	1.2	13.1
Mapmaking						6.4	7.0	8.9	8.1	11.1	9.5	14.4	14.3	119.5
Sum of other TOD processing	4.4	8.6	44.4	14.7	4.6	5.1	5.0	9.4	7.7	8.1	6.8	8.6	8.7	136.1
TOD processing cost per sample	15.5	26.8	104.5	23.0	24.1	27.6	27.9	40.3	37.4	51.7	50.6	51.9	54.6	535.9
Amplitude sampling														14.0
Spectral index sampling														25.5
Total cost per sample														581.2

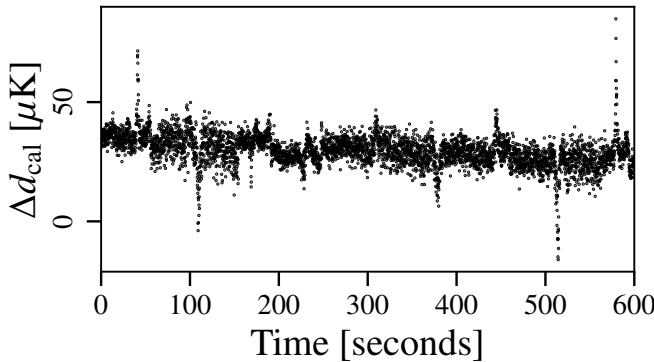


Fig. 3. Difference between the COSMOGLOBE $d_{\text{cal}} = \mathbf{d}/g - \mathbf{b} - s_{\text{sl}}$ and the delivered calibrated TOD from WMAP.

ations in the gain solution. This is twice as large as the 0.2 % uncertainty estimated in [Bennett et al. \(2013\)](#) based on end-to-end simulations.

On longer timescales, as displayed in Figure 4, the most prominent feature is a varying signal of amplitude 0.2 mK. This likely due to the hourly baseline subtraction mentioned above, which contrasts with the COSMOGLOBE approach of assigning a linear baseline solution for the entire scan. The variations are commensurate with correlated noise, which for K113 has $f_{\text{knee}} \sim 0.5$ mHz, corresponding to a little over half an hour. Therefore, the hourlong baseline subtraction essentially acts as a destriper, removing an estimate of the correlated noise. To test this hypothesis, we plot a realization of correlated noise generated by Commander, and find that the signals are very similar, both in amplitude and morphology.

We also compare the gain and baseline solutions throughout the course of the mission in Fig. 2. To recover the WMAP9 gain

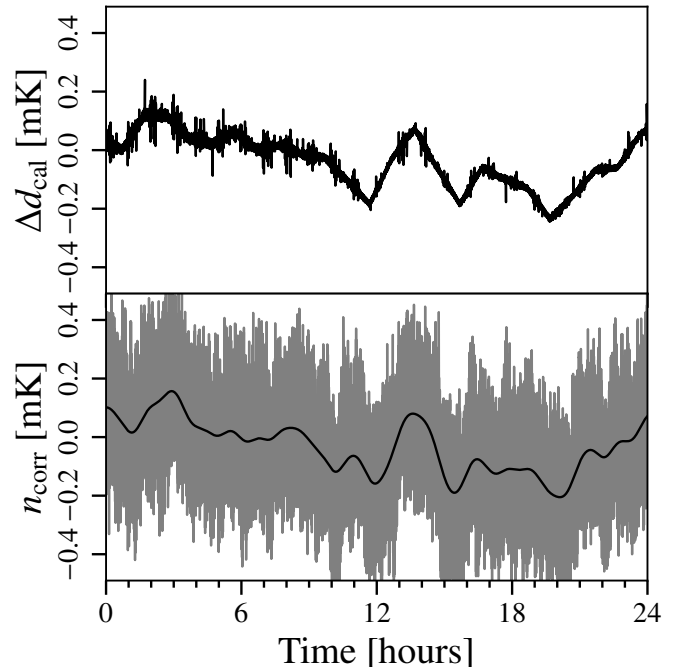


Fig. 4. (top) Difference between the COSMOGLOBE $d_{\text{cal}} = \mathbf{d}/g - \mathbf{b} - s_{\text{sl}}$ and the delivered calibrated TOD from WMAP. (bottom) Raw correlated noise (gray) and smoothed data with Gaussian kernel (black). This shows more clearly the hourly baseline subtraction from the WMAP treatment.

solution, we directly compare the uncalibrated WMAP data with the calibrated WMAP data with a far sidelobe contribution convolved with the delivered WMAP9 DA maps. We find that the

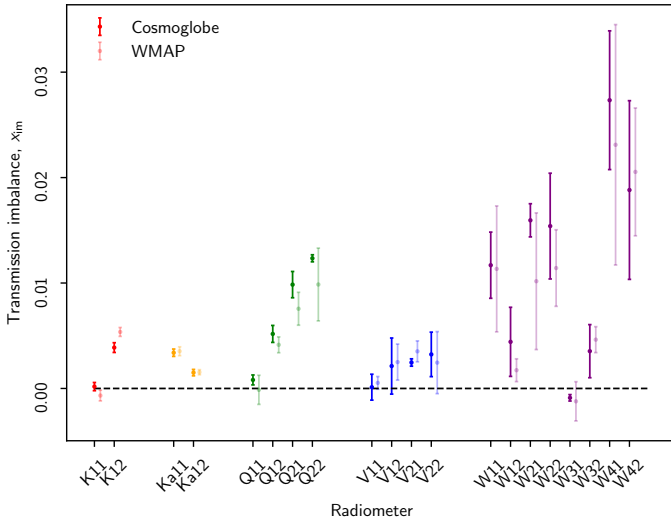


Fig. 5. Transmission imbalance

calibrated and uncalibrated data can be related by

$$d_t^{\text{raw}} = g(d_t^{\text{cal}} + s_t^{\text{sl}}) + \sum_{i=0}^3 c_i(t - t_0)^i. \quad (54)$$

We find that d_t^{raw} is consistent with the expression on the right at the level of < 0.1 du for all radiometers, suggesting that this estimate of g and the baseline c_0 is a good approximation of the *WMAP9* calibration solution. An initial estimate using a linear baseline gave an unacceptably poor fit. Given that Eqn. (2) of [Jarosik et al. \(2003a\)](#) employed a cubic baseline fit while fitting for transmission imbalance parameters, it is reasonable to assume that the official calibrated archive was created using a similar procedure.

The morphological characteristics of the *WMAP9* and COSMOGLOBE gain solutions are similar, with a general trend to increase with time. Both solutions also follow a sinusoidal pattern, corresponding to temperature change due to L2's motion around the Sun ([Greason et al. 2012](#)). However, we do find the amplitude of the COSMOGLOBE K -band gain is slightly lower than the *WMAP9* solution, and with fewer oscillatory features. Other than the absolute calibration shift in K -band, the gains are consistent between COSMOGLOBE and *WMAP9* within 1 %. For completeness, the full gain comparisons can be found in Fig. A.3.

4.2. Transmission imbalance

The transmission imbalance parameters x_{im} are crucial to measure correctly because their mis-estimation can induce a large polarized signal that is coupled to the Solar dipole ([Jarosik et al. 2007; Watts et al. 2022](#)). The uncertainty in x_{im} was quoted as the source of large-scale polarized features in the *WMAP9* maps, and a template of this effect was explicitly projected out in the pixel-space polarized covariance matrix.

We find x_{im} values that are largely consistent with the values reported in [Bennett et al. \(2013\)](#), albeit with some outliers. We find in general that the 68 % confidence intervals from COSMOGLOBE are smaller than the fiducial values, although we caution against a direct comparison of these values since such different procedures were used for estimating the uncertainties.

4.3. Instrumental noise and goodness-of-fit

The noise fitting, as outlined in Sect. 2.6, inherently depends the data being fit well by both the sky model and the instrument model. In practice, correlated noise fitting can model any unmodelled signals, so the power spectrum and TODs must be carefully scrutinized before any conclusions can be made about the corresponding maps.

The white noise level in raw du is not strictly sampled, but is estimated conditioned on the instrumental parameters and the sky parameters. However, the calibrated white noise level $\sigma_0[\text{K}] = \sigma_0[\text{du}]/g$ does depend on the gain quite directly, which allows us to test the effects of the calibration on the instrument sensitivity itself. The calibrated white noise level follows a biaannual trend indicative of a system temperature variation, which is to be expected given the radiometer equation

$$\sigma_0[\text{V}] \propto gT_{\text{sys}}. \quad (55)$$

Aside from an overall amplitude shift due to the absolute calibration variation, the shape of the white noise level is stable throughout the Gibbs chain.

The knee frequencies for each channel lie between the reported values in [Jarosik et al. \(2003a\)](#) for both the Goddard Space Flight Center (GSFC) laboratory measurements and those from the first year of data collection. Nearly all radiometers have constant f_{knee} throughout the mission, with a few notable exceptions. First, all W -band channels display some amount of temporal variation that does not seem to be associated with any sinusoidal features. Second, all $Q2$ channels, V223, and V224 all display a similar asymptotic drift in time. We have not found any instrumental effects that share this feature. The PSD slope α is around -1 for each radiometer, albeit with high scatter for the lower frequencies. As expected, the uncertainty in α decreases as f_{knee} increases, since there are more datapoints to fit below f_{knee} where the constraining power on α is the strongest.

The most striking feature of the reduced normalized χ^2 is its amplitude and its semiannual periodicity. Given the noise model and data residual, we can evaluate the goodness-of-fit in the form of the relative χ^2 . Here, we find that approximately half of the radiometers have a χ^2 value at least 6σ above or below the expected value. Given perfect Gaussian residuals, we would expect the reduced sum of squares to be $n_{\text{TOD}} = 2^N$ and be within $\sqrt{2n_{\text{TOD}}} = 2^{(N+1)/2}$ 68 % of the time. For a typical W -band scan of length $n_{\text{TOD}} = 2^{22}$, a 10σ model failure corresponds to $\chi^2/n_{\text{TOD}} = 1.003$. Therefore, it is exceedingly difficult to look at any given *WMAP* scan in the time domain and identify a model failure. In power spectrum space, i.e., in Fig. 6, the data are still characterized well at all scales, despite this scan having a $\chi^2/7\sigma$ above the expectation value.

Only with aggressive smoothing, as in Fig. 7, does the model failure become apparent at frequencies 1–10 Hz. Here, it is clear that despite fitting the data well at the highest and lowest frequencies, it is in the intermediate range of 1–5 Hz where the power spectrum is a less accurate fit to the power spectrum. Part of the cause of this failure is that the white noise level is essentially fixed by the value of the power spectrum at the Nyquist frequency, as it was computed by differencing adjacent samples. The power spectrum has a downward trend beyond above 1 Hz, indicating that the data would be better fit by one or more terms proportional to f^α . This is phenomenologically similar to the *WMAP* collaboration's approach of describing the time-space autocorrelation as a cubic polynomial in $\log \Delta t$ ([Jarosik et al. 2007](#)).

Table 3. Summary of noise properties.

Radiometer ..	Diode	Sensitivity, σ_0 (mK \sqrt{s})			Knee frequency, f_{knee} (mHz)			Slope, α
		GSFC	WMAP	CG/ $\sqrt{2}$	GSFC	WMAP	CG/ $\sqrt{2}$	
K11	1	0.72	0.66	0.704 ± 0.002	6.13	0.4	0.82 ± 0.20	-1.01 ± 0.10
	2			0.708 ± 0.003			0.63 ± 0.14	-0.95 ± 0.10
K12	1	0.87	0.75	0.796 ± 0.004	5.37	0.51	0.42 ± 0.19	-0.93 ± 0.12
	2			0.780 ± 0.005			0.71 ± 0.15	-1.02 ± 0.10
Ka11	1	0.75	0.71	0.788 ± 0.001	1.66	0.71	1.20 ± 0.22	-1.02 ± 0.09
	2			0.777 ± 0.001			1.19 ± 0.22	-1.02 ± 0.09
Ka12	1	0.77	0.72	0.788 ± 0.003	1.29	0.32	0.62 ± 0.16	-0.99 ± 0.11
	2			0.784 ± 0.001			0.63 ± 0.13	-1.01 ± 0.11
Q11	1	0.99	0.92	0.998 ± 0.002	3.21	1.09	1.06 ± 0.16	-1.09 ± 0.09
	2			0.992 ± 0.002			1.06 ± 0.16	-1.10 ± 0.09
Q12	1	0.95	1.02	1.159 ± 0.007	3.13	0.35	0.45 ± 0.47	-0.98 ± 0.11
	2			1.146 ± 0.007			0.83 ± 0.14	-1.00 ± 0.09
Q21	1	0.89	0.85	0.908 ± 0.002	1.92	5.76	2.88 ± 0.37	-1.10 ± 0.07
	2			0.906 ± 0.002			3.22 ± 0.56	-1.10 ± 0.06
Q22	1	1.04	0.99	1.074 ± 0.004	4.61	8.62	3.95 ± 0.54	-1.11 ± 0.06
	2			1.064 ± 0.003			4.05 ± 0.64	-1.11 ± 0.06
V11	1	1.25	1.22	1.551 ± 0.003	2.56	0.09	1.27 ± 0.15	-0.90 ± 0.06
	2			1.539 ± 0.003			1.19 ± 0.14	-0.89 ± 0.06
V12	1	1.07	1.11	1.398 ± 0.002	4.49	1.41	2.11 ± 0.20	-0.97 ± 0.05
	2			1.432 ± 0.002			1.88 ± 0.17	-0.96 ± 0.05
V21	1	1.01	0.97	1.241 ± 0.298	2.43	0.88	1.50 ± 0.24	-0.95 ± 0.07
	2			1.217 ± 0.294			1.60 ± 0.26	-0.97 ± 0.06
V22	1	1.13	1.1	1.443 ± 0.300	3.06	8.35	4.01 ± 0.85	-1.00 ± 0.08
	2			1.415 ± 0.316			3.08 ± 0.65	-1.01 ± 0.08
W11	1	1.18	1.35	1.938 ± 0.005	16.2	7.88	5.59 ± 0.53	-0.94 ± 0.05
	2			1.895 ± 0.005			8.99 ± 0.85	-0.95 ± 0.04
W12	1	1.41	1.61	2.301 ± 0.005	15.1	0.66	3.91 ± 0.42	-0.89 ± 0.05
	2			2.345 ± 0.006			4.81 ± 0.53	-0.89 ± 0.05
W21	1	1.38	1.61	2.225 ± 0.007	1.76	9.02	13.57 ± 1.47	-0.89 ± 0.03
	2			2.292 ± 0.006			5.06 ± 0.95	-0.93 ± 0.05
W22	1	1.44	1.72	2.291 ± 0.006	0.77	7.47	3.02 ± 0.53	-0.98 ± 0.05
	2			2.232 ± 0.007			7.26 ± 1.05	-0.95 ± 0.04
W31	1	1.47	1.65	2.328 ± 0.005	1.84	0.93	1.30 ± 0.46	-0.99 ± 0.07
	2			2.322 ± 0.006			1.97 ± 0.28	-0.98 ± 0.06
W32	1	1.69	1.86	2.707 ± 0.015	2.39	0.28	1.59 ± 0.29	-0.98 ± 0.07
	2			2.579 ± 0.015			1.40 ± 0.39	-1.00 ± 0.07
W41	1	1.6	1.71	2.519 ± 0.010	8.46	46.5	26.81 ± 1.83	-0.92 ± 0.04
	2			2.479 ± 0.009			24.75 ± 1.63	-0.92 ± 0.04
W42	1	1.43	1.65	2.221 ± 0.017	5.31	26.0	16.10 ± 1.09	-0.94 ± 0.04
	2			2.202 ± 0.015			17.11 ± 1.19	-0.94 ± 0.04

In practice, the $1/f$ model has a small effect on the final data products, and was not visible in noise models when we modeled the data in one day scans rather than the longer 3–7 day scans due to the lower n_{TOD} giving a higher uncertainty on the relative χ^2 . Therefore, although this strictly constitutes a deficiency in the model, it is in practice too small to affect the results of the rest of the chain. The downturn of the noise PSD at high frequencies is also present in, e.g., the *Planck* HFI data ([Planck Collaboration Int. XLVI 2016](#), Fig. 1), so improved modelling of this form will be a necessity in future COSMOGLOBE endeavors, and will be used to improve the *WMAP* data processing.

4.4. Astrophysical sky model

Given the frequency maps,⁶ we can determine the component's amplitude maps as part of the Gibbs chain. Due to the high signal-to-noise of the K -band map, which was not used in the

[BeyondPlanck \(2022\)](#) for this reason, the spectral indices were not fit in this chain but rather drawn from prior distributions.

5. Markov chains and parameter correlations

5.1. Trace plots

To illustrate the dependence of the goodness-of-fit on the noise model, we inspect the 50th TOD segment, corresponding to MJDs 52285.2–52290.6, as a function of Gibbs iteration, in Fig. 9. This is one of the worst-fitting TOD segments of the entire mission, with a reduced relative χ^2 of -7.5 , equivalent to $\chi^2/n = 0.993$. The line plots demonstrate a strong correlation between the noise parameters and the χ^2 , while the gain itself is almost completely uncorrelated with the variations in the χ^2 . As σ_0 is not formally sampled in the Gibbs chain, it is weakly dependent on f_{knee} and α , making it more likely that it is the driver of the correlations in this figure.

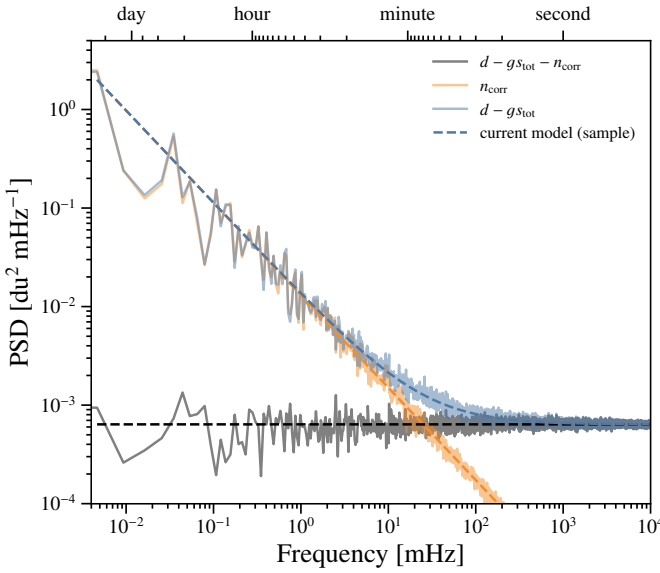


Fig. 6. PSD for radiometer W413 that spans MJDs 52252.3–52254.8. The power spectrum of the blue line corresponds to the residual, while the gray line is the residual with a correlated noise realization removed.

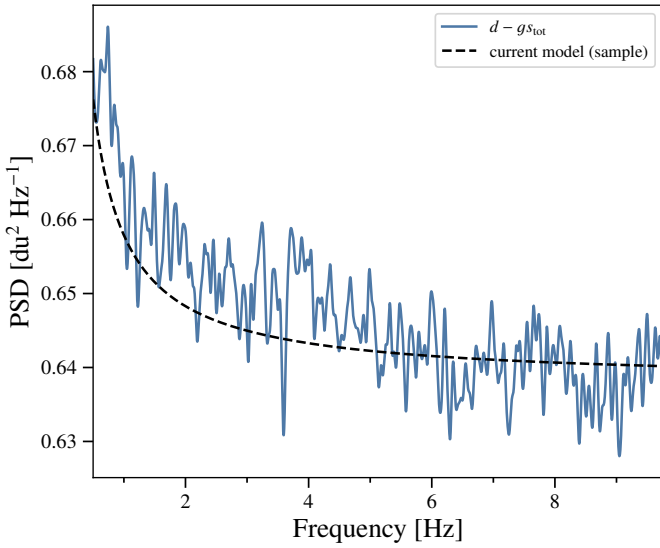


Fig. 7. PSD for radiometer W413 that spans MJDs 52252.3–52254.8. The black dashed line is a sample of the theoretical PSD, while the blue line is the smoothed residual power spectrum.

5.2. Parameter correlations

Fusce mauris. Vestibulum luctus nibh at lectus. Sed bibendum, nulla a faucibus semper, leo velit ultricies tellus, ac venenatis arcu wisi vel nisl. Vestibulum diam. Aliquam pellentesque, augue quis sagittis posuere, turpis lacus congue quam, in hendrerit risus eros eget felis. Maecenas eget erat in sapien mattis porttitor. Vestibulum porttitor. Nulla facilisi. Sed a turpis eu lacus commodo facilisis. Morbi fringilla, wisi in dignissim interdum, justo lectus sagittis dui, et vehicula libero dui cursus dui. Mauris tempor ligula sed lacus. Duis cursus enim ut augue. Cras ac magna. Cras nulla. Nulla egestas. Curabitur a leo. Quisque egestas wisi eget nunc. Nam feugiat lacus vel est. Curabitur consectetur.

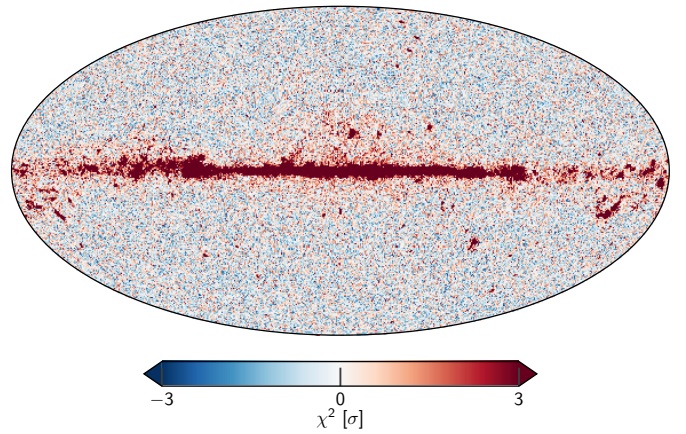


Fig. 8. Reduced- χ^2 , using $n_{\text{dof}} = 300$, which comes from fitting to the regions outside of the K -band processing mask.

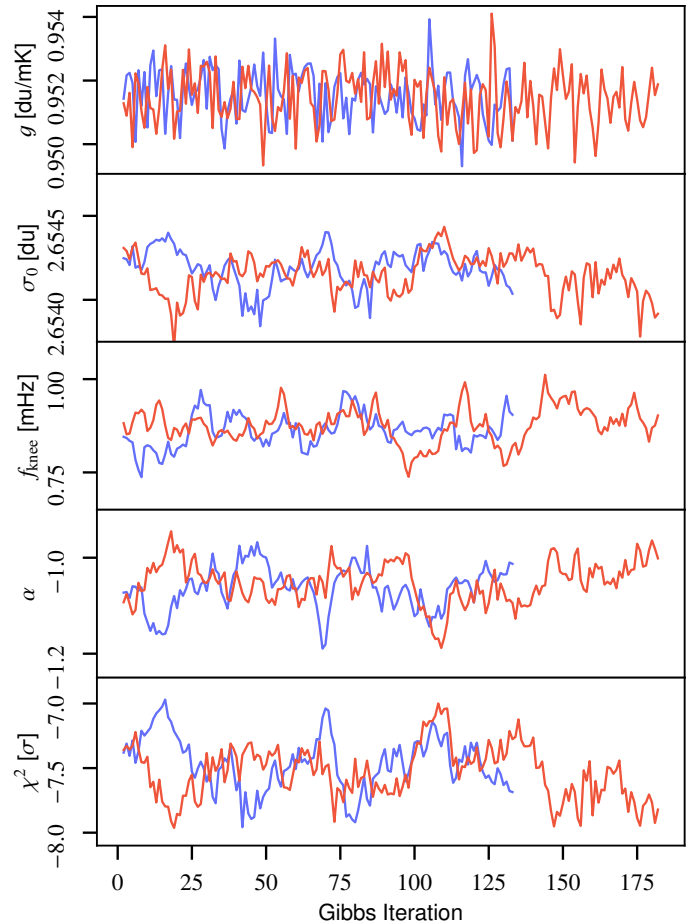


Fig. 9. Subset of K113 Gibbs samples for both chains, arbitrarily coloured red and blue. The gain, noise PSD parameters, and χ^2 correspond to MJDs 52285.2–52290.6.

5.2.1. K-band calibration and AME

In a preliminary Commander3 run, we discovered an unbounded rise in the K -band absolute calibration, g_0 , and the dipole in the AME component of the sky. Because the AME is strongest among all bands at K -band, any increase in the K -band absolute calibration can easily be accounted for by changing the amplitude of the AME, while leaving goodness-of-fit tests such as relative- χ^2 and residual maps unaffected.

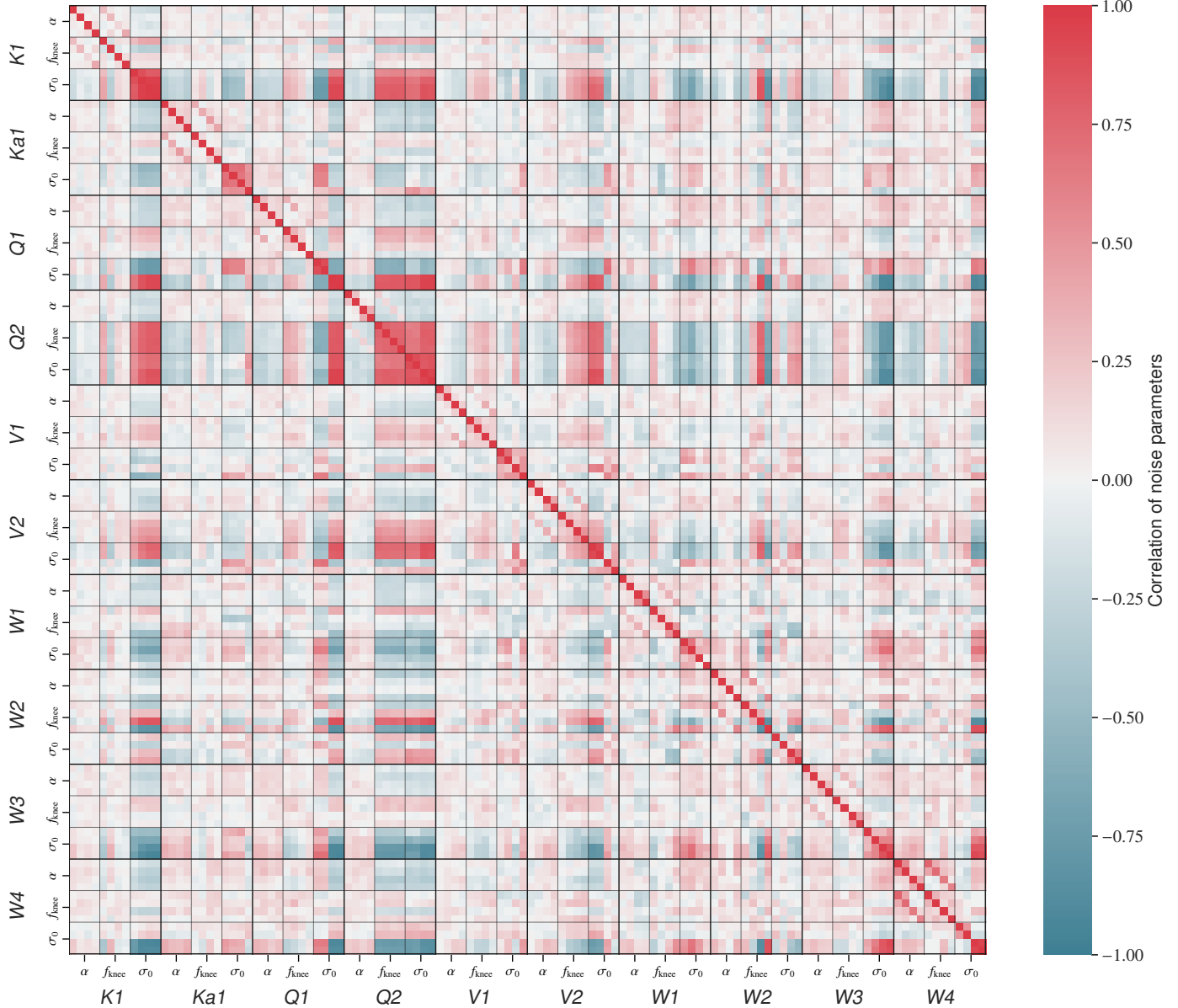


Fig. 10. Noise parameter correlation matrix. We average over all Gibbs samples of the noise parameters $\xi^n = \{\alpha, f_{\text{knee}}, \sigma_0\}$ for each PID. We then find the correlation in time between these averages for the different bands and detector. The results here are for the calibrated white noise level, σ_0 [mK]. The values for each detector are ordered 13, 14, 23, and 24

In order to break this degeneracy, it was necessary to impose a prior either on the AME itself or on the absolute calibration. The AME prior we explored followed the approach of [Andersen et al. \(2022\)](#), in which the prior mean was the *Planck* DR4 857 GHz map scaled by $3 \cdot 10^{-5}$, and the variance is given in angular scales by a parameter q . We found that a prior of $q = 10^{-2} \mu\text{K}^2$ was necessary to stabilize the gain, resulting in an AME map that was nearly identical to the *Planck* 857 GHz band. As this gave a result that was inconsistent with many previous results, we opted instead to sample the absolute calibration instead.

Any error in g_0 leads to a residual due to the large Solar dipole. In practice, we found that the typical variation of g_0 was 0.002, giving a relative error of $\sim 0.1\%$. This variation induces a $\sim 6 \mu\text{K}$ Solar dipole uncertainty, which is easily attributed to AME during component separation. In Figure 36, we demonstrate this effect on recovered AME maps using extreme g_0 values of 1.175 and 1.9. We find that AME maps consistent with

those presented in [Bennett et al. \(2013\)](#) and [Planck Collaboration X \(2016\)](#) are recovered when g_0 is between 1.180 and 1.182. Based on this analysis, we sample g_0 from a Gaussian with mean 1.1815 and standard deviation 0.001.

[Bennett et al. \(2013\)](#) and [Planck Collaboration X \(2016\)](#) find AME peak frequencies 12.0–17.5 GHz and 17–23 GHz, respectively, both with low signal-to-noise at high Galactic latitude and with structure along the plane. The Q-U-I JOint Tenerife Experiment (QUIJOTE) has recently released maps of the sky with approximately 70 % sky coverage at frequencies 11, 13, 17, and 19 GHz ([Rubiño-Martín et al. 2023](#)). QUIJOTE is optimized for characterizing the polarized sky, and constraints from, e.g., [de la Hoz et al. \(2023\)](#), will be critical for future polarized synchrotron SED characterization and polarized AME limits. While in principle the AME SED can be constrained by a joint *WMAP/LFI/QUIJOTE* analysis, we consider this outside of the scope of the paper, which aims to evaluate the effect of jointly

analyzing *WMAP* and *Planck* LFI at the TOD level. Future analysis will include the QUIJOTE data, and hopefully break the g_{0-a} degeneracy.

Lorem ipsum dolor sit amet, consectetur adipiscing elit. Ut purus elit, vestibulum ut, placerat ac, adipiscing vitae, felis. Curabitur dictum gravida mauris. Nam arcu libero, nonummy eget, consectetur id, vulputate a, magna. Donec vehicula augue eu neque. Pellentesque habitant morbi tristique senectus et netus et malesuada fames ac turpis egestas. Mauris ut leo. Cras viverra metus rhoncus sem. Nulla et lectus vestibulum urna fringilla ultrices. Phasellus eu tellus sit amet tortor gravida placerat. Integer sapien est, iaculis in, pretium quis, viverra ac, nunc. Praesent eget sem vel leo ultrices bibendum. Aenean faucibus. Morbi dolor nulla, malesuada eu, pulvinar at, mollis ac, nulla. Curabitur auctor semper nulla. Donec varius orci eget risus. Duis nibh mi, congue eu, accumsan eleifend, sagittis quis, diam. Duis eget orci sit amet orci dignissim rutrum.

The second main deviation... is in the treatment the noise power spectra. As shown in Sect 2.5 of Jarosik et al. (2007), the noise autocorrelation spectrum is fit on a year-by-year basis to a polynomial in $\log(\Delta t)$, where Δt is the time lag between data points. This method is very similar to the Commander3 approach, which fits for the power spectrum in Fourier space using a correlated noise model of the form $\sigma_0^2(f/f_{\text{knee}})^\alpha$. Properly parameterized, these two approaches should yield similar results, albeit with different levels of uncertainty and time resolution. However, we have confirmed that in many cases the simple $1/f$ noise model does not fit the signal-subtracted TOD, yielding χ^2 values that are up to 10σ discrepant from their expected values. [Show, discuss figure with the PSDs, residual spectrum, and Bessel filter.]

Deviations from the $1/f$ model consist either of a linear increase or downturn above 10 Hz. This can be partially explained by the use of a two pole Bessel low-pass filter just prior to signal quantization, which introduces a 2.62% correlation between 25.6 ms sample integrations (Jarosik et al. 2003b, Sect. 5.3). The exact form of the Bessel filter was not used on flight data, but rather the parametric fit as discussed above. However, the filter is designed to reduce the signal by half at 100 Hz, and as such has a negligible effect.

Lorem ipsum dolor sit amet, consectetur adipiscing elit. Ut purus elit, vestibulum ut, placerat ac, adipiscing vitae, felis. Curabitur dictum gravida mauris. Nam arcu libero, nonummy eget, consectetur id, vulputate a, magna. Donec vehicula augue eu neque. Pellentesque habitant morbi tristique senectus et netus et malesuada fames ac turpis egestas. Mauris ut leo. Cras viverra metus rhoncus sem. Nulla et lectus vestibulum urna fringilla ultrices. Phasellus eu tellus sit amet tortor gravida placerat. Integer sapien est, iaculis in, pretium quis, viverra ac, nunc. Praesent eget sem vel leo ultrices bibendum. Aenean faucibus. Morbi dolor nulla, malesuada eu, pulvinar at, mollis ac, nulla. Curabitur auctor semper nulla. Donec varius orci eget risus. Duis nibh mi, congue eu, accumsan eleifend, sagittis quis, diam. Duis eget orci sit amet orci dignissim rutrum.

Nam dui ligula, fringilla a, euismod sodales, sollicitudin vel, wisi. Morbi auctor lorem non justo. Nam lacus libero, pretium at, lobortis vitae, ultricies et, tellus. Donec aliquet, tortor sed accumsan bibendum, erat ligula aliquet magna, vitae ornare odio metus a mi. Morbi ac orci et nisl hendrerit mollis. Suspendisse ut massa. Cras nec ante. Pellentesque a nulla. Cum sociis natoque penatibus et magnis dis parturient montes, nascetur ridiculus mus. Aliquam tincidunt urna. Nulla ullamcorper vestibulum turpis. Pellentesque cursus luctus mauris.

Nulla malesuada porttitor diam. Donec felis erat, congue non, volutpat at, tincidunt tristique, libero. Vivamus viverra fermentum felis. Donec nonummy pellentesque ante. Phasellus adipiscing semper elit. Proin fermentum massa ac quam. Sed diam turpis, molestie vitae, placerat a, molestie nec, leo. Maecenas lacinia. Nam ipsum ligula, eleifend at, accumsan nec, suscipit a, ipsum. Morbi blandit ligula feugiat magna. Nunc eleifend consequat lorem. Sed lacinia nulla vitae enim. Pellentesque tincidunt purus vel magna. Integer non enim. Praesent euismod nunc eu purus. Donec bibendum quam in tellus. Nullam cursus pulvinar lectus. Donec et mi. Nam vulputate metus eu enim. Vestibulum pellentesque felis eu massa.

Quisque ullamcorper placerat ipsum. Cras nibh. Morbi vel justo vitae lacus tincidunt ultrices. Lorem ipsum dolor sit amet, consectetur adipiscing elit. In hac habitasse platea dictumst. Integer tempus convallis augue. Etiam facilisis. Nunc elementum fermentum wisi. Aenean placerat. Ut imperdiet, enim sed gravida sollicitudin, felis odio placerat quam, ac pulvinar elit purus eget enim. Nunc vitae tortor. Proin tempus nibh sit amet nisl. Vivamus quis tortor vitae risus porta vehicula.

6. Frequency maps and astrophysical components

6.1. Map summary statistics

Will combine these spectra shortly

Want to compare the *QU* correlation in *WMAP* and *Planck* LFI, get a quantitative number. Point out that the polarization solution itself is much better, but the covariance between pixels themselves is much higher. This wasn't an issue for LFI, so we had to take that into account here.

I also want to put a bit here on why the low- ℓ approach needed to be done separately, how correlated noise sampling addresses it, to what extent it's mitigated, etc.

Note that LFI's 30 and 70 GHz *QU* correlation is ~ 0.1 , whereas 44 GHz is much larger, ~ 0.5 . This discrepancy is due to the number of horns with differing polarization orientation. Both 30 and 70 GHz have an even number of horns, allowing for pairs of datastreams to be combined to give independent polarization measurements. Conversely, 44 GHz has one horn pair and an unpaired horn, the latter of which induces more correlation in the *QU* observation matrix. An example for *Ka* and 30 GHz is shown in Fig. ???. Aside from the obvious morphological changes due to the two experiments' different observing strategies, the magnitude of *WMAP*'s correlation is much larger than *Planck*'s.

The BEYONDPLANCK project took this covariance structure into account using the dense $N_{\text{side}} = 16$ noise covariance matrix provided by the *WMAP* team.⁷ Properly sampled correlated noise only leaves white noise in the maps, so the noise properties of each map's sample do not require a dense pixel-pixel covariance, even at low resolution (BeyondPlanck 2022; Basyrov et al. 2022). The *WMAP9* inverse noise covariance matrices were computed using the full time-space noise matrix $\mathbf{N} = \mathbf{N}^{\text{w}} + \mathbf{N}^{\text{corr}}$, so the full pixel-pixel covariance matrix $\Sigma^{-1} = \mathbf{P}^T \mathbf{N}^{-1} \mathbf{P}$ took into account the correlation between neighboring samples. The COSMOGLOBE maps, by subtracting a realization of correlated noise before mapmaking, estimates an inverse noise covariance matrix

$$\Sigma_{pp'}^{-1} = \sum_{t_1, t_2} \mathbf{P}_{t_1, p_1}^T \mathbf{N}_{t_1, t_2}^{-1} \mathbf{P}_{t_2, p_2} = \sum_t \mathbf{P}_{t, p_1}^T \mathbf{N}_{t, t}^{-1} \mathbf{P}_{t, p_2} \quad (56)$$

⁷ https://lambda.gsfc.nasa.gov/product/wmap/dr5/ninv_info.html

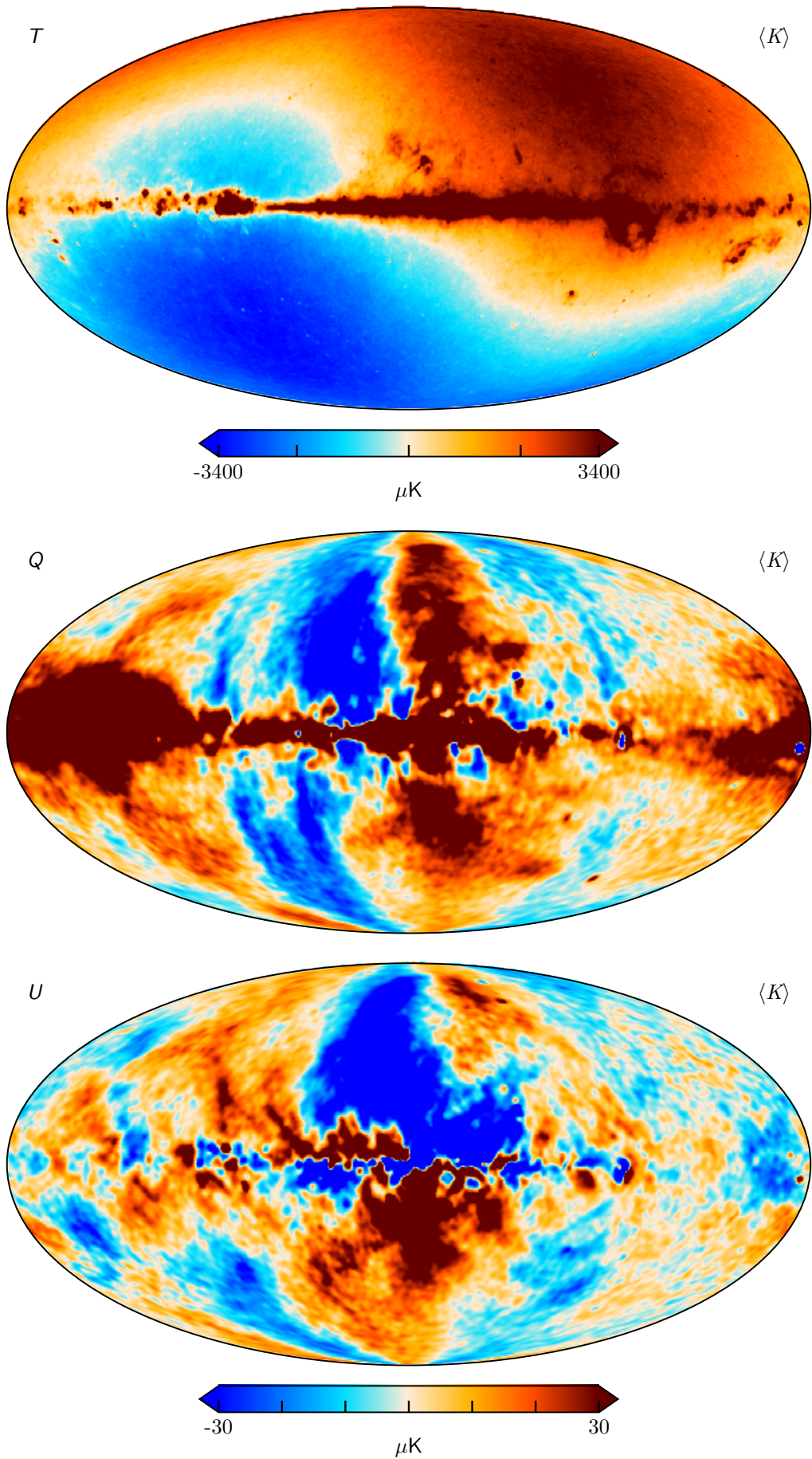
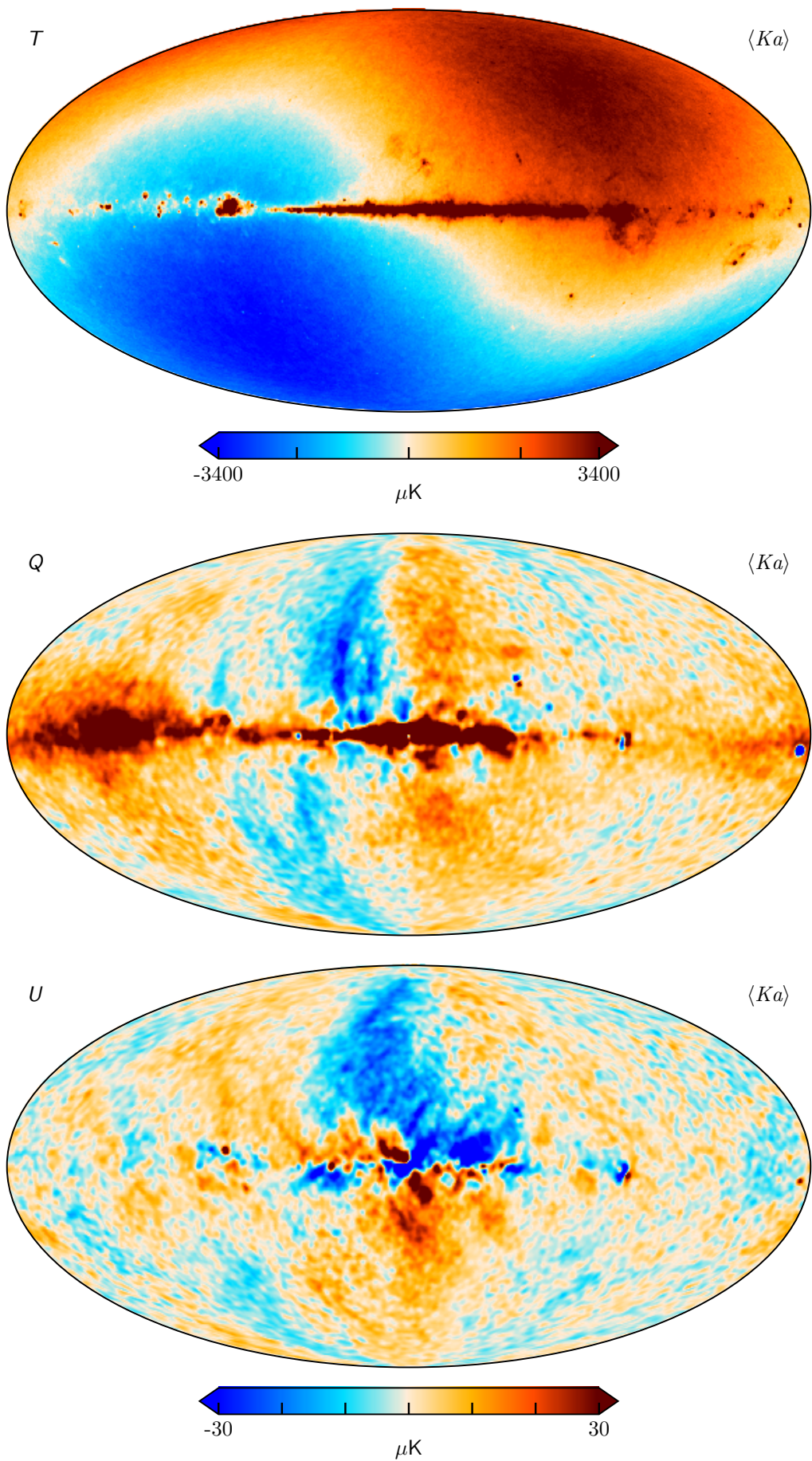


Fig. 11. K -band

**Fig. 12.** Ka -band

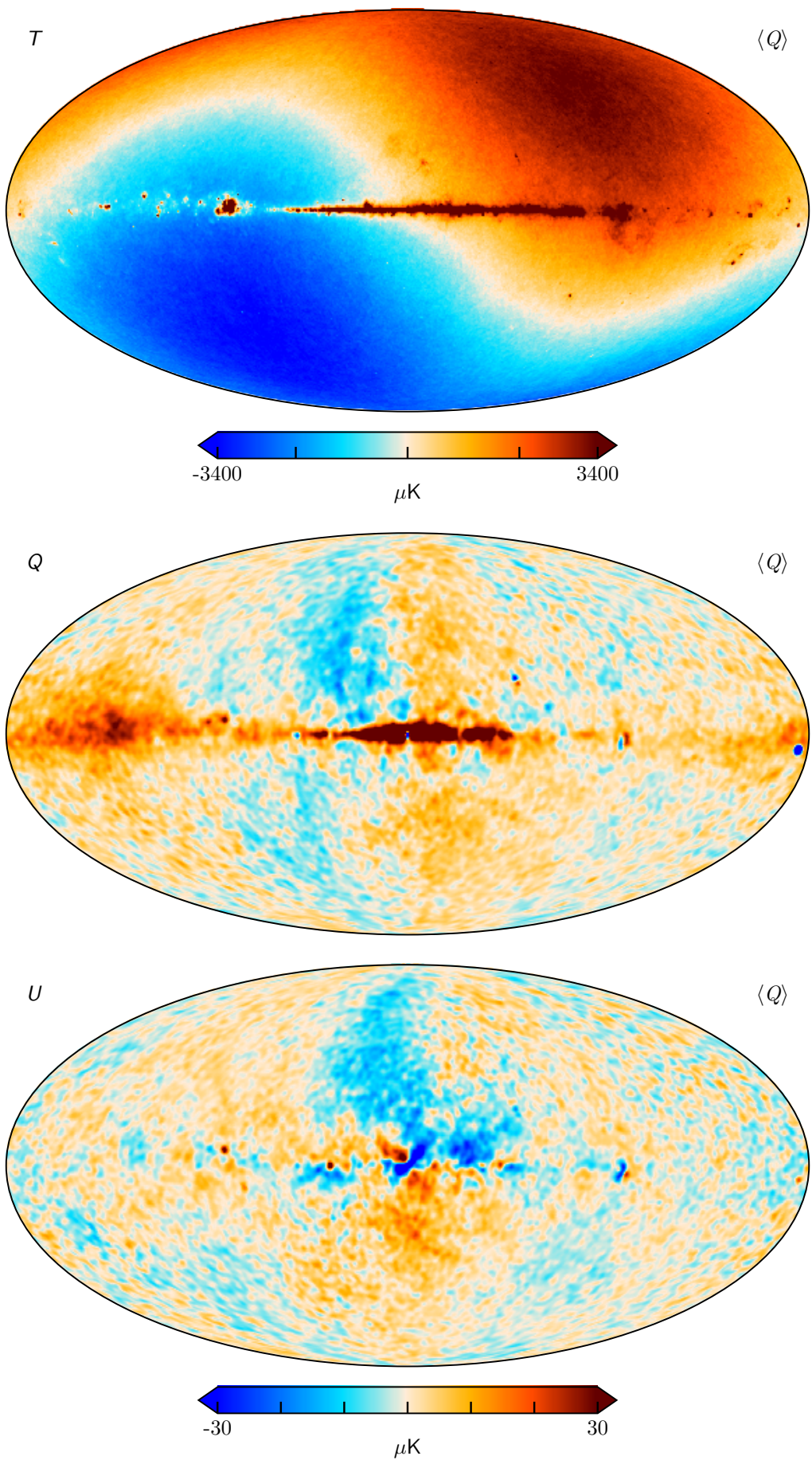


Fig. 13. Q -band

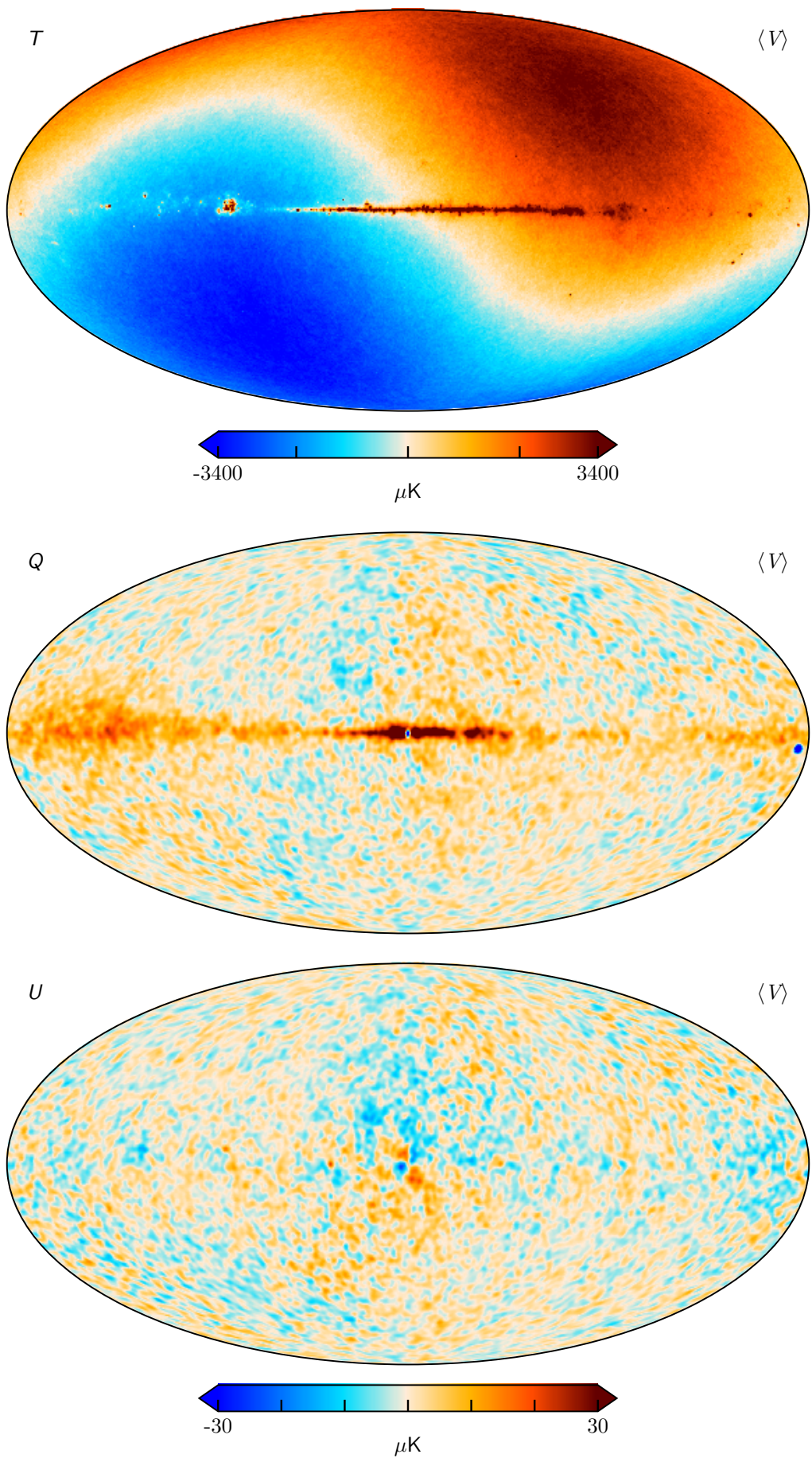


Fig. 14. V -band

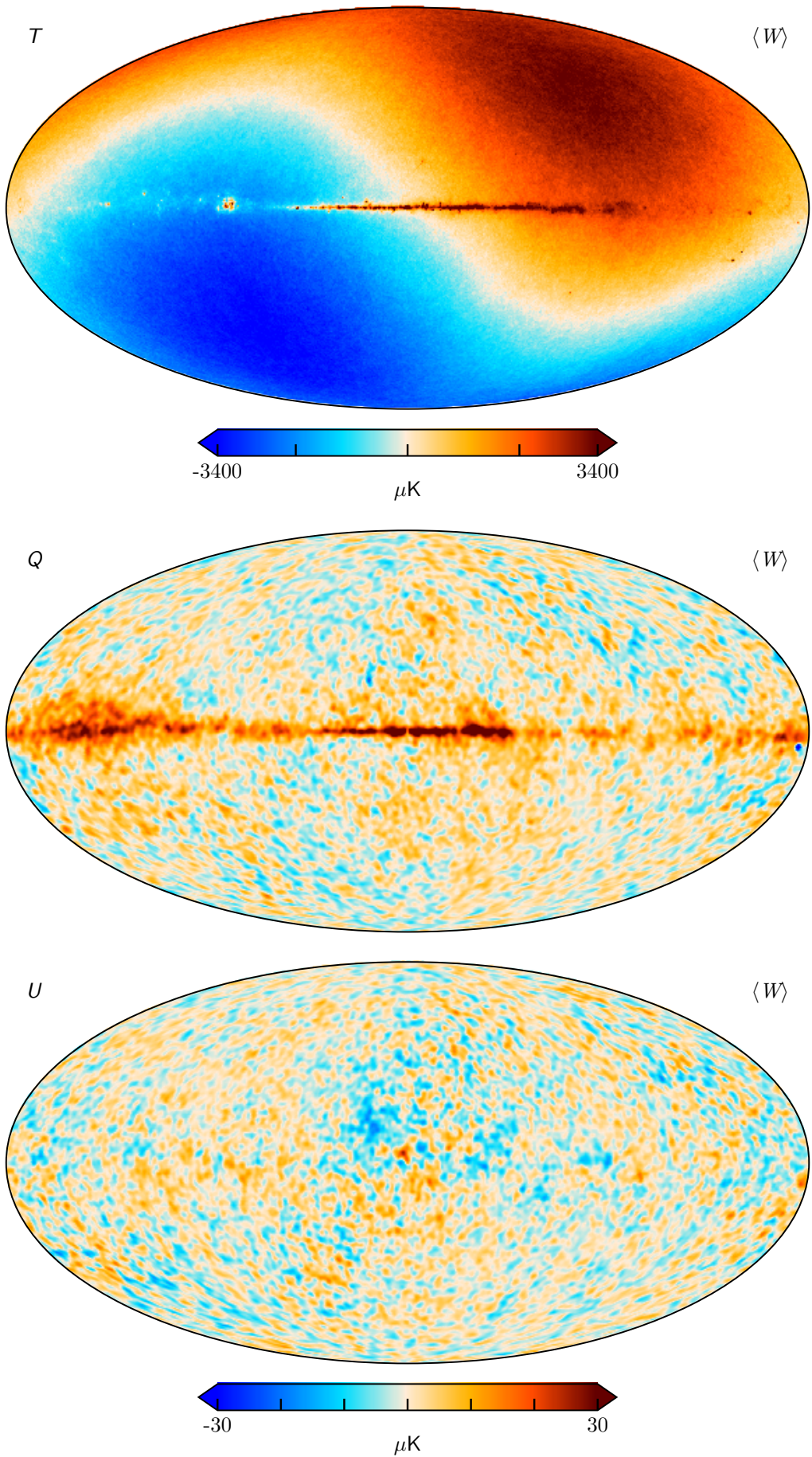
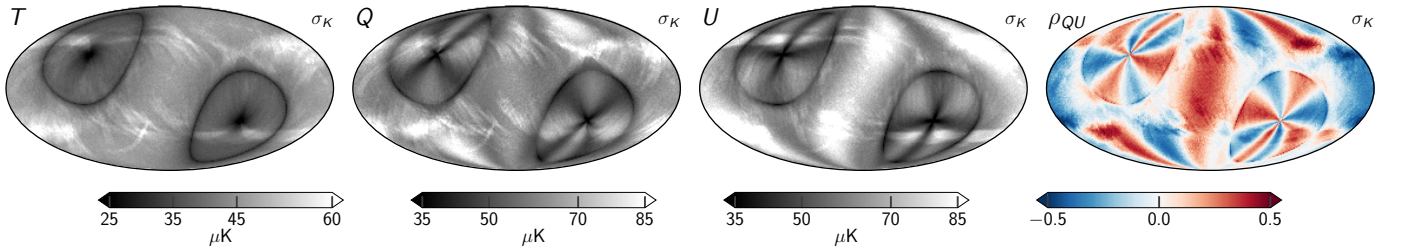
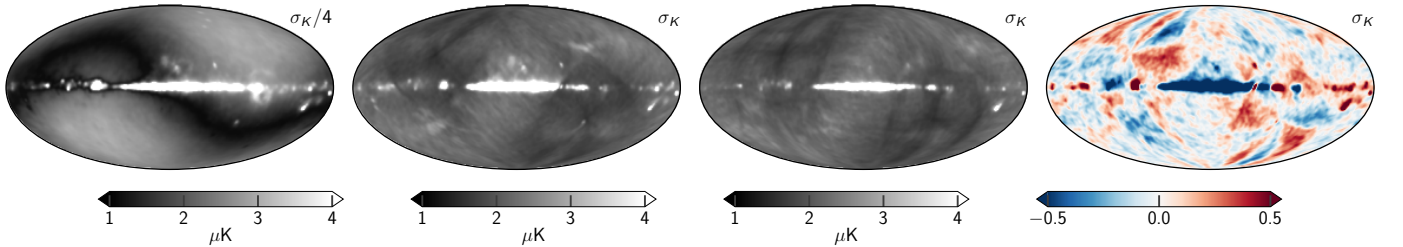


Fig. 15. W -band

Article number, page 20 of 49

**Fig. 16.** RMS**Fig. 17.** Kstd**Table 4.** Difference map χ^2 statistics.

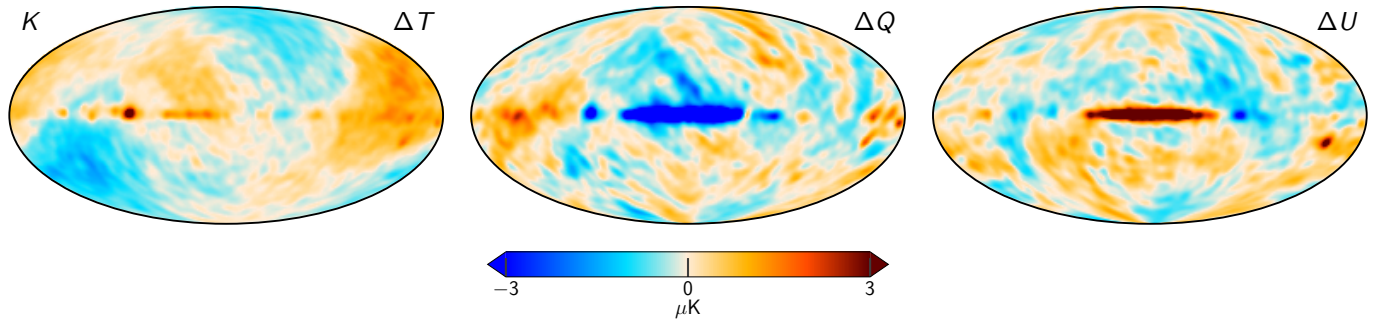
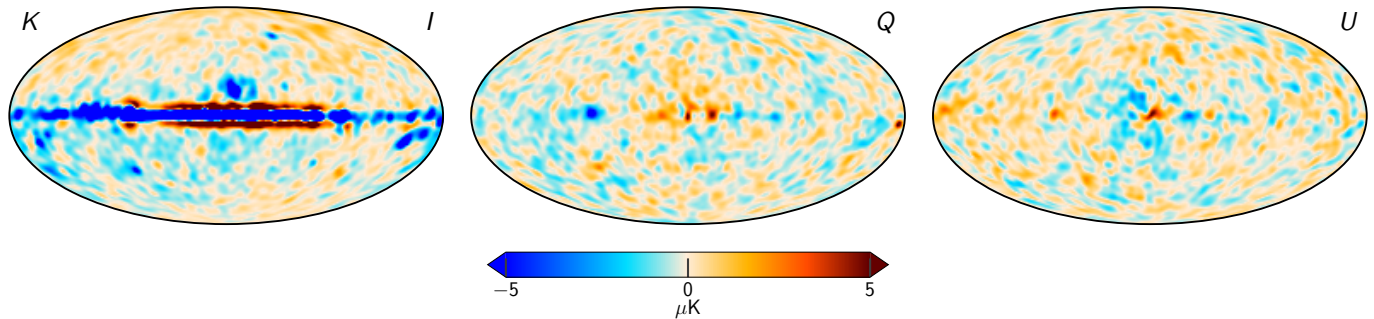
DIFFERENCE	χ^2_{uncorr}	χ^2_{corr}	$\Delta\chi^2$
0.32×K1 – Ka1 . . .	4291	4287	4
Q1 – Q2	4500	4380	120
V1 – V2	4490	4429	61
W1 – W2	4328	4270	68
W3 – W4	4257	4145	112

Table 5. Transmission imbalance template amplitudes for each WMAP radiometer as estimated by fitting the official templates to low-resolution difference maps between COSMOGLOBE and WMAP. The templates are provided in mK, and the template amplitudes are therefore dimensionless. The fourth column lists the relative decrease in standard deviation, $\sqrt{\sigma_{\text{raw}}^2 - \sigma_{\text{corr}}^2}/\sigma_{\text{raw}}$, after subtracting the best-fit templates in percent.

DA	a_1	a_2	$\Delta\sigma[\%]$
K1	-27.5	-50.6	30
Ka1	-1.4	-1.9	25
Q1	-30.0	-71.6	11
Q2	-7.1	-1.5	20
V1	-32.8	-53.4	6
V2	8.8	-4.1	16
W1	-2.8	4.6	8
W2	-6.9	-3.5	11
W3	29.1	53.4	12
W4	15.5	-6.8	52

How much off-diagonal pixel covariance is there here?

dense noise covariance matrix also explicitly projected out the poorly-measured imbalance modes, but because we find no trace of these modes in our sky maps or residual maps, this treatment is not necessary in our approach. However, the correlation between Stokes Q and U was not taken into account in the BEYONDPLANCK LFI analysis. This was not a significant oversight in the LFI analysis because the 30 and 70 GHz maps only had a 10% correlation, and 44 GHz's 50% correlation was subdominant to other systematic effects. We have updated Commander3 to take QU correlation into account for LFI.

**Fig. 18.** K sample diff**Fig. 19.** K residual

6.2. Comparison with 9-year WMAP maps

6.3. Consistency within WMAP channels

6.4. Consistency between WMAP and LFI

6.5. Preliminary CMB results

6.5.1. CMB Solar dipole

6.5.2. Temperature power spectrum

6.5.3. Preliminary large-scale CMB polarization results

6.6. Signal-to-noise ratio comparison between WMAP and LFI

7. Systematic error corrections and uncertainties

7.1. Sky map corrections

7.2. Power spectrum residuals

8. Outstanding issues

8.1. Noise modelling

8.2. V-band quadrupole residual

8.3. Degeneracy between K -band calibration and AME dipole

8.4. Other minor effects

8.4.1. Time-variable bandpass modelling

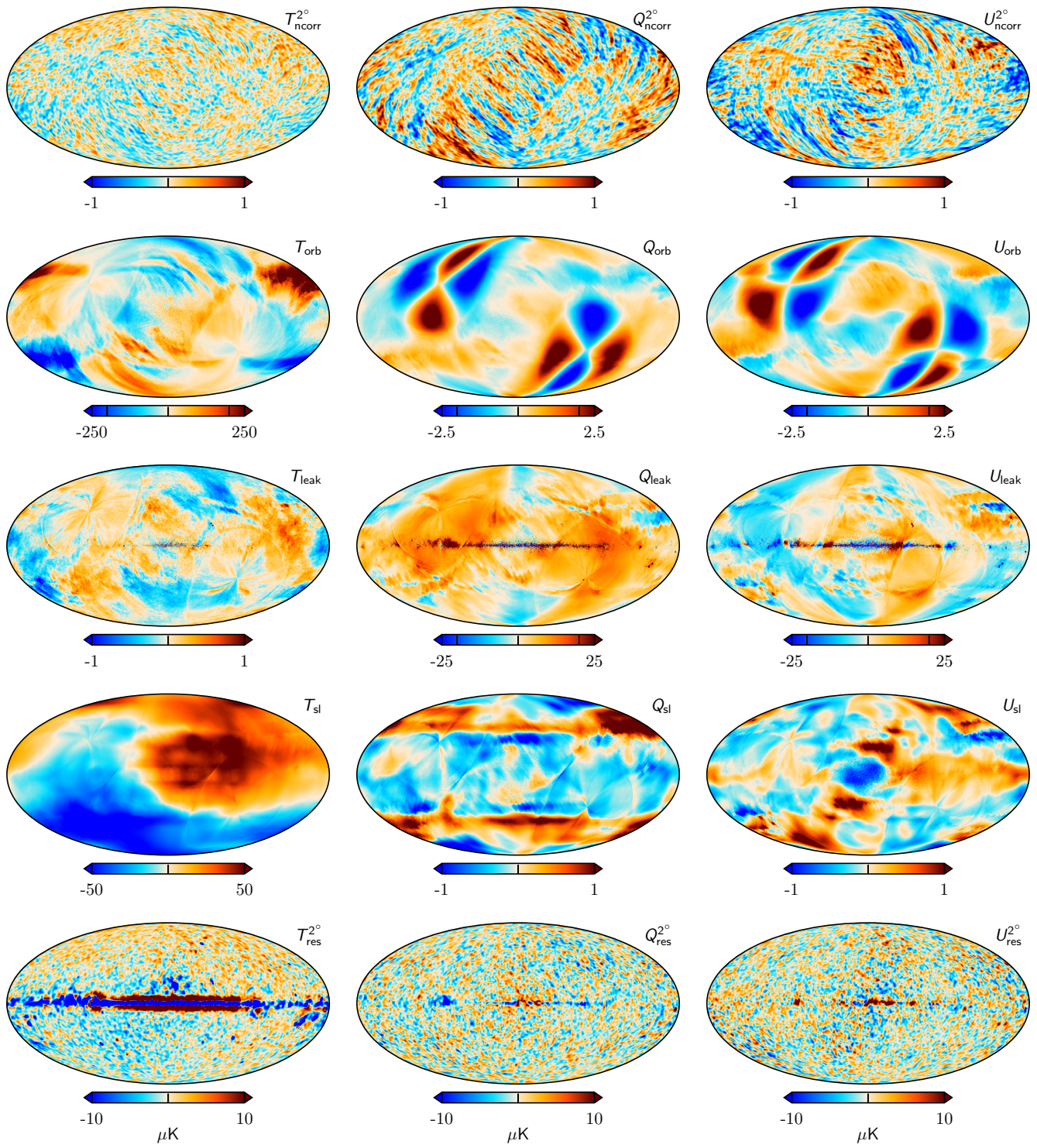
8.4.2. Polarized sidelobe modelling

9. Conclusions

References

Ali-Haïmoud, Y. 2010, Astrophysics Source Code Library [ascl:1010.016]

- Ali-Haïmoud, Y., Hirata, C. M., & Dickinson, C. 2009, MNRAS, 395, 1055
 Andersen et al. 2022, A&A, in press [arXiv:2201.08188]
 Barnes, C., Hill, R. S., Hinshaw, G., et al. 2003, ApJS, 148, 51
 Barrett, R., Berry, M. W., Chan, T. F., et al. 1994, Templates for the Solution of Linear Systems (Society for Industrial and Applied Mathematics)
 Basyrov et al. 2022, A&A, submitted [arXiv:2208.14293]
 Bennett, C. L., Bay, M., Halpern, M., et al. 2003a, ApJ, 583, 1
 Bennett, C. L., Halpern, M., Hinshaw, G., et al. 2003b, ApJS, 148, 1
 Bennett, C. L., Larson, D., Weiland, J. L., et al. 2013, ApJS, 208, 20
 BeyondPlanck. 2022, A&A, submitted [arXiv:2011.05609]
 de la Hoz, E., Barreiro, R. B., Vielva, P., et al. 2023, MNRAS, 519, 3504
 Dicke, R. H., Peebles, P. J. E., Roll, P. G., & Wilkinson, D. T. 1965, ApJ, 142, 414
 Eriksen, H. K., Dickinson, C., Lawrence, C. R., et al. 2006, ApJ, 641, 665
 Eriksen, H. K., Jewell, J. B., Dickinson, C., et al. 2008, ApJ, 676, 10
 Eriksen, H. K., O'Dwyer, I. J., Jewell, J. B., et al. 2004, ApJS, 155, 227
 Frigo, M. & Johnson, S. G. 2005, Proceedings of the IEEE, 93, 216, special issue on "Program Generation, Optimization, and Platform Adaptation"
 Galloway et al. 2022, A&A, in press [arXiv:2201.03509]
 Gjerløw et al. 2022, A&A, submitted [arXiv:2011.08082]
 Greason, M. R., Limon, M., Wollack, E., et al. 2012, Nine-Year Explanatory Supplement, 5th edn., Greenbelt, MD: NASA/GSFC
 Haslam, C. G. T., Salter, C. J., Stoffel, H., & Wilson, W. E. 1982, A&AS, 47, 1
 Hill, R. S., Weiland, J. L., Odegard, N., et al. 2009, ApJS, 180, 246
 Hinshaw, G., Barnes, C., Bennett, C. L., et al. 2003, ApJS, 148, 63
 Hinshaw, G., Nolta, M. R., Bennett, C. L., et al. 2007, ApJS, 170, 288
 Hinshaw, G., Weiland, J. L., Hill, R. S., et al. 2009, ApJS, 180, 225
 Hu, W., Fukugita, M., Zaldarriaga, M., & Tegmark, M. 2001, ApJ, 549, 669
 Ihle et al. 2022, A&A, in press [arXiv:2011.06650]
 Jarosik, N., Barnes, C., Bennett, C. L., et al. 2003a, ApJS, 148, 29
 Jarosik, N., Barnes, C., Greason, M. R., et al. 2007, ApJS, 170, 263
 Jarosik, N., Bennett, C. L., Dunkley, J., et al. 2011, ApJS, 192, 14
 Jarosik, N., Bennett, C. L., Halpern, M., et al. 2003b, ApJS, 145, 413
 Jewell, J., Levin, S., & Anderson, C. H. 2004, ApJ, 609, 1
 Keihänen et al. 2022, A&A, in press [arXiv:2011.06024]
 Lange, A. E., Ade, P. A., Bock, J. J., et al. 2001, Phys. Rev. D, 63, 042001
 Mather, J. C., Cheng, E. S., Cottingham, D. A., et al. 1994, ApJ, 420, 439
 Mather, J. C., Fixsen, D. J., Shafer, R. A., Mosier, C., & Wilkinson, D. T. 1999, ApJ, 512, 511
 Page, L., Jackson, C., Barnes, C., et al. 2003, ApJ, 585, 566
 Penzias, A. A. & Wilson, R. W. 1965, ApJ, 142, 419
 Planck Collaboration II. 2016, A&A, 594, A2
 Planck Collaboration X. 2016, A&A, 594, A10
 Planck Collaboration II. 2020, A&A, 641, A2

**Fig. 20.** Time-ordered components projected

- Planck Collaboration Int. XLVI. 2016, A&A, 596, A107
 Press, W. H., Teukolsky, S. A., Vetterling, W. T., & Flannery, B. P. 2007, Numerical Recipes 3rd Edition: The Art of Scientific Computing, 3rd edn. (USA: Cambridge University Press)
 Remazeilles, M., Dickinson, C., Banday, A. J., Bigot-Sazy, M.-A., & Ghosh, T. 2015, MNRAS, 451, 4311
 Rubiño-Martín, J. A., Guidi, F., Génova-Santos, R. T., et al. 2023, MNRAS, 519, 3383
 Silsbee, K., Ali-Haïmoud, Y., & Hirata, C. M. 2011, MNRAS, 411, 2750
 Smoot, G. F., Bennett, C. L., Kogut, A., et al. 1992, ApJ, 396, L1
 Stevenson, M. A. 2014, The Astrophysical Journal, 781, 113
 Svalheim et al. 2022, A&A, in press [arXiv:2011.08503]

- Tramonte, D., Génova-Santos, R. T., Rubiño-Martín, J. A., et al. 2023, MNRAS, 519, 3432
 van der Vorst, H. A. 1992, SIAM Journal on Scientific and Statistical Computing, 13, 631
 Watts et al. 2022, A&A, in press [arXiv:2202.11979]
 Weiland, J. L., Odegard, N., Hill, R. S., et al. 2011, ApJS, 192, 19

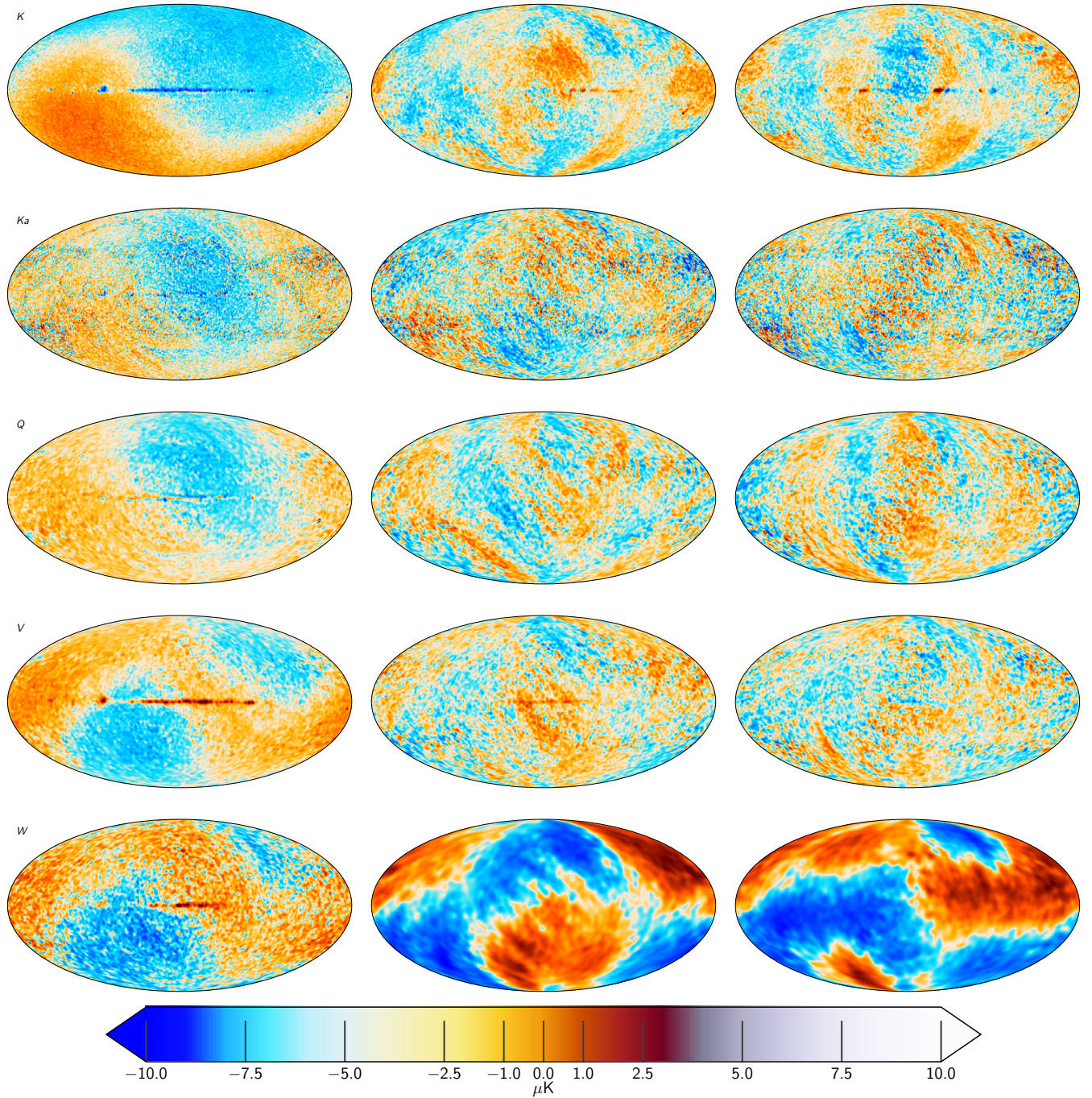
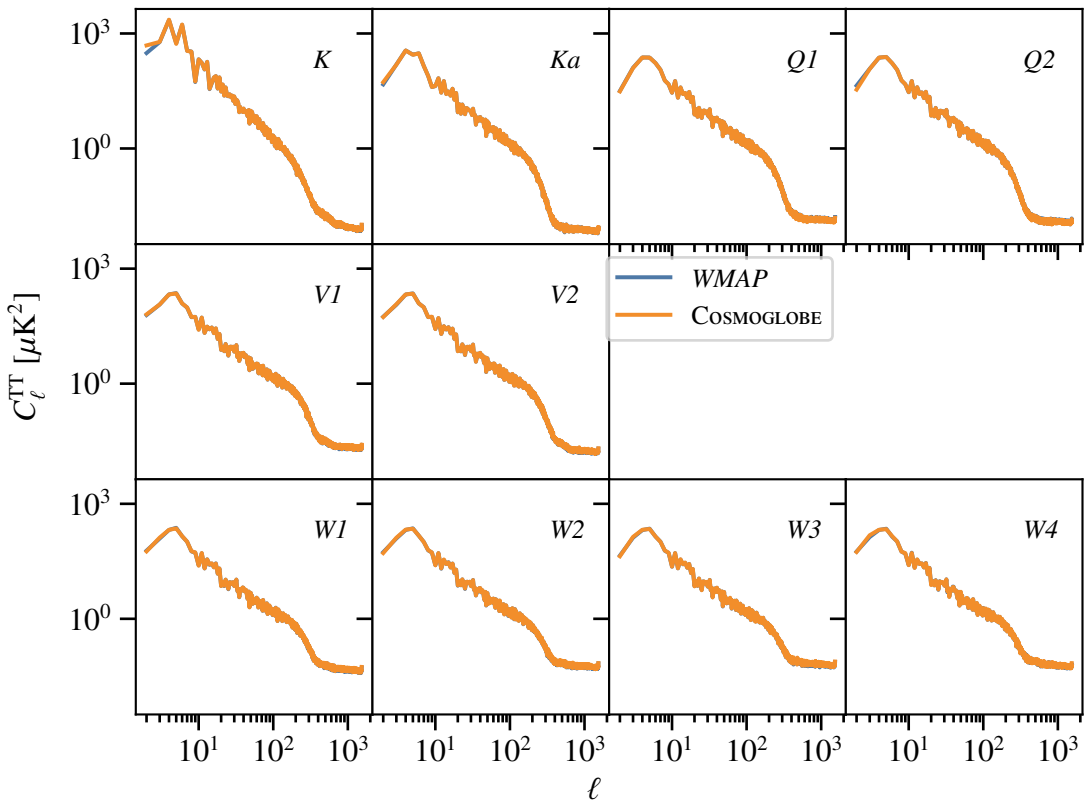
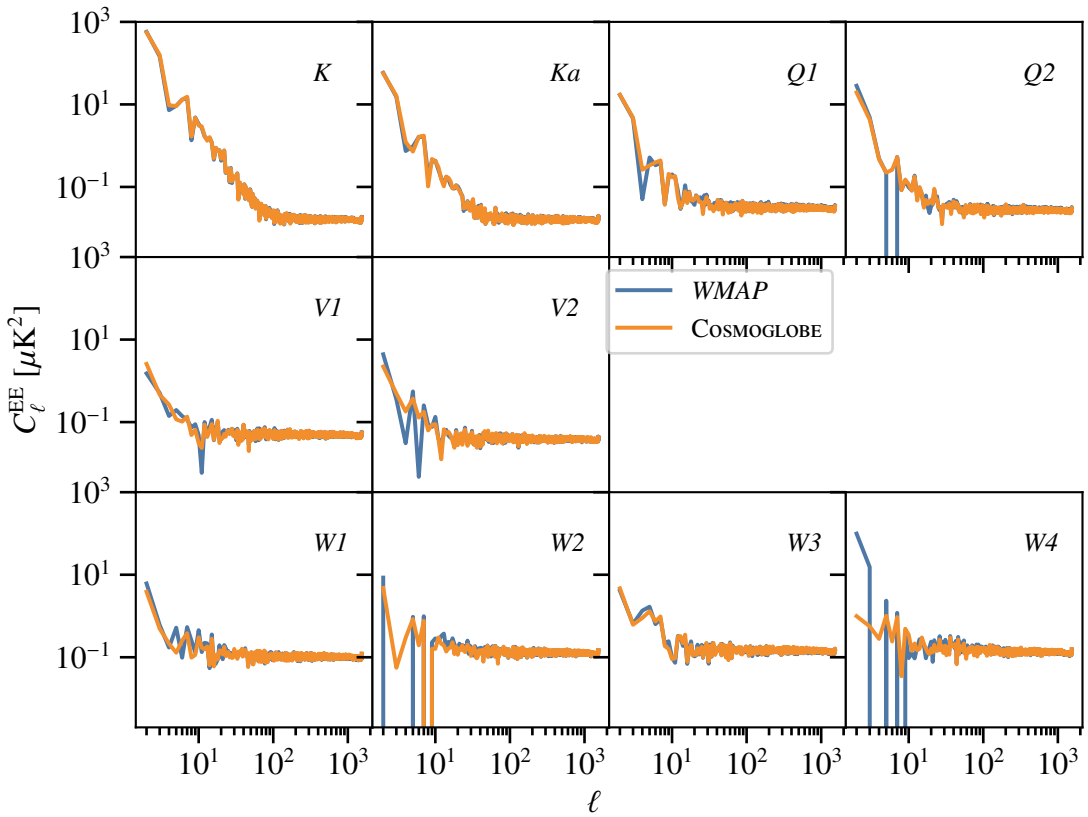
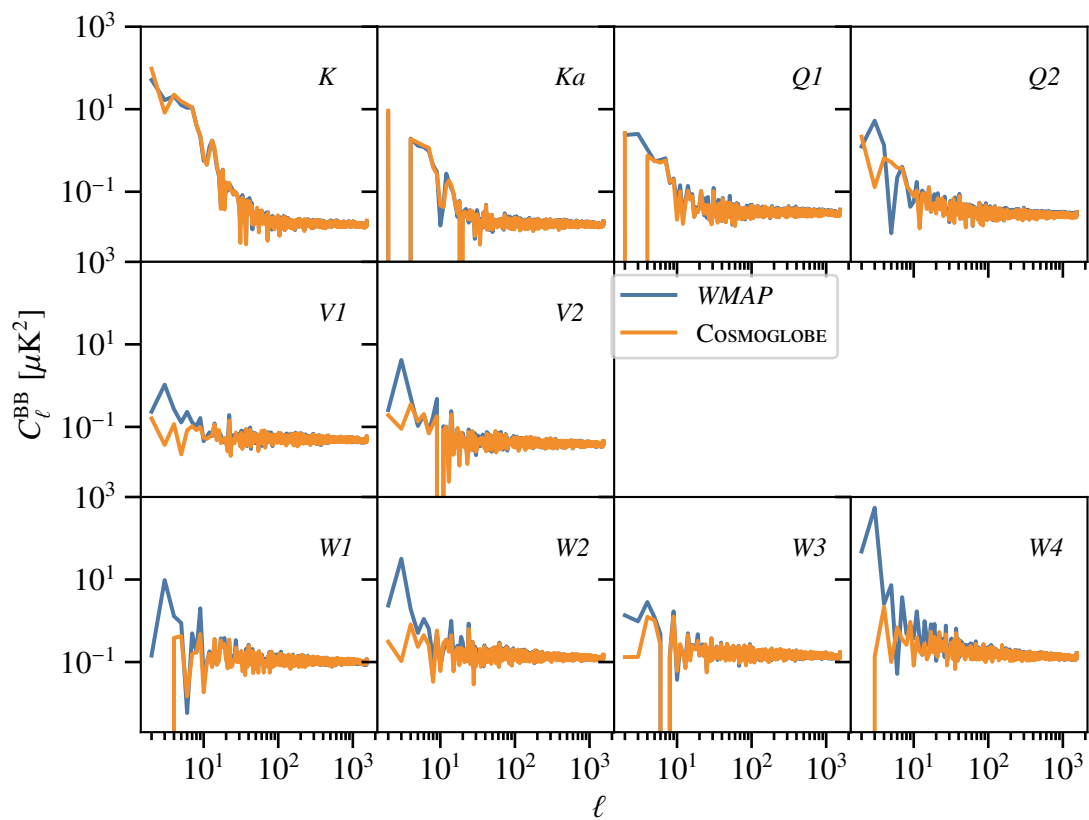
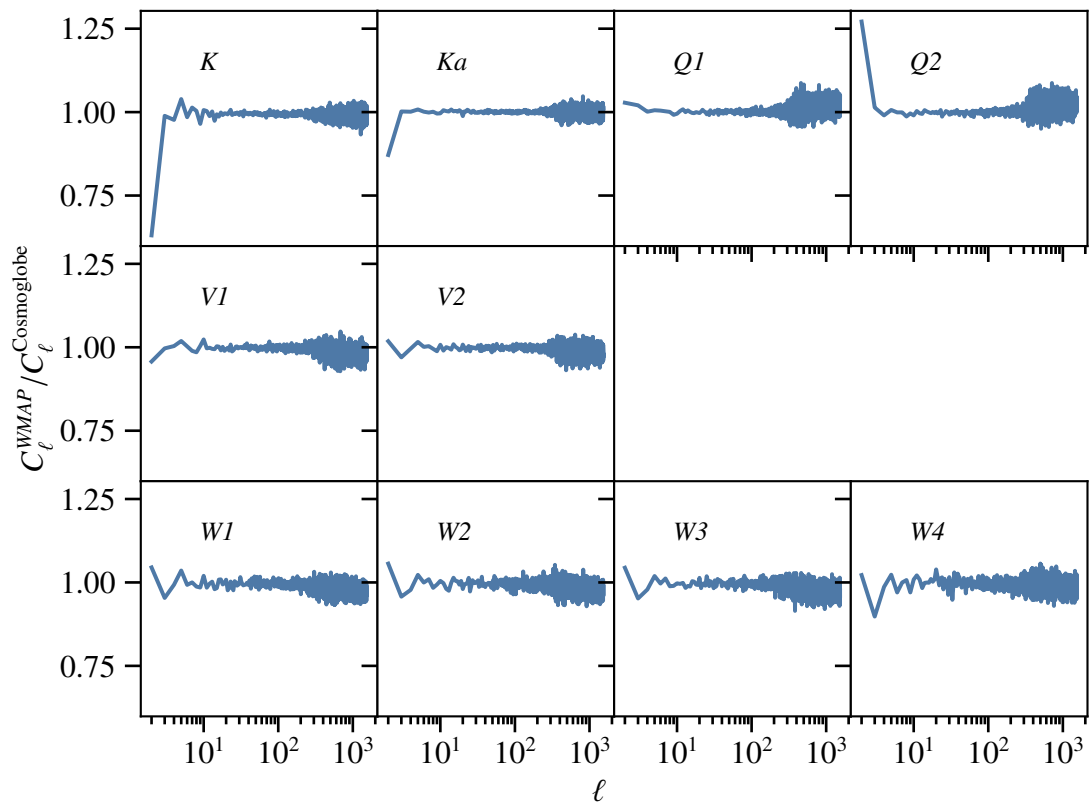
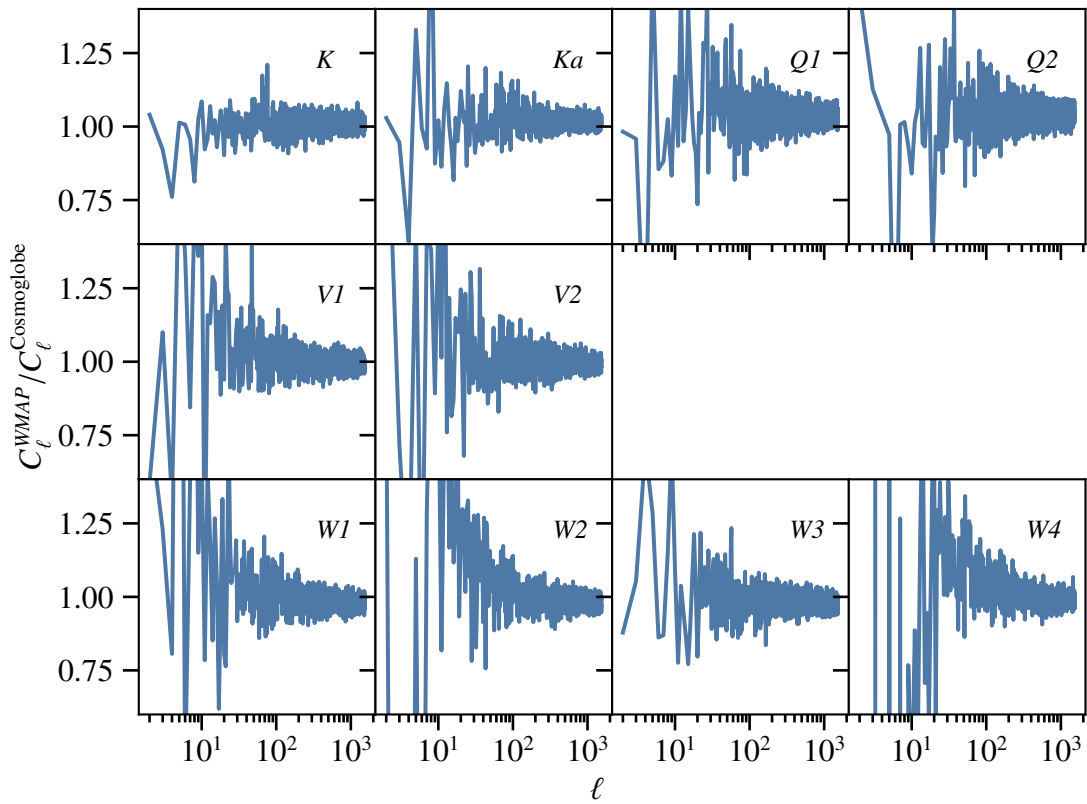
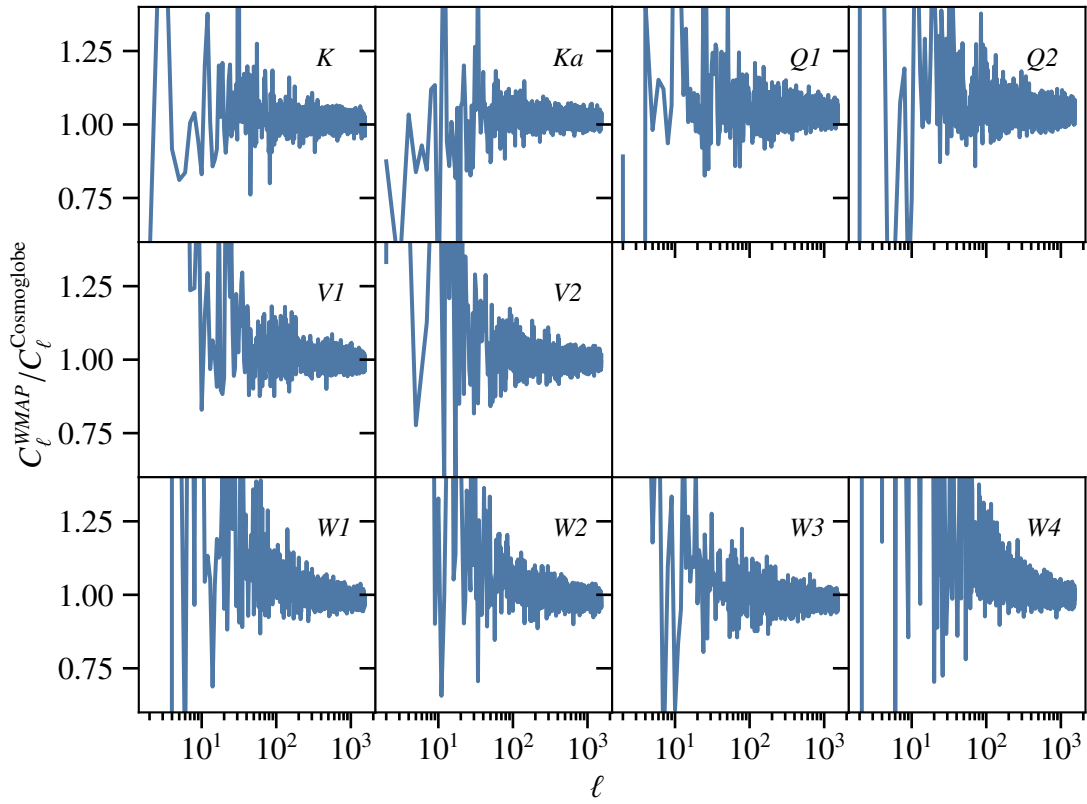


Fig. 21. Difference maps between the COSMOGLobe and 9-year *WMAP* frequency maps. Columns show Stokes T , Q , and U parameter maps, while rows show K -, Ka -, Q -, V -, and W -band maps. The temperature maps are smoothed to an angular resolution of 1° FWHM, while the polarization maps are smoothed to 5° FWHM.

**Fig. 22.** TT power spectra**Fig. 23.** EE power spectra

**Fig. 24.** BB power spectra**Fig. 25.** TT ratios

**Fig. 26.** EE ratios**Fig. 27.** BB ratios

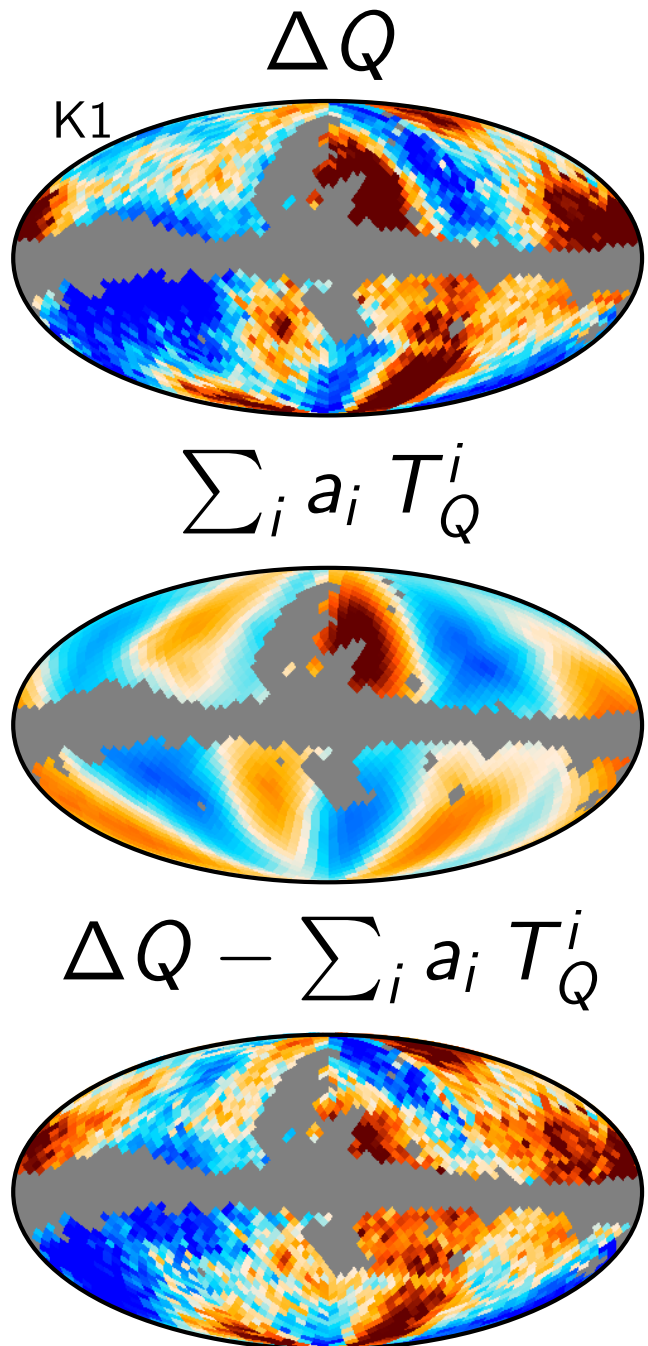
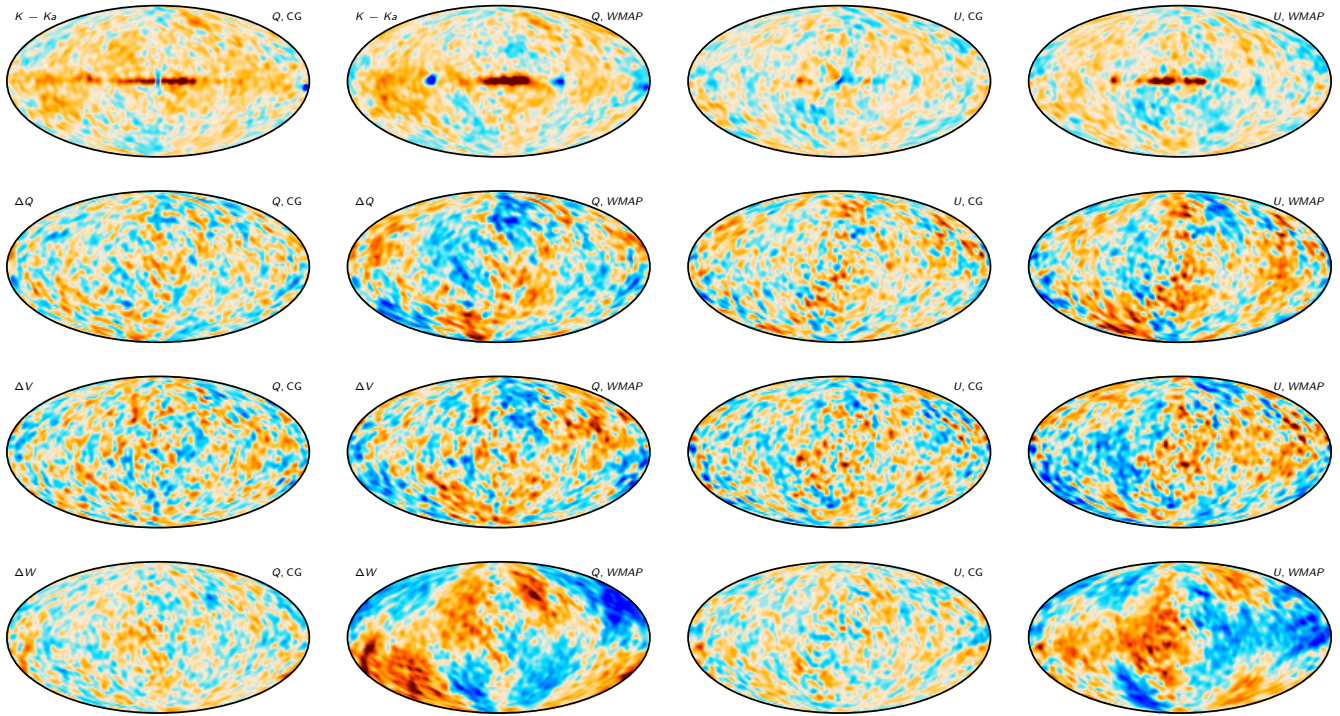
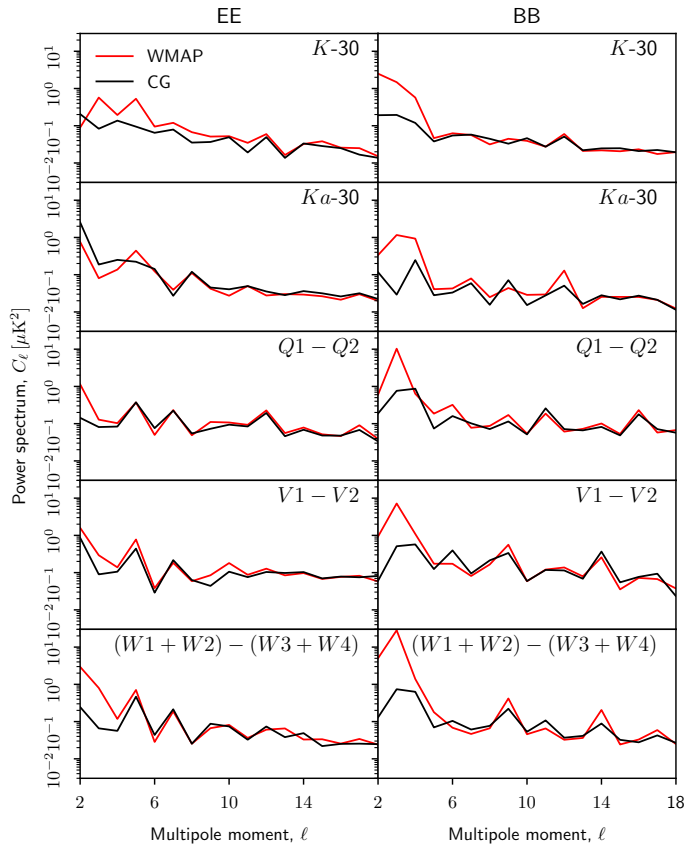


Fig. 28. K-band transmission imbalance templates

**Fig. 29.** Half-difference maps, smoothed by 10° .**Fig. 30.** Half-difference spectra.

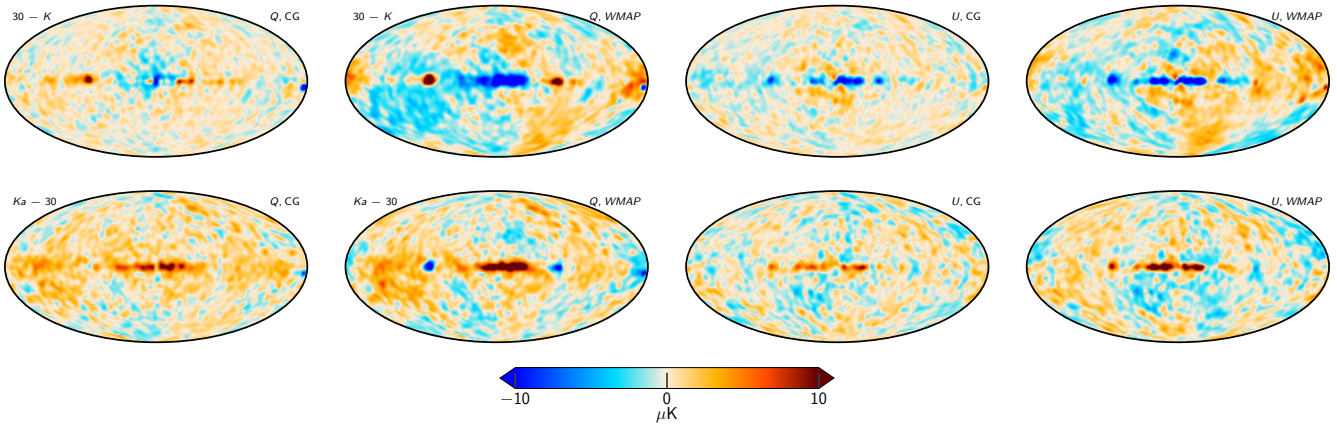
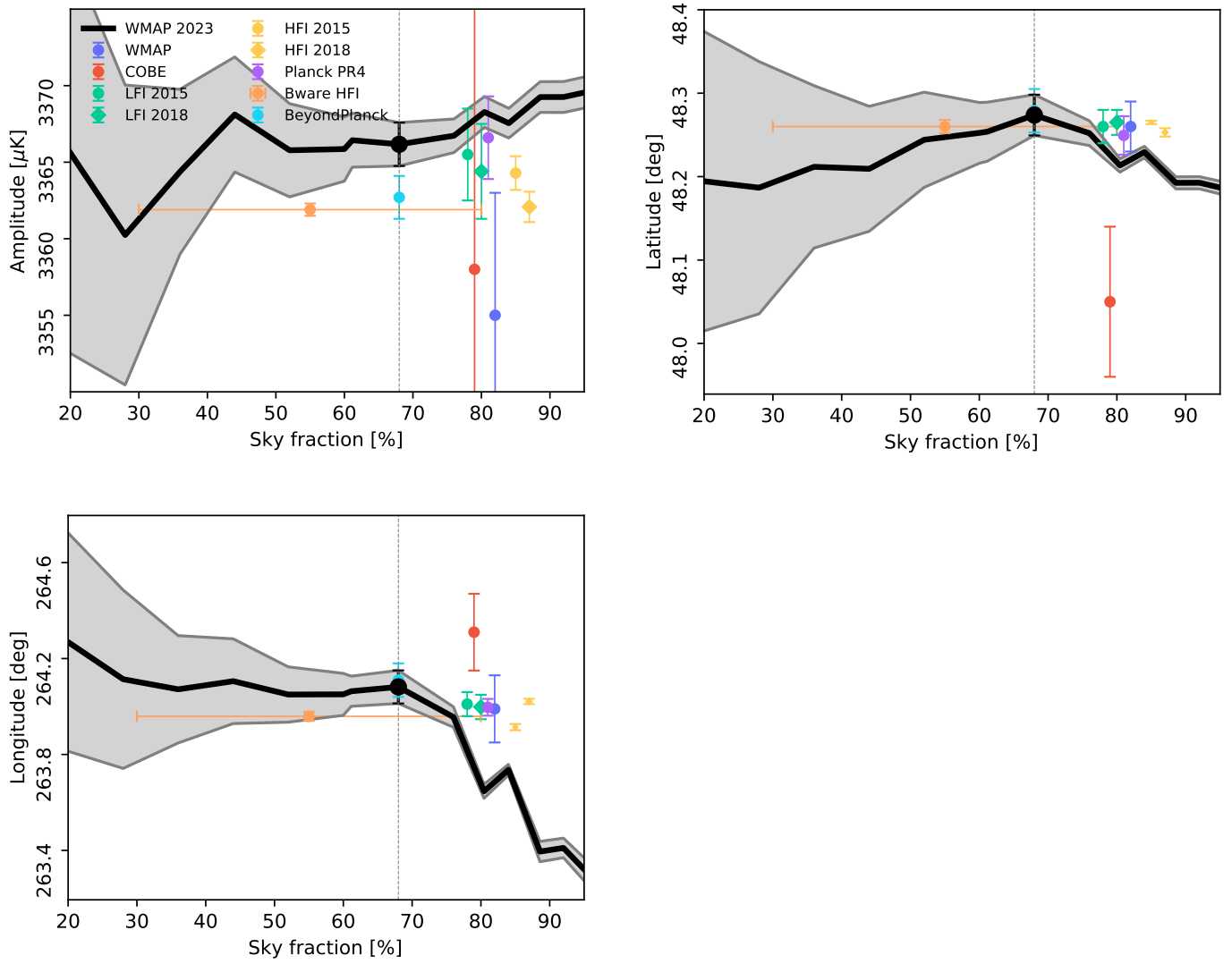
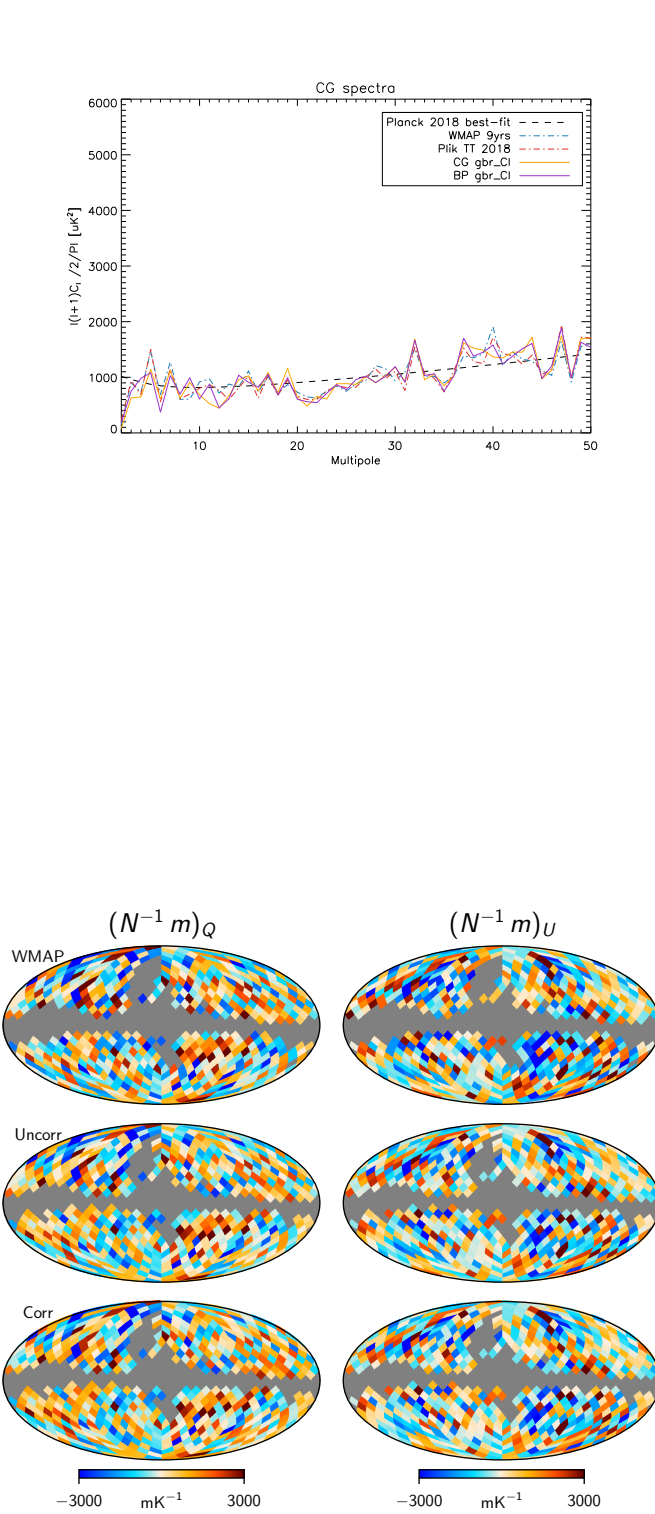
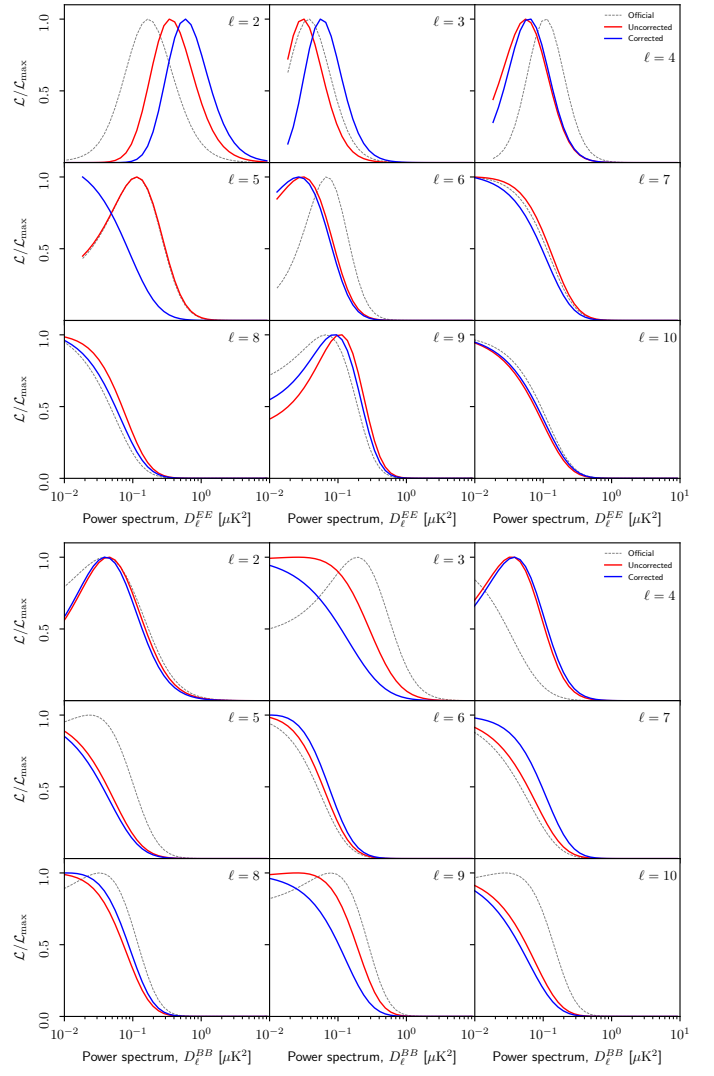


Fig. 31. Mean of WMAP+LFI bands



**Fig. 32.** Noise-weighted likelihood input maps.**Fig. 33.** Likelihood slices

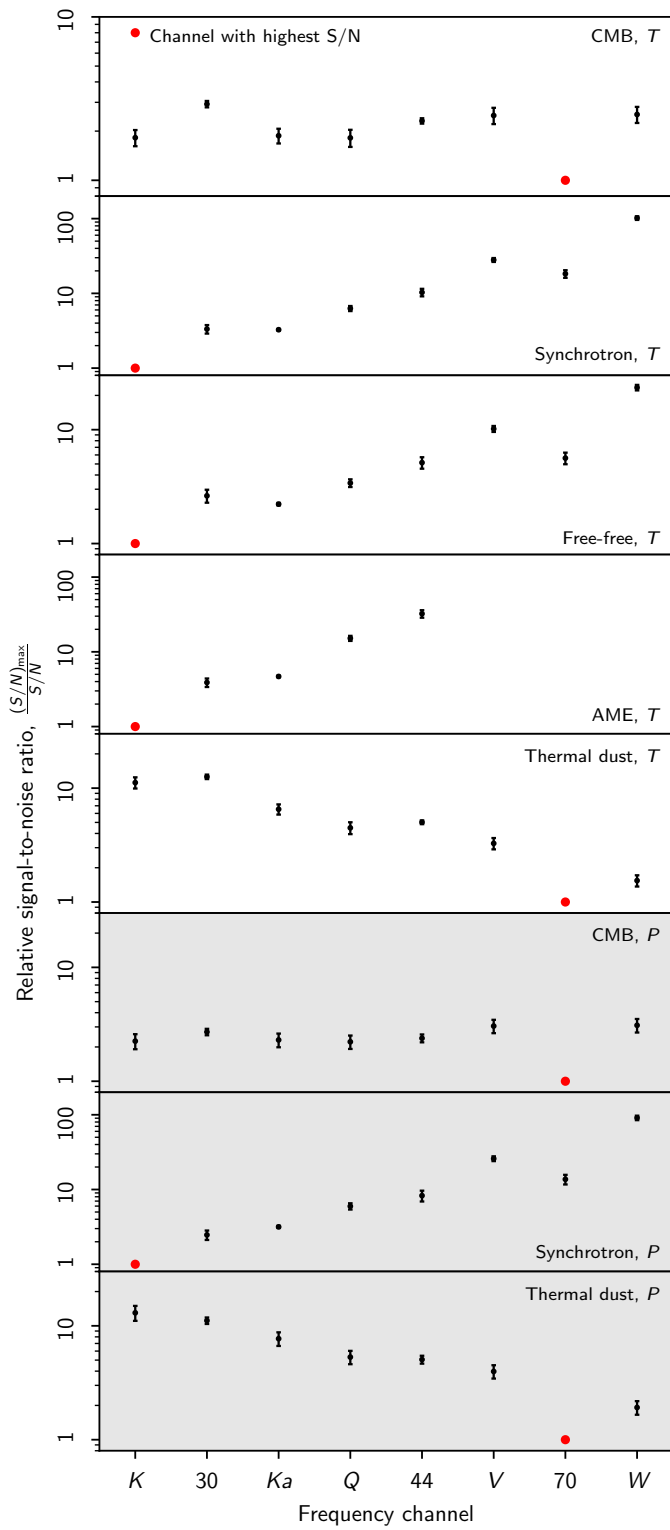


Fig. 34. Relative signal-to-noise ratios for WMAP and LFI channels and various components.

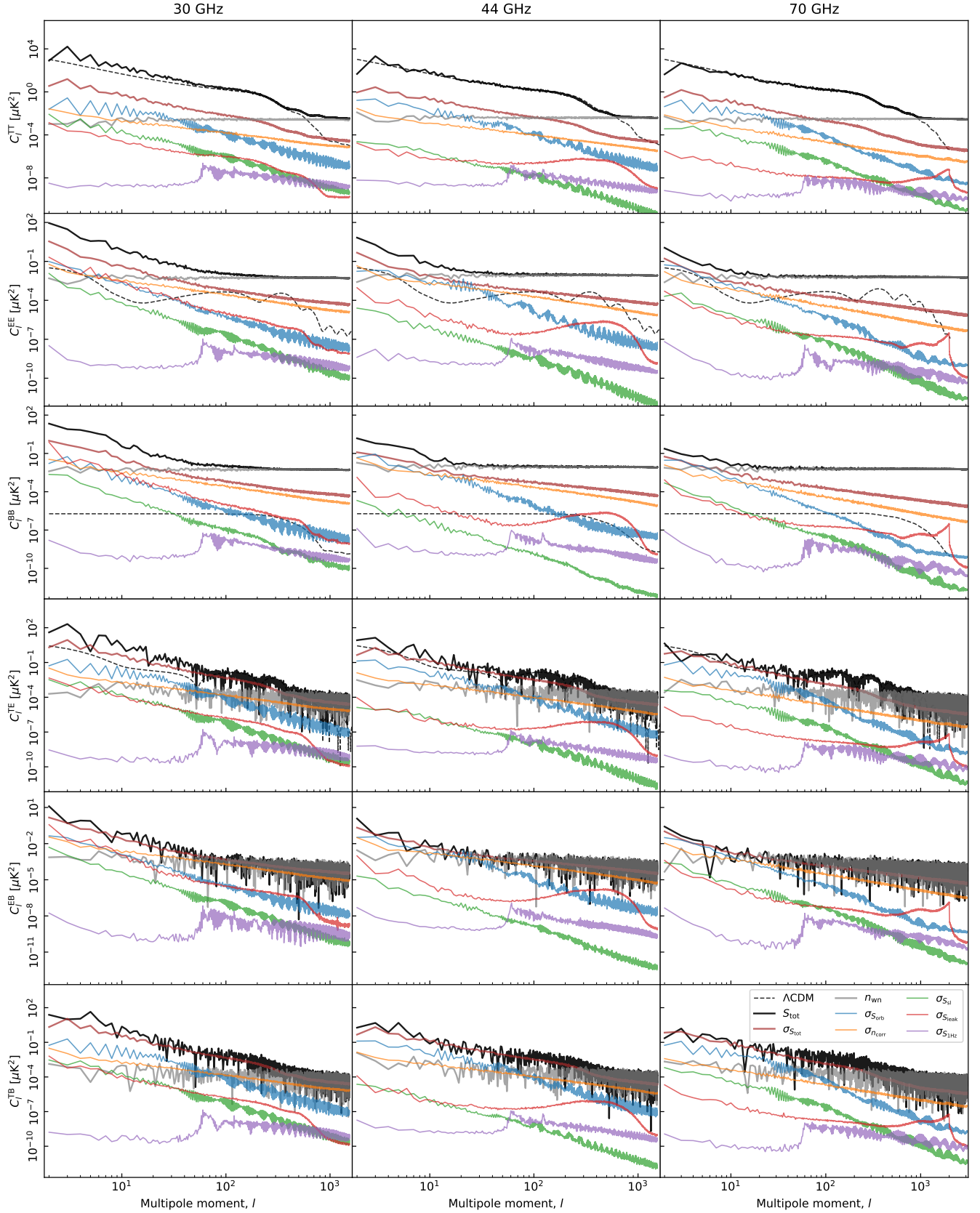


Fig. 35. Pseudo-spectrum standard deviation for each instrumental systematic correction shown in Figs. ??–?? (thin colored lines). For comparison, thick black lines show spectra for the full coadded frequency map; thick red lines show the standard deviation of the same (i.e., the full systematic uncertainty); gray lines show white noise; and dashed black lines show the best-fit *Planck* 2018 Λ CDM power spectrum convolved with the instrument beam. Columns show results for 30, 44 and 70 GHz, respectively, while rows show results for each of the six polarization states (TT, EE, BB, TE, TB, and EB). All spectra have been derived outside the CMB confidence mask presented by [Andersen et al. \(2022\)](#) using the HEALPix *anafast* utility, correcting only for sky fraction and not for mask mode coupling.

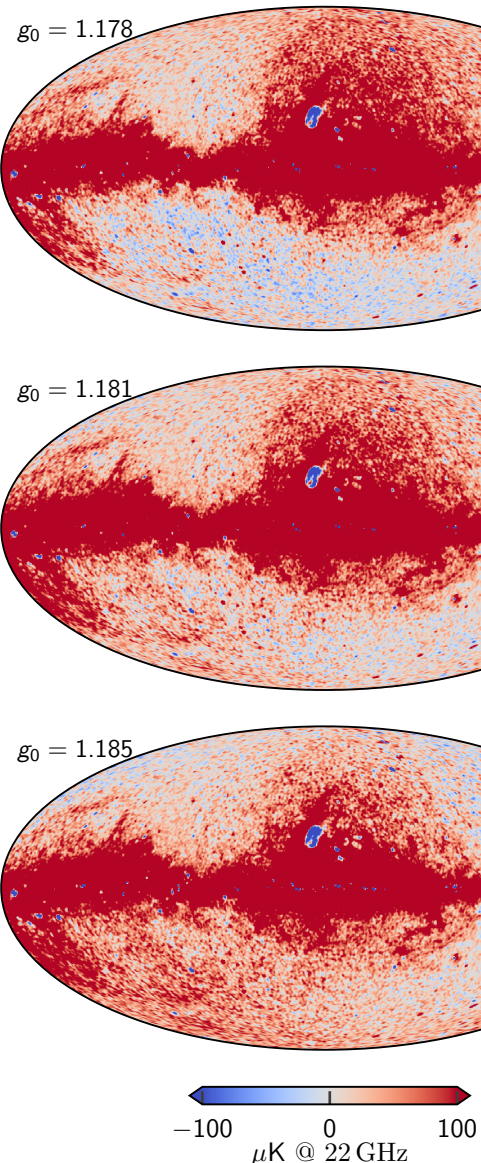


Fig. 36. Dependence on AME amplitude evaluated at 22 GHz as a function of absolute calibration. Each map comes from the fifth iteration of a dedicated `Commander` run that fixed g_0 while letting all other TOD parameters be fit. The values of $g_0 = 1.178$ and $g_0 = 1.185$ represent 3.5σ draws from the prior distribution with mean 1.1815 and standard deviation 0.001. The dipole visible in the top and bottom panels is aligned perfectly with the Solar dipole, and is directly due to variations in the K -band absolute calibration.

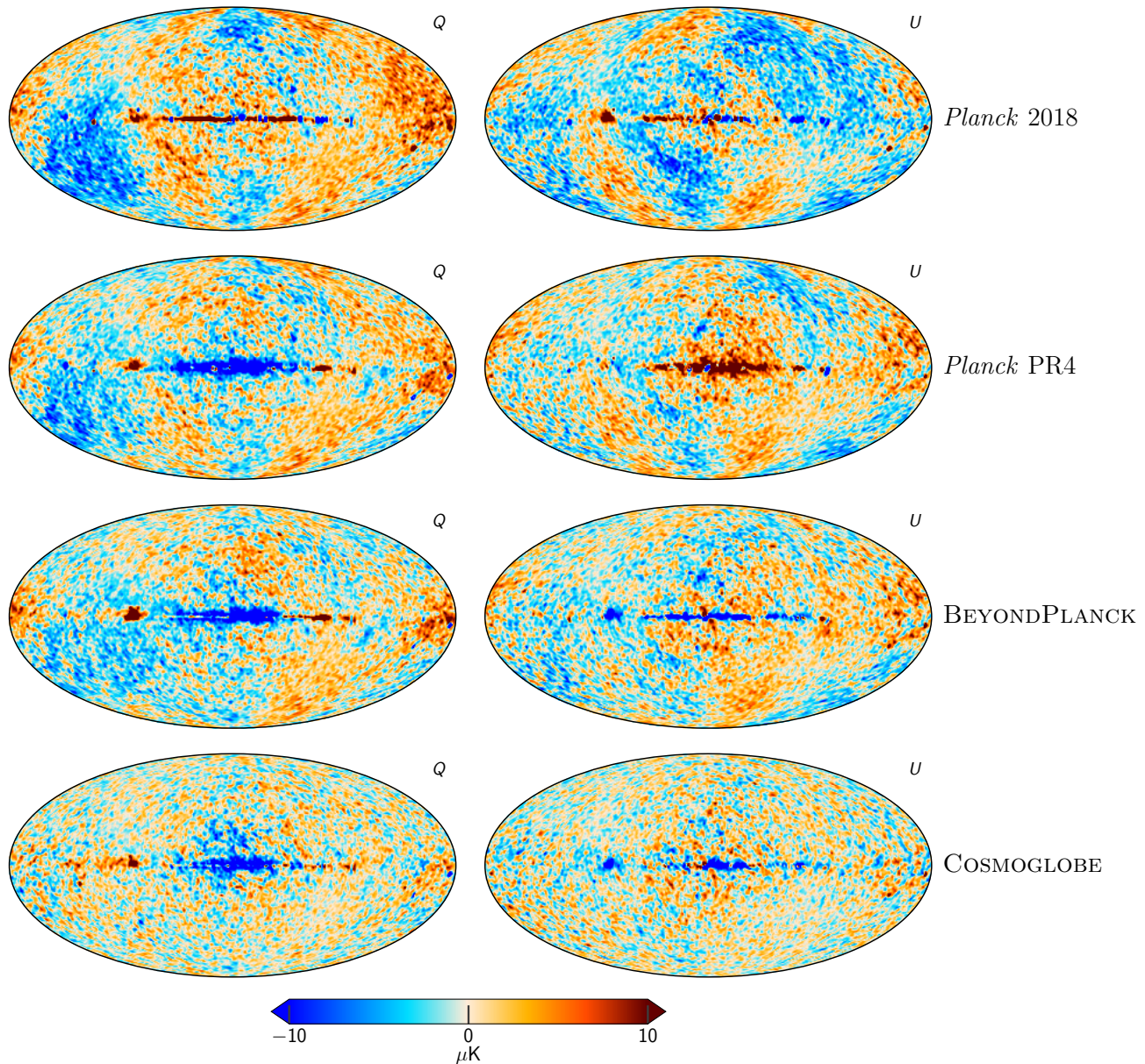


Fig. 37. Difference maps between the *Planck* 30 GHz and WMAP *K*-band maps. The columns are (1) *Planck* 2018 v. WMAP9, (2) *Planck* PR4 v. WMAP9, (3) BEYONDPLANCK v. WMAP9, and (4) COSMOGLOBE *Planck* 30 GHz and WMAP *K*-band both produced in this paper. All maps have been smoothed to a common resolution of 2° FWHM, and the *K*-band map has been scaled by 0.495 to account for different central frequencies, assuming a synchrotron spectral index $\beta_s = -3.1$.

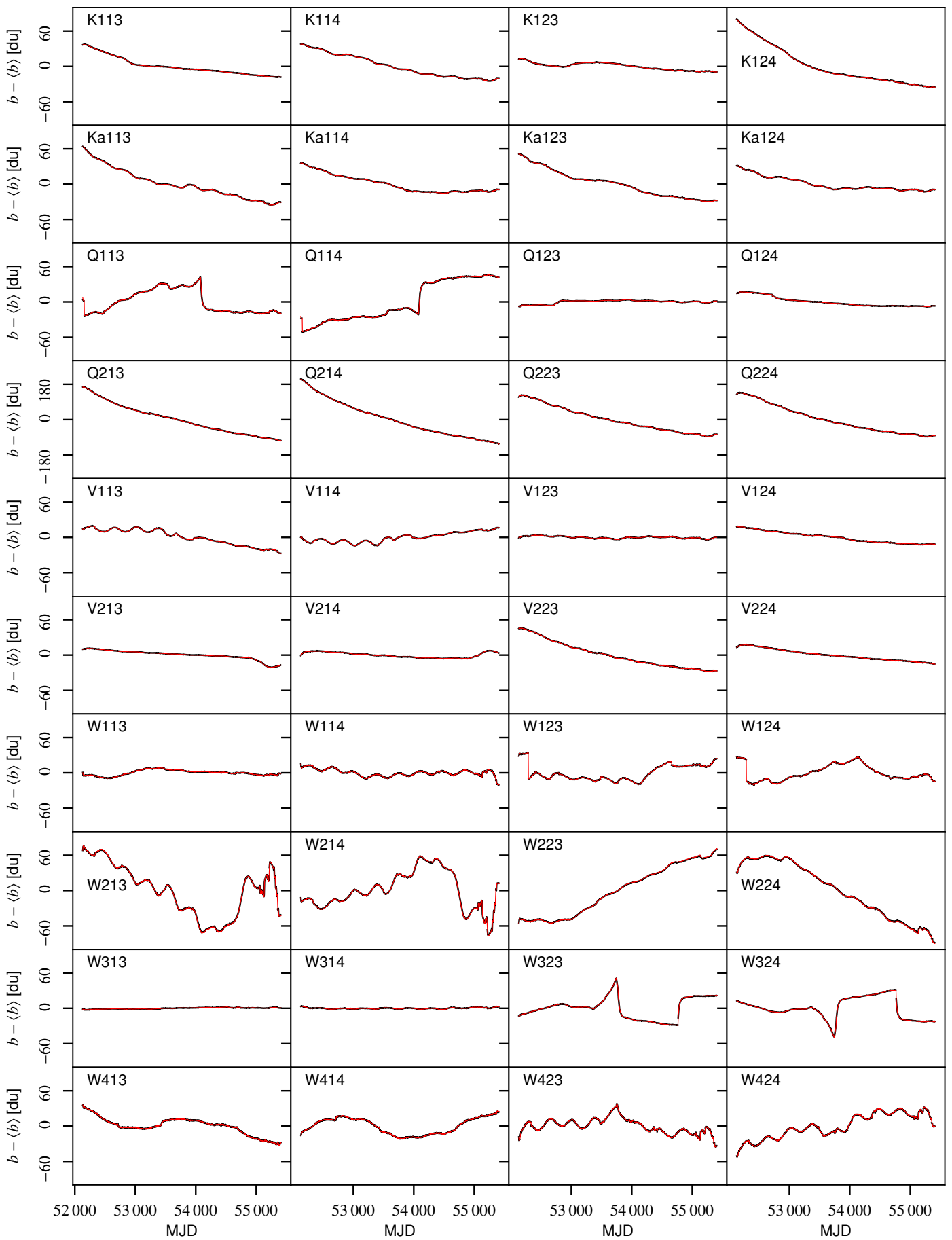
Appendix A: Survey of instrumental parameters

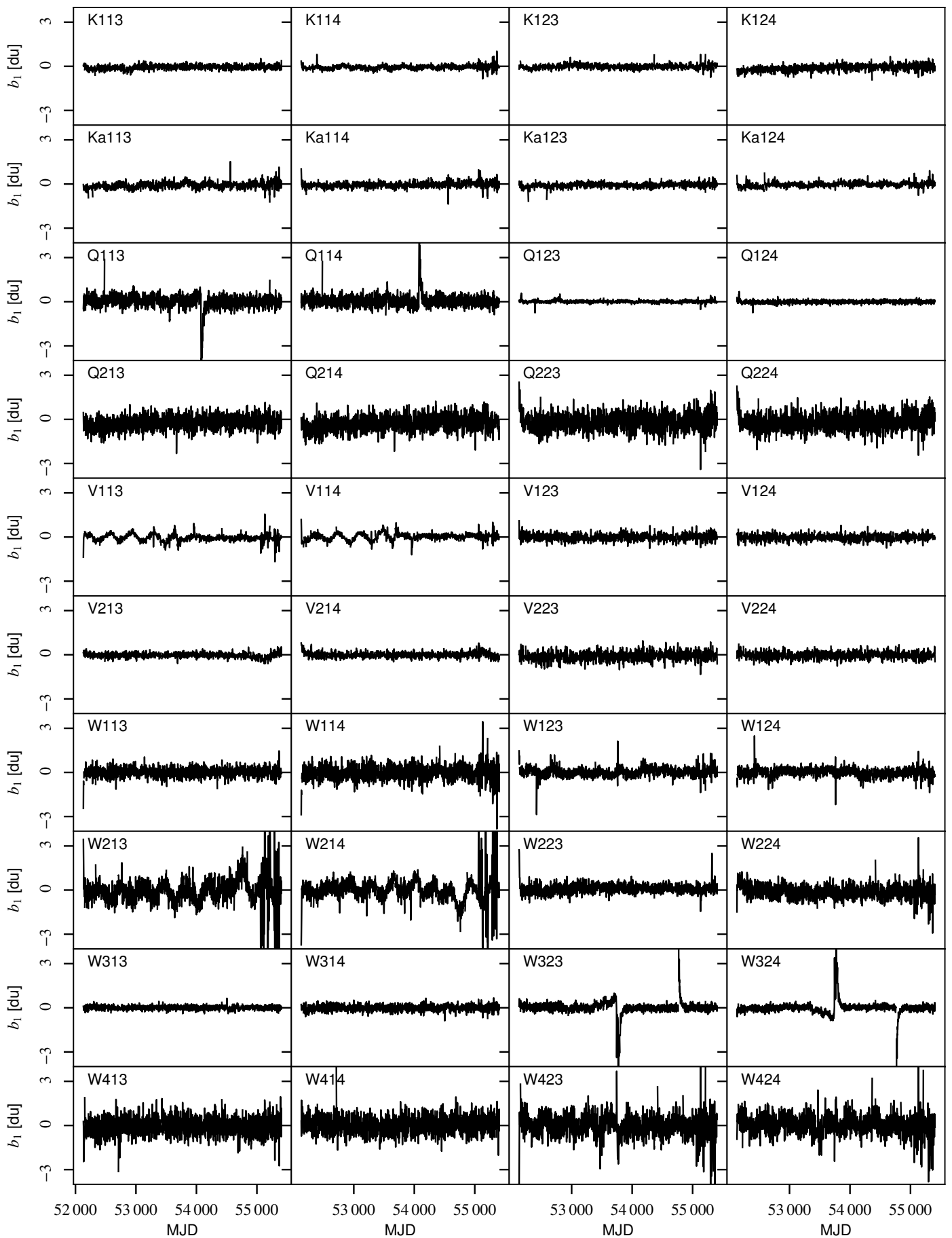
Appendix A.1: Gain, baselines, noise and χ^2

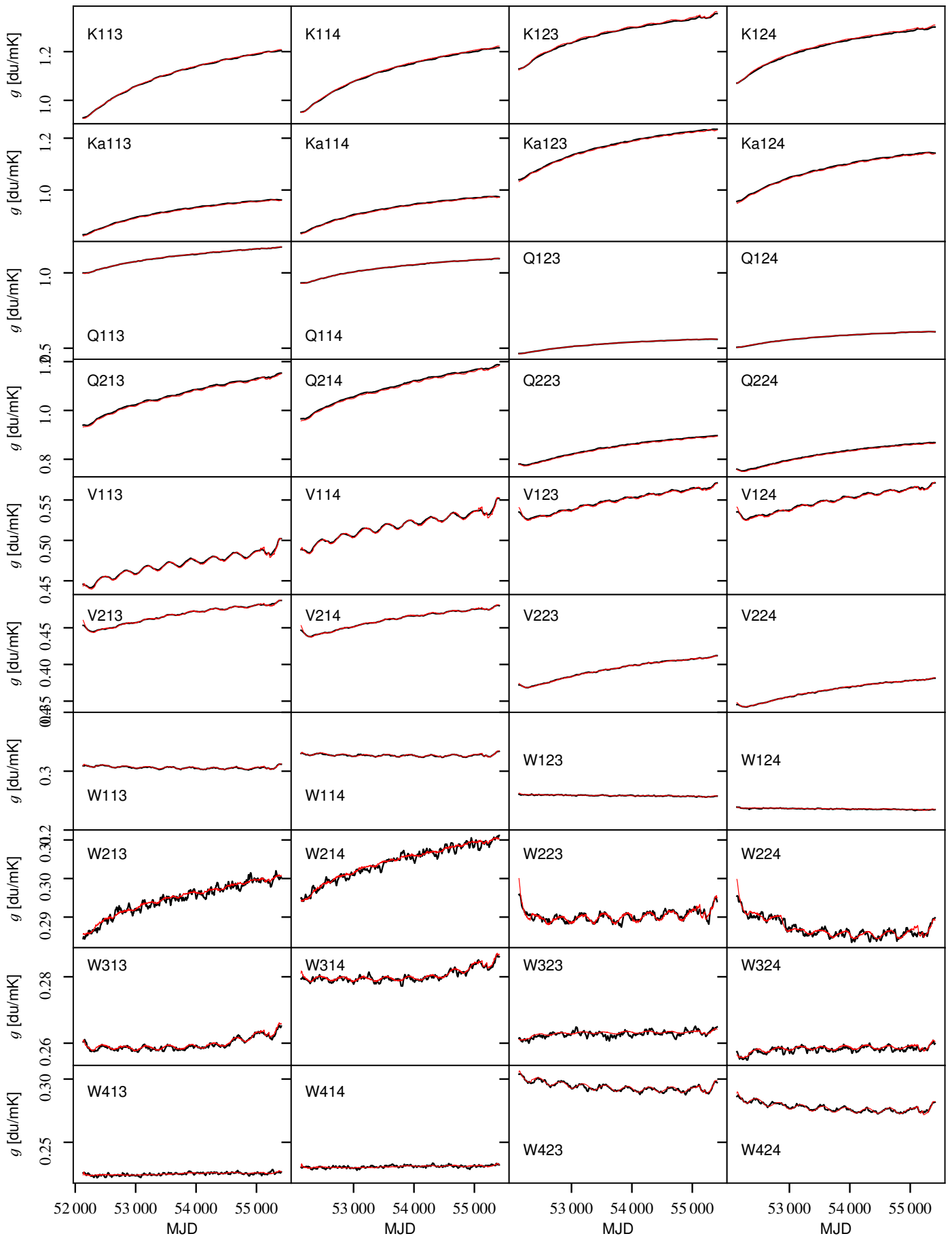
Appendix A.2: Transmission imbalance

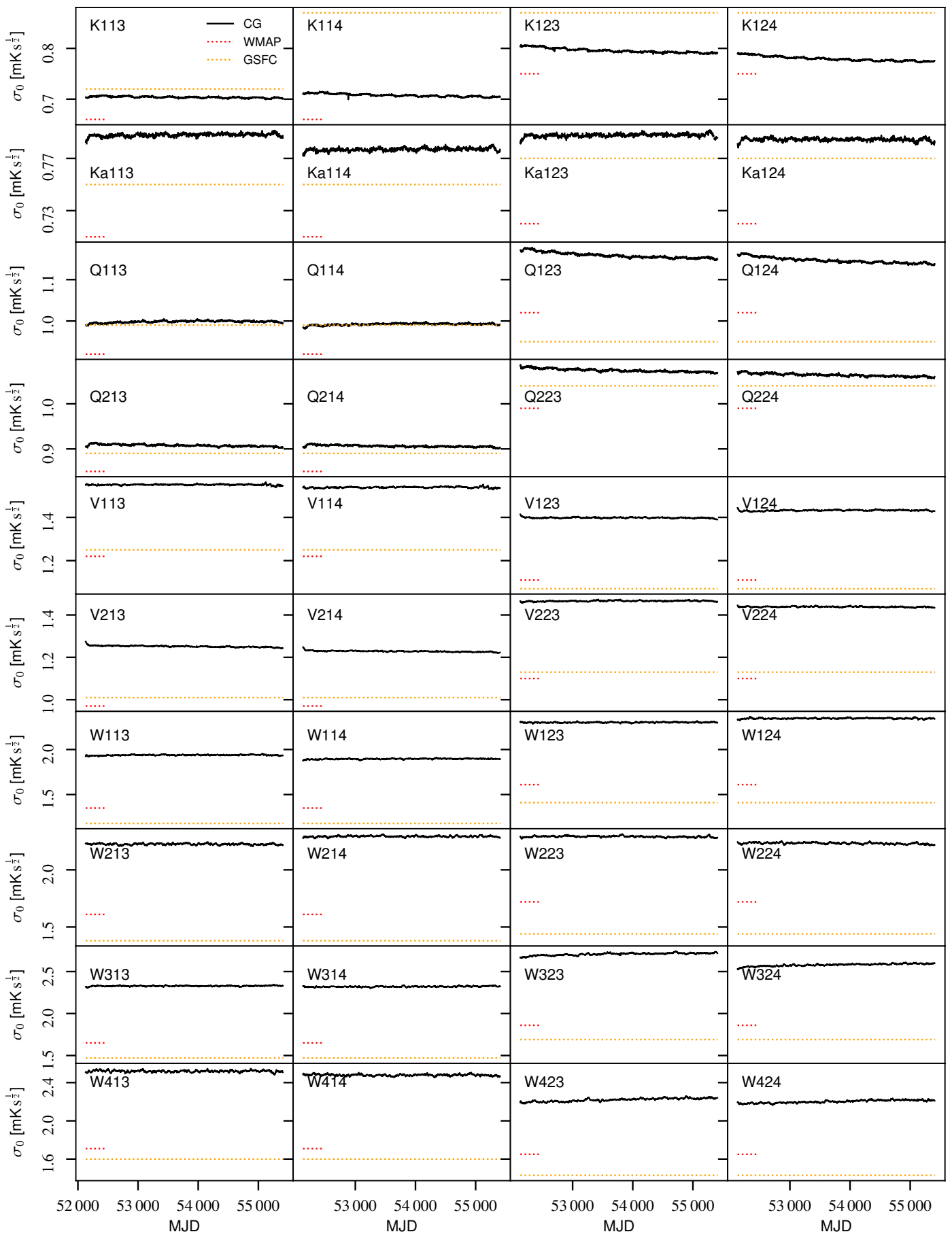
Appendix B: WMAP frequency map survey

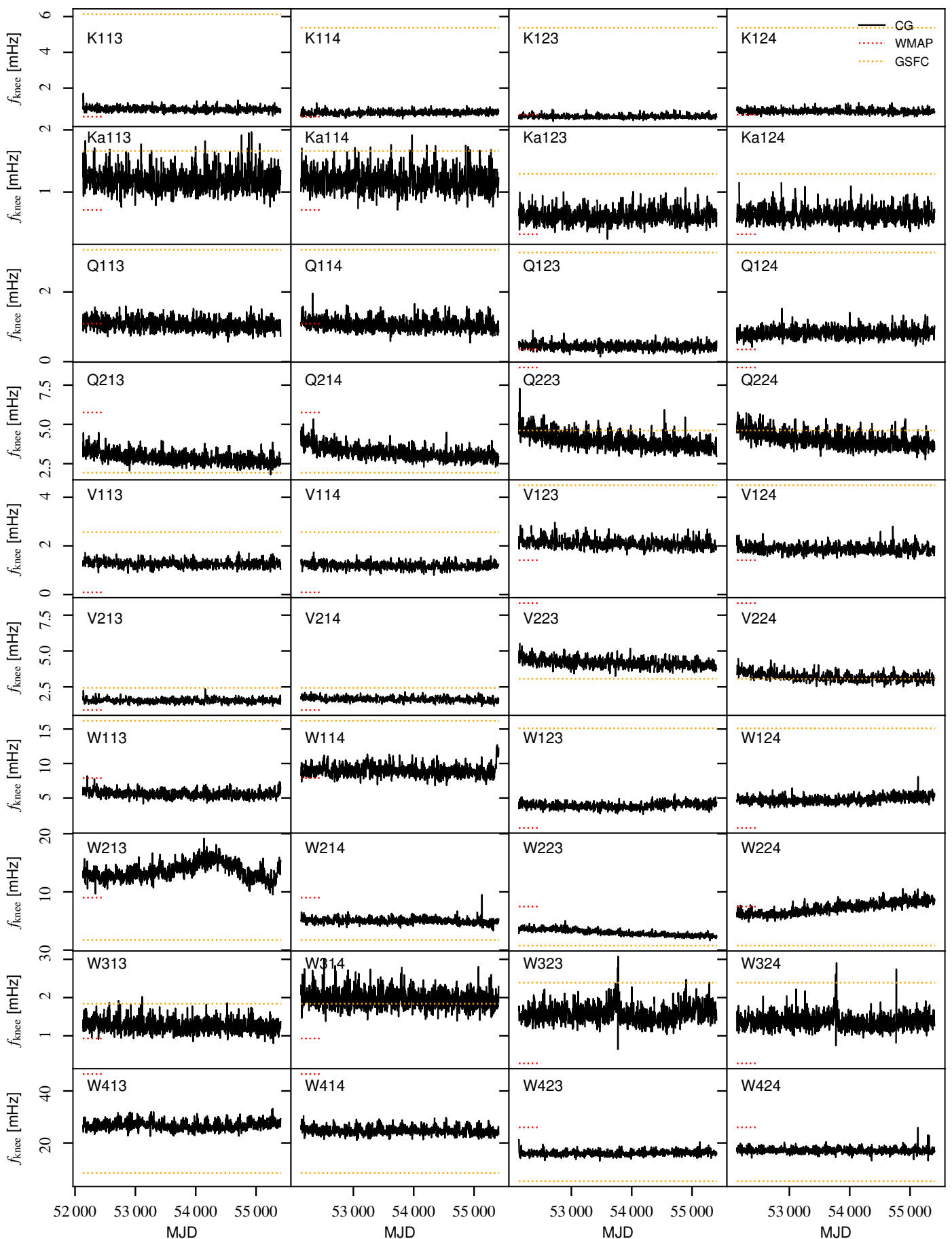
Appendix C: Comparison with BEYONDPLANCK LFI results

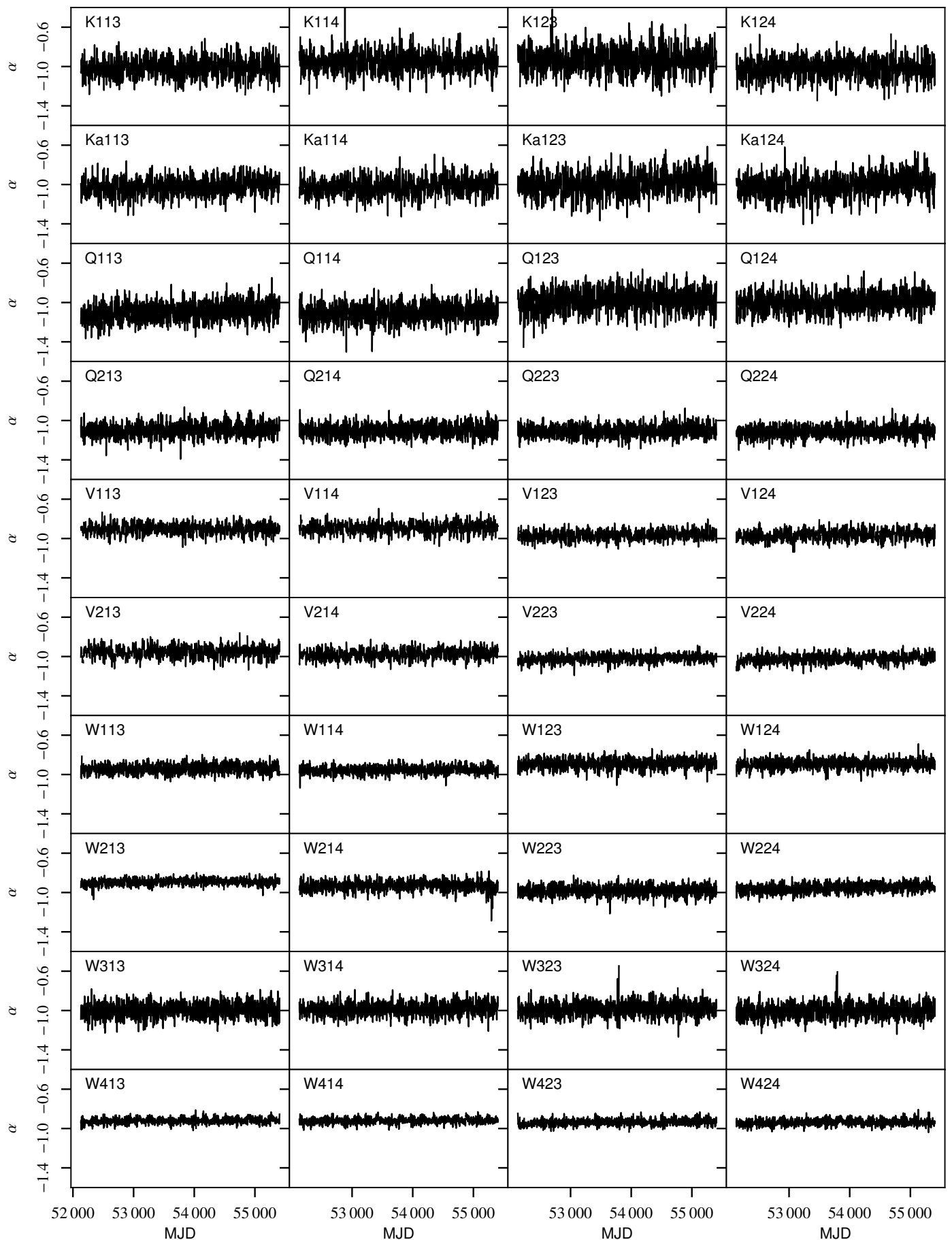
**Fig. A.1.** baseline.

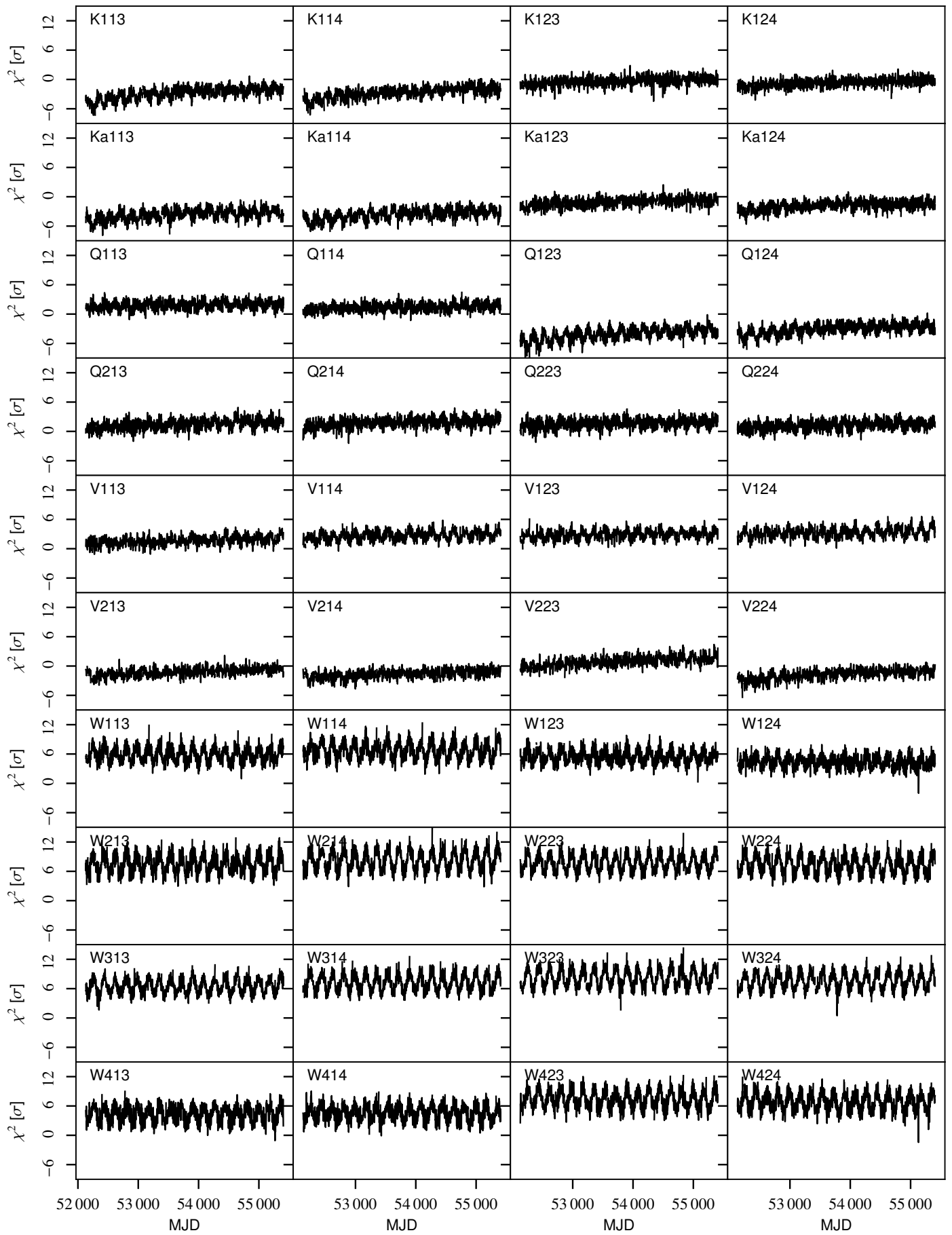
**Fig. A.2.** baseline slopes.

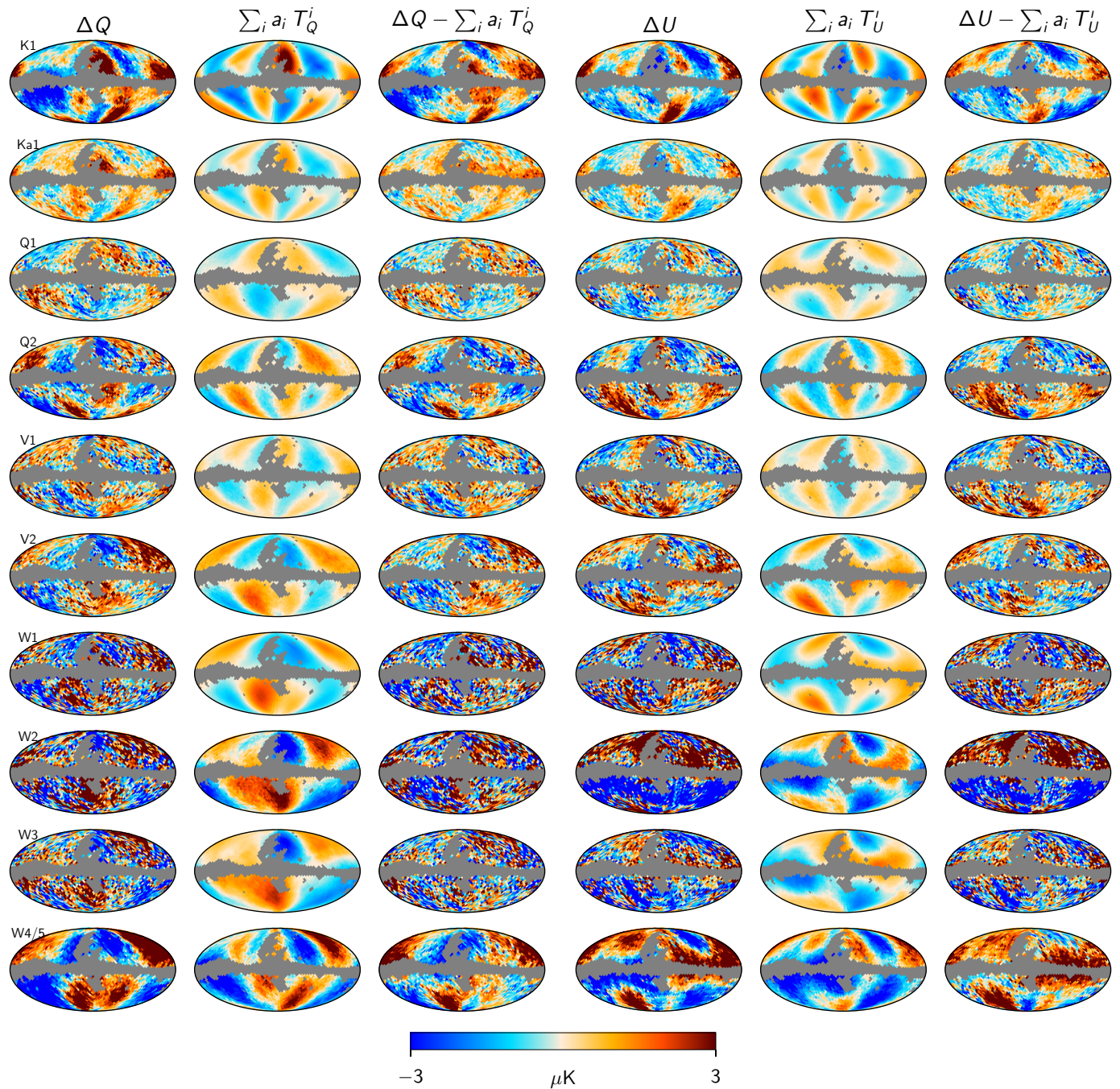
**Fig. A.3.** Gain.

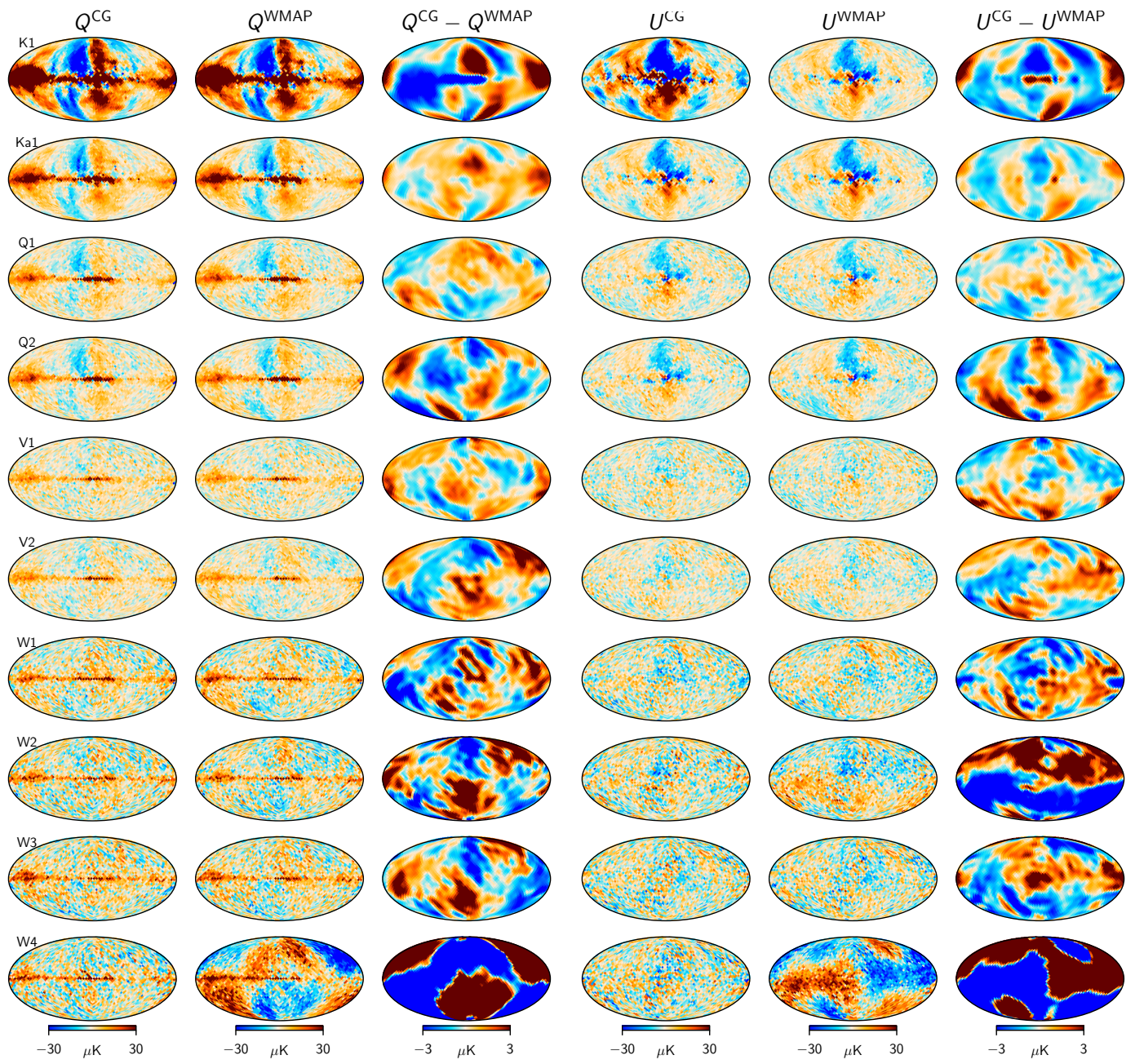
**Fig. A.4.** σ_0 .

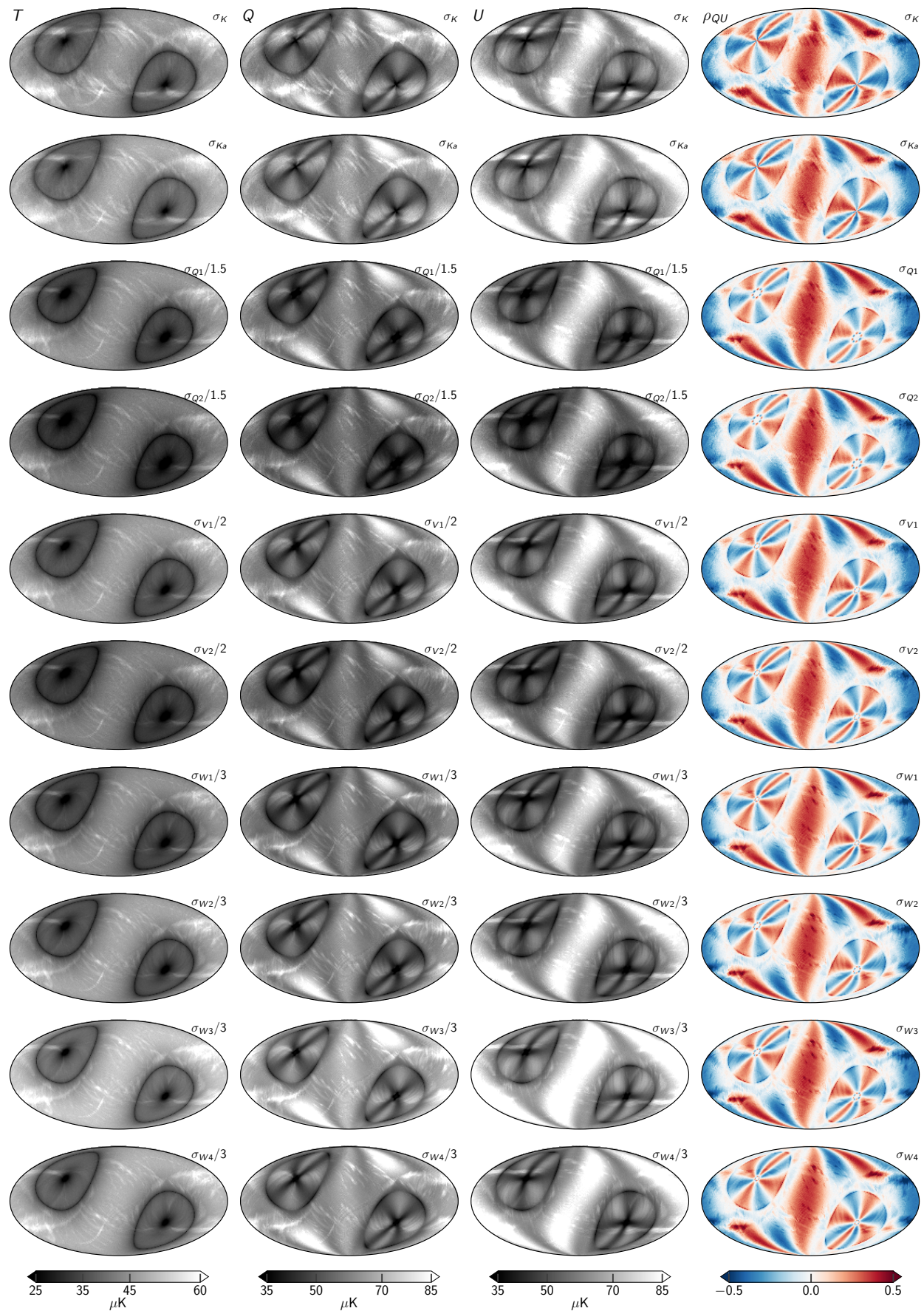
**Fig. A.5.** Fknee.

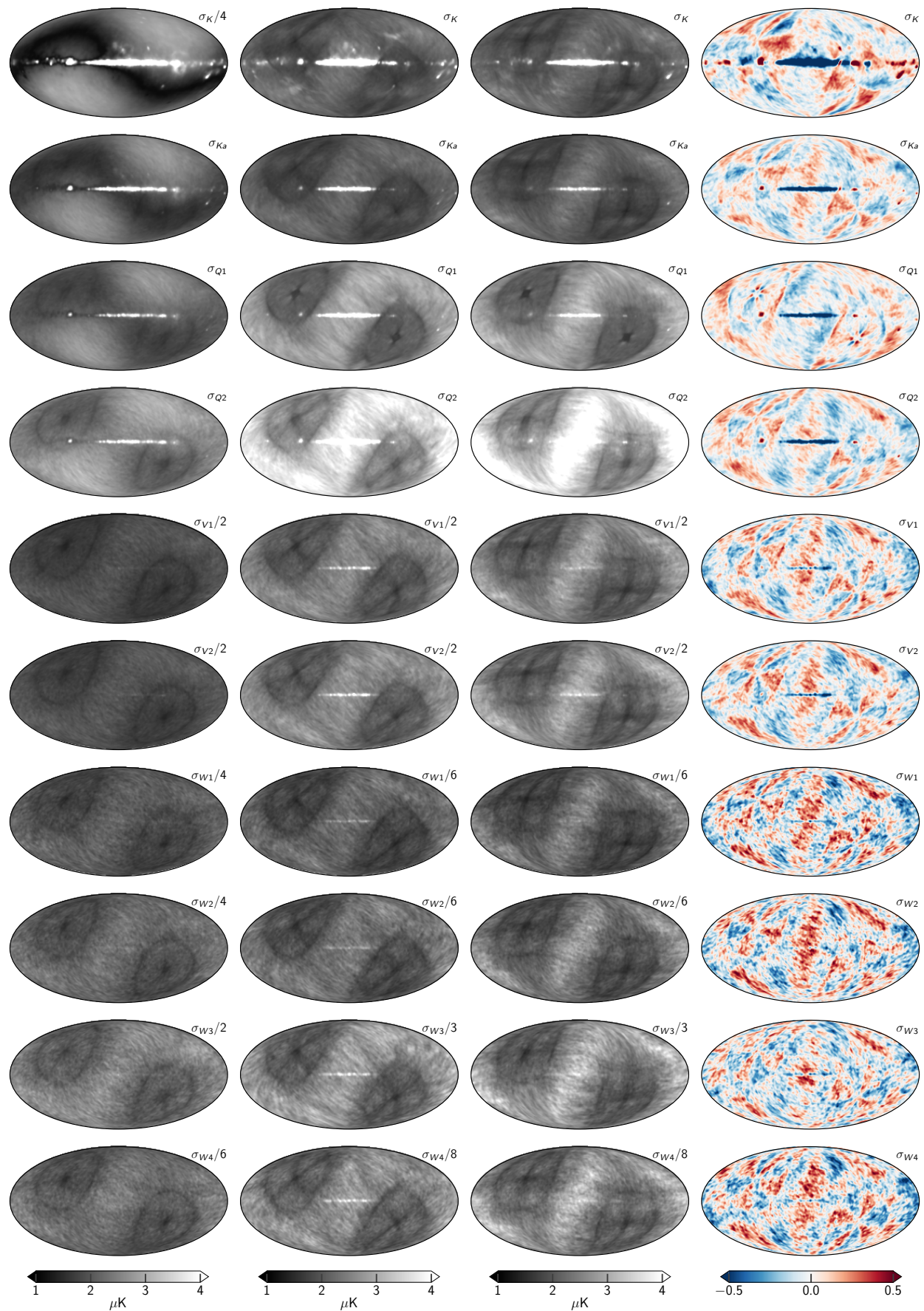
**Fig. A.6.** α .

**Fig. A.7.** chisq.

**Fig. A.8.** Transmission imbalance templates

**Fig. B.1.** Sky maps

**Fig. B.2.** RMS maps

**Fig. B.3.** STD std

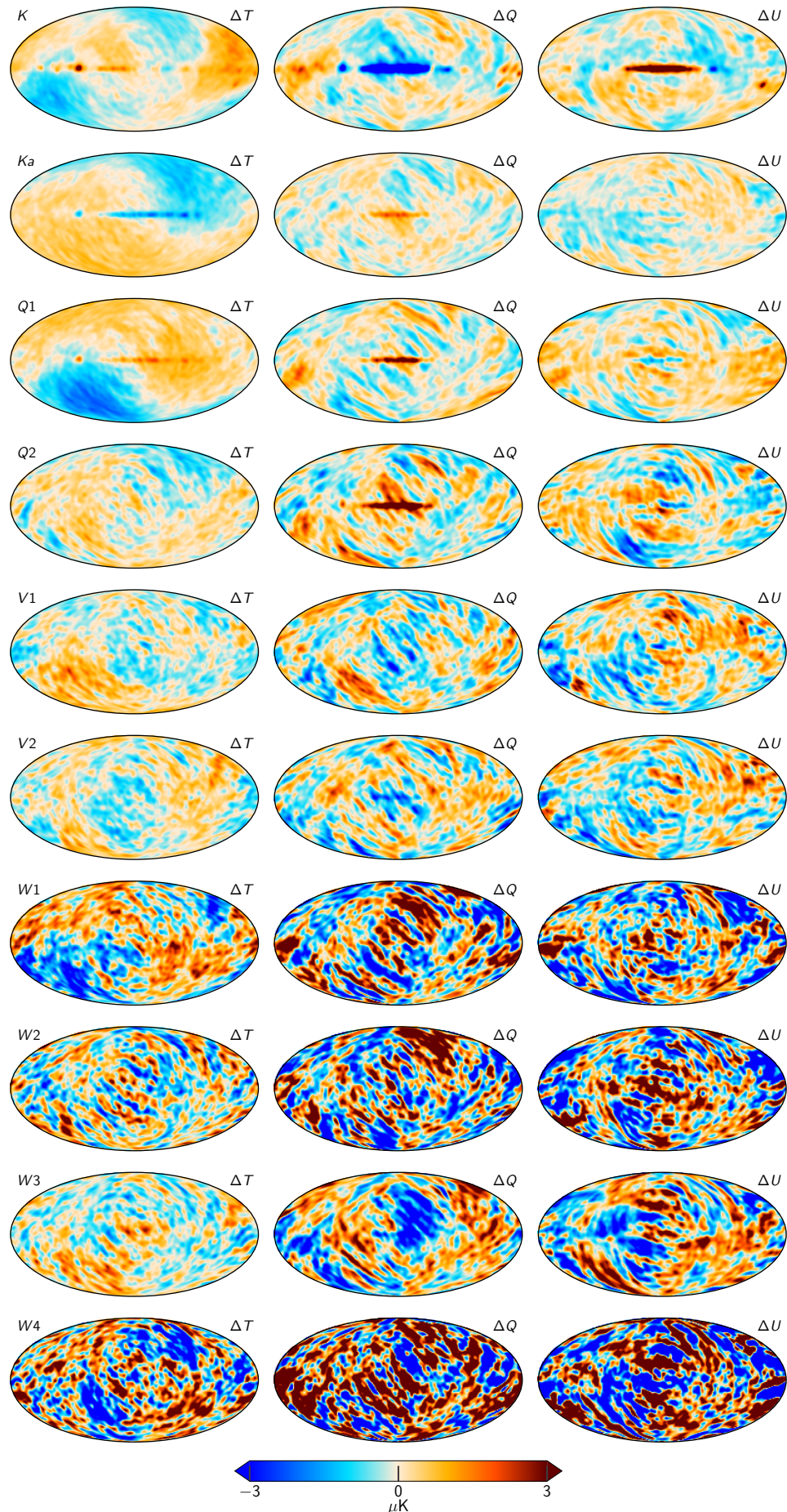
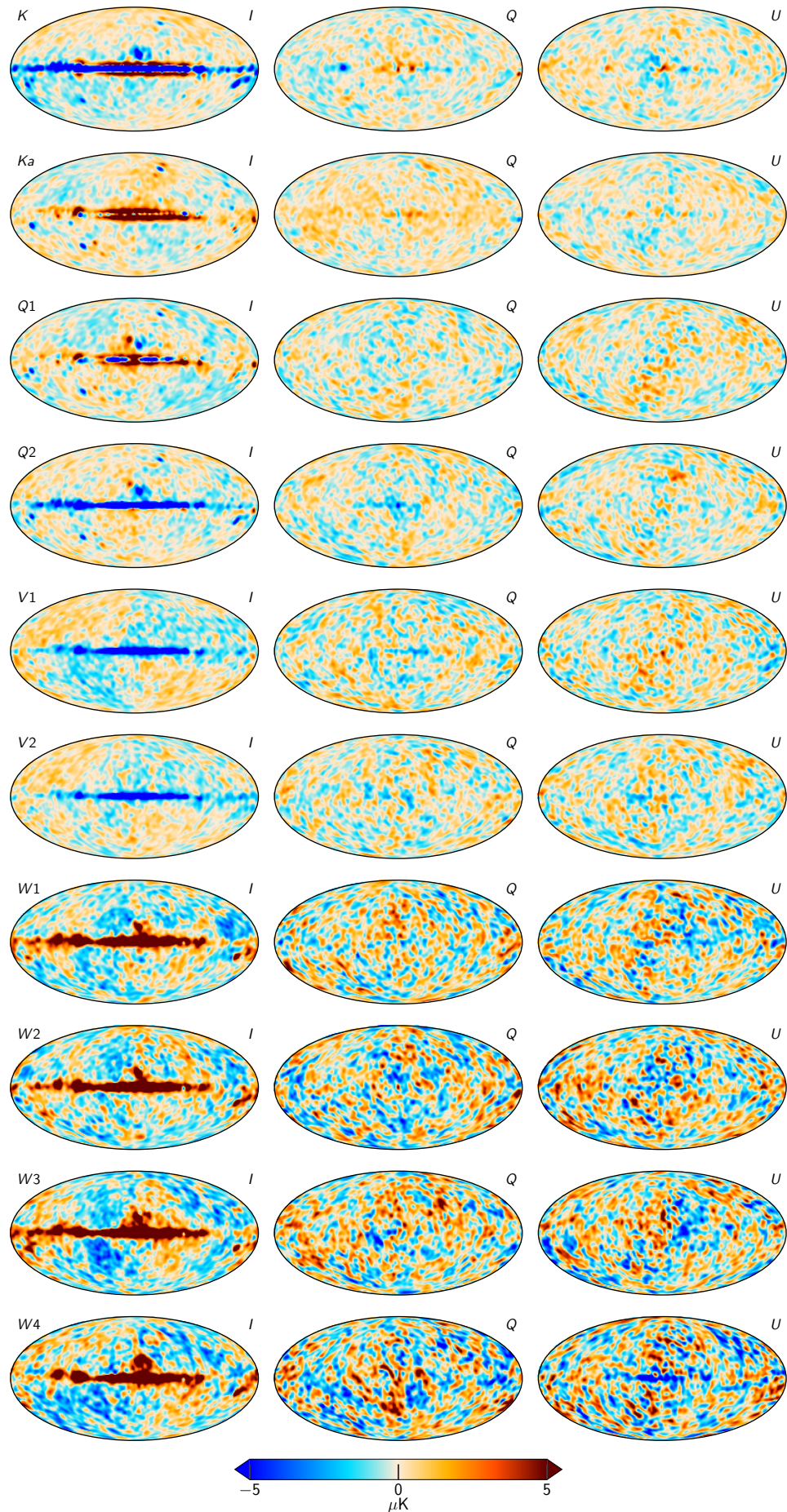


Fig. B.4. Differences between two samples
Article number, page 48 of 49

**Fig. B.5.** TOD Residuals for each of the WMAP channels, smoothed by 5° .